CZECH TECHNICAL UNIVERSITY IN PRAGUE
Faculty of Civil Engineering

Ing. Jan Novák, Ph.D.

Modelling of Microstructure-Informed Fluctuation Fields for Generalized Finite Element Methods

Modelování mikrostrukturálních fluktuačních polí pro zobecněné metody konečných prvků

April, 2022

ACKNOWLEDGMENTS

I would like to thank my wife Iva Dlouhá for her never ending encouragement and support that helped me to attain the goals I have ever set for myself.

I wish to further thank all my colleagues who have given me valuable comments and advises. Namely, I would like to express my deepest gratitude to Prof. Jan Zeman, Prof. Petr Konvalinka and Dr. Martin Doškář for their substantial support at work and beyond.

Last but not least, the financial support provided by the GAČR Grant No. 19-26143X is also gratefully acknowledged.

TABLE OF CONTENTS

Czech Technical University in Prague

Abstract

Modelling of Microstructure-Informed Fluctuation Fields for Generalized Finite Element Methods

Jan Novák

Understanding physical processes taking place in heterogeneous materials at scales where the heterogeneity is perceptible as clearly separated regions, here called inhomogeneities, is important when seeking for phenomena accompanied by abrupt changes in materials integrity, e.g. crack initiation. Macroscopic crack is usually preceded and/or initiated by the presence of stress concentrations at subscale levels, e.g. at notches induced by manufacturing imperfections, stress perturbations among precipitates at metals due to cooling or annealing protocols, or at solid-solid interfaces in composites.

In this collection, it is therefore presented, an approach towards the analysis of fine scale mechanical fields in inhomogeneous media based on Finite Element formulation and classical micromechanics with microstructural modeling strategy backed by Wang tiling's Periodic Unit Cell generalization. In particular, after the short overview on state of the art in the field made in the first chapter, the second chapter deals with a micromechanics-enhanced finite element formulation that accurately captures the mechanical behavior at the media with analytically defined inhomogeneities, yet in a computationally efficient manner. The strategy imprints the closed-form Eshelby solution for ellipsoidal inhomogeneity problem into the so called T-complete Trefftz approximation functions to augment the coarse scale solution by its subscale counterpart. A key feature of this approach is that it does not call for the explicit resolution of the inhomogeneities to the merit of the computational overhead.

The third chapter elaborates in detail the theoretical and computational basis of the micromechanical solutions to be fed into the coarse scale Finite Element formulation and presents implementation issues related to the in-house library developed to this purpose. The chapter also discusses the limitations of micromechanical solutions, namely from the viewpoint of Gibbs effects nearby the inclusion boundaries related to the chosen strategy of the so called self-compatible fields.

The fourth chapter paves the path from solvers at the subscale level on the subscale-size domains, no matter whether these are semi/analytical as in the previous chapter or purely numerical, to generating realizations of microstructure-informed functions on structural-scale-size supports. In particular it presents a stochastic Wang tiling based technique to compress and reconstruct inhomogeneity distribution that is statistically consistent with underlying subscale geometry across several length scales. Unlike the approaches based on the above mentioned Periodic Unit Cell concept, the proposed method works with finite sets of patches, so called tiles, assembled by a stochastic tiling algorithm, thereby eliminating by definition the periodic unit cell's incapability to accurately reproduce long-range orders.

The fifth chapter then extends the Wang tiling approach into the realm of microstructure-informed enrichment functions such that it suits the coarse scale Finite Element formulation presented in the first Chapter. It again deals with a concept of aperiodic tilings, this time, designed to produce not only microstructures morphologically similar to original media but

also the enrichment functions that satisfy up to some extent the traction continuity across the tiles.

The work encloses with a brief overview on works directly following out of the outcomes presented within the previous fourth chapters.

Keywords: Micromechanics; Finite Element Method; Microstructural Modeling; Microstructure-Informed Enrichment Functions; Trefftz Method

České vysoké učení technické v Praze

Abstrakt

Modelování mikrostrukturálních fluktuačních polí pro zobecněné metody konečných prvků

Jan Novák

Pochopení fyzikálních procesů probíhajících v heterogenních materiálech na měřítcích, kde jsou heterogenity vnímány jako zřetelně oddělené souvislé oblasti, tzv. nehomogenity, je důležité zejména při posuzování jevů doprovázených náhlými změnami integrity materiálu, např. vznikem trhlin. Vznik makroskopických trhlin je obvykle řízen koncentrací napětí na nižších měřítcích, jako jsou vruby způsobené výrobními imperfekcemi, precipitáty vzniklé v důsledku zchlazování či žíhání při výrobě a zušlechťování kovů, nebo rozhraní jednotlivých složek v kompozitech.

V předkládané habilitační práci je proto prezentován přístup k detailní analýze mechanických polí v nehomogenních materiálech, který je založený na formulaci konečných prvků, klasické mikromechanice a strategii mikrostrukturního modelování založeného na zobecnění konceptu periodické jednotkové buňky pomocí Wangova dláždění.

První kapitola práce uvádí stručný výčet prací na které je v této práci odkazováno a na nichž jsou prezentované přístupy založeny. Druhá kapitola práce se zabývá obohacenou formulací konečných prvků pro určení mechanické odezvy materiálu s analyticky definovanými nehomogenitami. Tato metoda využívá Eshelbyho řešení pro problém elipsoidální nehomogenity jímž obohacuje T-kompletní Trefftzovy aproximační funkce a tak zahrnuje detaily z mikroúrovně do řešení na makroúrovni. Klíčovým rysem tohoto přístupu je, že nevyžaduje detailní diskretizaci nehomogenit na mikroúrovni a tím nezvyšuje celkovou výpočetní náročnost.

Třetí kapitola podrobně rozvádí teoretický a výpočtový základ pro řešení mikromechanických polí, která jsou vkládána do výše uvedené formulace konečných prvků. Představuje implementační náležitosti související s programovou knihovnou vyvinutou specielně pro tyto účely. Kapitola dále komentuje nevýhody mikromechanických řešení, a to z pohledu Gibbsových jevů v blízkosti hranic inkluzí, které souvisí se zvolenou strategií pro zajištění kompatibility obohacujících polí.

Čtvrtá kapitola poodhaluje zvolenou strategii generování obohacujících funkcí, bez ohledu na to, zda jsou řešeny analyticky, semianalyticky či čistě numericky, na definičních oborech o velikostech srovnatelných s úlohami řešenými na makroúrovni. Představuje stochastickou metodu pro kompresi a rekonstrukci distribuce nehomogenit založenou na Wangově dláždění, která z definice zajišťuje statisticky konzistentní realizace mikrostrukturální geometrie napříč několika korelačními délkami. Narozdíl od přístupu založeném na metodě periodické jednotkové buňky, pracuje v této práci navržená metoda s konečnými množinami dlaždic sestavovanými stochastickým algoritmem, právě za účelem eliminace neschopnosti periodické jednotkové buňky přesně reprodukovat korelační délky větší než jsou její rozměry.

Pátá, kapitola pak rozšiřuje tento přístup do oblasti generování mikrostrukturálních obohacujících funkcí tak, aby vyhovovaly formulaci konečných prvků zvolené v úvodní kapitole. Opět se tedy zabývá konceptem neperiodických dláždění, tentokrát navržených tak, aby popisovaly nejen mikrostruktury morfologicky podobné cílovému materiálu, ale také

obohacující funkce, které do určité míry splňují spojitost vektoru napětí mezi jednotlivými dlaždicemi.

Práce je zakončena šestou kapitolou, ve které je stručně uveden výčet prací navazujících na zde prezentované výsledky a postupy.

Klíčová slova: Mikromechanika; Metoda Konečných prvků; Mikrostrukturální modelování; Mikrostrukturálně informované obohacující funkce, Trefftzova metoda

Chapter 1

A BRIEF SUMMARY OF ADOPTED APPROACHES

The title of this work abbreviates modeling of fluctuations fields in heterogeneous materials with complex microstructures, which may find the use as enrichments in Generalized Finite Element formulations or in the Hybrid Trefftz Finite Element method augmented by Eshelby fields. This work thus stems from Finite Element techniques, Micromechanics, Microstructural modeling and compression and synthesis formalism based on Wang tiling method. As each of the mentioned approaches may be considered as a self-sustained topic, a brief summary on works that are at the heart of the methodology presented in **Chapters 2–4** is given first.

A Brief Summary of Adopted Approaches

Jan Novák

Experimental Centre, Faculty of Civil Engineering, Czech Technical University in Prague, Czech Republic

1. Microstructure-informed enrichments in Finite Element Methods

The ability of Finite Element Methods to capture the subscale features independently of the underlying discretization continues to be a challenge in computational mechanics research. Partition of Unity methods [1–4], based on seminal work of Melenk and Babuška [5] and Babuška and Melenk [6] provide a solution strategy to this problem, without mesh refinement, by extending a given solution space with additional functions. The class of similar algorithms has been called as Generalized Finite Element Methods (GFEM) [7], and as such has been successfully applied to problems such as e.g. cracks and material interfaces.

As for the incorporation of microstructural details into the solution of linear problems, Strouboulis et al. [8] introduced a dictionary of pre-computed local solutions to selected microstructural features, which were then used as enrichment functions within GFEM. Fish and Yuan [9] proposed a multiscale enrichment method, combining the Partition of Unity methods with responses of a periodic microstructure representation to unit loading cases from the computational homogenization [10]. Efendiev et al. [11] developed the Generalized Multiscale Finite Element Method that extracts local enrichments in problem's subdomains from a collection of pre-computed general responses using eigenvalue analyses. In a similar spirit but without pre-calculations, Plews and Duarte [12] generated the microstructure-specific enrichments on-the-fly by subjecting subdomains with finer discretization to boundary values obtained from a coarse global solution, building on the local-global enrichment framework [13]. Outside the GFEM family of approaches, the recently proposed Coarse Mesh Condensation Multiscale method [14], subsequently extended to non-periodic microstructures and non-conforming coarse-scale discretization [15], is conceptually similar to the aforementioned methods as it combines a coarse scale approximation of a strain field with parallel calculations of localization fields within (potentially overlapping) subdomains. In contrast to older works by Zohdi and coworkers, e.g. [16, 17], in which a domain-decomposition-like approach with a regularized approximation at the interfaces of subdomains was adopted, the parametrization of the localization fields is linked to the coarse strain field via an L_2-norm projection in [14, 15].

However, Partition of Unity methods or GFEMs increase the solution complexity by additional degrees of freedom. Therefore, the focus of this work is centered on an alternative approach based on the Hybrid-Trefftz stress element formulation (HTFEM) [18, 19] such that it does not result in additional degrees of freedom (DOFs), at the expense of an additional, often non-negligible, computational overhead related to integration of enrichment functions[18, 20]. The principal difference between GFEM and HTFEM, related to addi-

Email address: novakja@fsv.cvut.cz (Jan Novák)

tional DOFs, stems from the different approaches to the construction of enrichment functions. In GFEM Langrangian formulations, these functions can be chosen nearly arbitrarily, its compatibility at the element boundaries is satisfied by their product with conventional macroscopic basis, though still having a new set of coordinates for the enrichment basis. However, in HTFEM the subscale fields must satisfy, like their coarse-scale counterparts do [21, 22], the governing differential equation (Cauchy stress equilibrium in the case of linear elasticity), and as such do not need to be weighted by macroscopic bases but only simply added to it. The compatibility constraints in the Trefftz methods are satisfied only in a weak/weighted sense, see e.g. Herrera [23, 24] and references therein.

2. Modeling random microstructures

One of the approaches for modeling heterogeneous materials rests on an extension of Periodic Unit Cell (PUC) generated such that its spatial statistics match that of a reference microstructure, see e.g. [25, 26]. This procedure appears in the literature under various names such as Statistically Optimal Representative Unit Cell coined by Lee et al. [27], Repeating Unit Cell given by Yang et al. [28], Statistically Similar Representative Volume Element that first appeared in [29], or Statistically Equivalent Periodic Unit Cell (SEPUC) by Zeman and Šejnoha [30], to name but a few. The spatial statistics, key paradigm in statistics-based microstructural modeling methods, involved range from Minkowski functionals [31] to multi-point probability functions [32], out of which the two-point probability [25, 26, 33], two-point cluster [34], and lineal path [30, 35–37] functions have been used most frequently and as such represent the key paradigm of this work as well.

Following Povirk's seminal work [38], the majority of cell representations are generated using optimization procedures, minimizing the discrepancy between the statistical characterization of the reference microstructure and its compressed representation. The particular choice of optimization algorithm currently varies with several options including simulated annealing [30, 36, 39], genetic [27, 28, 40, 41] and gradient [38, 42], or phase-recovery [43] algorithms.

The second approach to microstructure generation utilizes reference samples of the microstructure. New realizations are then obtained with a Markovian process, taking individual voxels [44] or a patch of voxels [45] from the provided reference samples according to the proximity of the spatial statistics computed for their surroundings. Alternatively, searching for statistics proximity can be replaced with a classification tree-based supervised learning model [46].

The previous two approaches suffer from high computational costs related either to optimization or to training the learning models. The applicability of their outputs is also sensitive to the spatial statistics considered, attesting to the ill-conditioning of the microstructure reconstruction problem itself. Achieving a good match in selected statistics does not automatically guarantee similar overall behavior; for instance, Biswal et al. [47] demonstrated that realizations with similar two-point probability functions could have significantly different percolation characteristics that govern overall transport properties.

Complementary to the statistics-informed methods, a third approach to generating microstructural realizations relies on meta-modeling the genesis of a microstructure. These methods range in complexity and include the Monte-Carlo Potts [48] and phase field models [49] of grain growth; sedimentation-and-compaction models [47]; and various particle

packing algorithms, e.g. [50, 51, and references therein], based on either Random Sequential Adsorption (RSA) [52, 53] or molecular dynamics [54–56].

The relevance of packing algorithms extends beyond simple particle-matrix microstructures because the resulting packing often serve as initial seeds for tessellation-based models applicable to polycrystals [57, 58], foams [51], and cell tissues [59, 60]. Due to its straightforward implementation, Voronoï tessellation is the most common choice; however, the resulting geometry is oversimplified for many materials. For instance, Voronoï-based models overestimate overall stiffness for high porosity foams [61]. The curvature of the cell walls [57, 62] and heterogeneity in cell size [51, 58] and wall thickness [58] must be additionally introduced to obtain realistic geometries. Similar effects can be achieved by modifying the distance measure used during tessellation, e.g. models based on the Laguerre variant generate microstructures with multi-mode cell size distribution [50, 51, 58, 63]. Inspired by Laguerre tessellation, Chakraborty et al. [60] proposed Adaptive Quadratic Voronoï Tessellation, attributing a distinct anisotropic metric to each seed and thus allowing for additional control over the resulting geometry.

The original RSA method [64] suffers from $\mathcal{O}\left(N^2\right)$ complexity for N particles due to overlap checks and is impractical for generating large, densely packed systems. Consequently, several accelerations have been proposed. For Dart Throwing Algorithm [64], which is a simplified case of RSA with equisized circular/spherical particles, Dunbar and Humphreys [65] introduced a scalloped sector representation of non-overlap guaranteed regions. In the same year, Jones [66] proposed an alternative bookkeeping of the regions based on an adaptively updated Voronoï tessellation. Moreover, both approaches utilize a tree data structure and improve the algorithm complexity to $\mathcal{O}(N \log N)$. For general RSA, Yang et al. [28] proposed an acceleration based on a combination of a spline description of particle shapes and hierarchically refined bounding boxes of each particle. Recently, Sonon et al. [67] introduced a method building on an implicit, level-set based description of particle shapes, achieving $\mathcal{O}(N)$ complexity. Moreover, Sonon et al.'s method readily facilitates generating complex microstructures using linear combinations of the nearest neighbor distance functions and dedicated morphing operations [67–70]. In a sense, this approach introduces the anisotropic pseudo-metrics of Chakraborty et al. [60] in a geometrically-motivated way by considering arbitrarily-shaped particles. As a result, Sonon et al.'s method enables refined control over generated microstructure unattainable with standard Voronoï or Laguerre tessellations.

Albeit significantly faster than RSA or optimization-based approaches, the latter method still starts anew every time an additional realization is required, imposing overhead on, e.g., investigations of the Representative Volume Element (RVE) size that require multiple microstructural samples to be generated, see Kanit et al. [71], Gitman et al. [72], Dirrenberger et al. [73]. Alternatively, larger microstructural realizations can be assembled from (SE)PUC; however, such construction introduces non-physical, long-range, periodic artifacts in a microstructural geometry and its local response.

3. Micromechanics

The first attempts to the determination of overall material properties of simple composites, laminates in particular, fall into the realm of the so called rules of mixture and are attributed to Voigt [74] and Reuss [75, 76]. Currently, micromechanics as it is considered

here – a sub-field of solid mechanics –, finds applications across different disciplines as biology [77], civil engineering [78] or analysis of natural and synthetic composites [79]. The large span of applications of micromechanics principles has been allowed by the essential discovery of Eshelby [80] who proved the fact that the strain and stress field inside an ellipsoidal inclusion subjected to a uniform far field excitation is also uniform. Eshelby's analytical results yield the easy estimation of thermomechanical fields in polydisperse media with ellipsoidal inclusions in terms of Young's modulus and Poisson's ratio of each phase, the so called Eshelby's (concentration) tensor and given magnitude of remote uniform loads. For general inclusions, the concentration factors can be derived either by means of rigorous bounding procedures or by making use of specifically tailored approximation techniques as e.g. proposed by Maz'ya and Schmidt [81].

The determination of overall elastic properties of heterogeneous materials on the basis of the well known elasticity energy principles has been contributed by authors as Hashin and Shtrikman [82], Beran [83] and Milton and Phan-Thien [84] to name few. On top of that, a variety of another class of approximation methods based on engineering intuition-assumptions were proposed within the past decades. These include well known and often used dilute approximation, self-consistent methods [85, 86] or very popular Mori-Tanaka method [87, 88]. This topic has been also addressed by the author of this collection in terms of the so called direct integration method presented in Svoboda et al. [89]. Stepping aside from the realm of random dispersion, thus considering the periodic media, the determination of local fields inside representative volumes of the composite can be obtained by numerical procedures as the Finite Element Method or currently very popular Galerkin trigonometric approximation [90–92].

Recent theoretical-computational developments in the field of micromechanics, have been motivated by the author's work [89] and include the direct calculation of coefficients accounting for the inclusion interactions in multiple non-dilute particulate media [93] and a Lagragian Finite Element formulation augmented by the Eshelby fields [94, 95].

4. Tiling

Tiling is a complementary term to the notion of tessellation, which stands for covering an infinite plane by tiles without voids or overlaps. Naturally, decoration is the first purpose of tiling that comes to everyone's mind.

However, from the scientific point of view, Johannes Kepler is usually considered to be the first who systematically investigated tessellations [96]. In the second part of his opus magnum Harmonice Mundi – the book where he also presented his third law of planetary motion – Kepler classified eleven tiling types containing only regular polygons that can create valid planar tilings (tilings without voids or overlaps). Since Kepler's time, the amount of literature on symmetries and tiling has significantly grown as for both theoretical background and applications. Nowadays, the classical reference in the field is the book "Tiling and patterns" by Grnbaum and Shephard [97], which contains also an exposition devoted to aperiodic tilings, the objective of fourth and fifth section of this collection that keeps a particular focus on Wang tiles and related tiling techniques.

Although the concept of Wang tiles was originally developed for reasons of mathematical logic, it has found use in different branches of science. For example, in Physics, the tiling concept has been used in studies of phase transitions of lattice models where individual tiles

represent the state of interacting particles centered at the lattice cells [98]. The particles interact through the tile edges associated with a prescribed binary energy density of either 0 or -1. In these models, the particle volume fraction is either fixed, prohibiting vacancies within the tiling, or ranges from 0 to 1 leading to discontinuous tilings [99]. Regarding predictive capabilities in modeling phase transitions, the former type of models exhibits high order continuous phase transitions at positive temperatures and forms quasi-crystalline structures at low temperatures, while the latter models capture discontinuous first-order transitions between the disordered substance and a quasi-crystalline one.

Wang tiles or computer models (cellular automata) based on Turing machines, known to be reproducible with Wang tiles, are also a promising tool in DNA nanotechology. The tiles represent synthetic units–DNA building blocks–that can be self-assembled into synthetic, two-dimensional, nanometer-scale DNA crystals by obeying the Watson-Crick complementarity. Color codes on tile edges are designed to ensure desired relations between neighboring tiles through the Watson-Crick base pairs, called sticky ends. By a careful tile design eliminating alternative Watson-Crick associations and conformations, scientists have formed layer crystals with varying lattice periodicity [100], exotic crystal patterns such as Sierpinski triangle fractals [101], or a polyhedral mesh for three-dimensional structures [102].

To the best of author's knowledge, the first application of the tiling concept was in computer graphics, namely in rendering surfaces of virtually visualized objects that can be attributed to Stam [103], who used the Amman aperiodic set of sixteen tiles for texture mapping to eliminate artificially looking patterns. Shade et al. [104], modified Stam's idea by introducing a set of only eight tiles and a complementary stochastic skyline tiling algorithm to tile 2D terrains covered by nonperiodic patterns, e.g. sunflowers crop. Hiller et al. [105], used the same tile set and applied it for fast generation of non-periodic point patterns, including those with Poisson's distribution, with blue noise characteristics. They demonstrated how to fill the tiles with point patterns and discussed automatic tile design for texture synthesis and object distribution. Subsequently, Cohen et al. [106], presented an efficient algorithm for tile design that is based on fusing samples of a reference pattern using the quilting procedure reported by Efros and Freeman [107]. Kopf et al. [108], extended the concept by introducing recursive tiling for adaptive point sets. They presented a hierarchical tiling procedure with finer scale tiles nested within coarser ones; however, the distribution of points in each tile remains the same irrespective of the scale. At the same time, Lagae and Dutré [109], introduced a local tiling algorithm, called procedural object distribution function, as an alternative to Shade et al.'s global skyline tiling algorithm, also allowing for real-time generation of textures with objects mapped on Poisson's distribution point sets. Wei [110], presented a tile-based texture mapping algorithm intended specifically for graphics hardware based exclusively on Wang tiles.

Contrary to a wide range of strictly aperiodic sets of planar Wang tiles, there has been published the results on only one set of Wang cubes, a three-dimensional variant of the concept [111]. Stochastic tile set design introduced by Cohen et al. [106] thus enabled also much greater freedom in cube set design for three-dimensional applications. The third dimension of Wang cubes can be either temporal for video synthesis or spatial for geometry placement as in [112]. Lu et al. [113], used Wang cubes to generate 3D pattern textures for scientific visualization tasks, illustrated with rendering anatomy-related datasets.

Computer graphics' quest for an efficient synthesis of naturally-looking textures strongly resembles challenges materials engineers face in modeling heterogeneous materials with

stochastic microstructures. The seminal results on Wang tiling aided compression and synthesis of microstructural data were presented by the author and coworkers in [114], where they introduced the basic principles of Wang tiling to the material modeling applications and combined them with spatial quantification and a priory estimates of spurious long-range order artifacts induced by generalized periodicity constraints. The methodology was compared against PUC representations and illustrated on isotropic mono-disperse microstructures. The follow-up work by Doškář et al. [115] dealt with compression and synthesis of complex, real-world material systems such as sandstone, penetrable mono-disperse media, and aluminum foam. The efficient synthesis of microstructural samples proved to be particularly appealing to applications where multiple realizations of microstructure are needed, such as numerical homogenization of complex microstructures with high contrast in material properties of their constituents [116]. However, the tiling concept has a potential beyond microstructural modeling. The regular partitioning behind the assembled tilings can be readily used in formulation criteria in Representative Volume Element size determination and combined with domain decomposition methods to accelerate pertinent calculations [117]. Moreover, beyond the findings presented in **Chapter 5**, Wang tiles have been further explored as a tool for efficient synthesis of microstructure-informed enrichment functions in generalized finite element methods [118].

References

[1] N. Sukumar, D. Chopp, N. Moës, T. Belytschko, Modeling holes and inclusions by level sets in the extended finite-element method, Computer Methods in Applied Mechanics and Engineering 190 (46–47) (2001) 6183–6200.

[2] N. Moës, J. Dolbow, T. Belytschko, A finite element method for crack growth without remeshing, International Journal for Numerical Methods in Engineering 46 (1) (1999) 131–150.

[3] N. Moës, M. Cloirec, P. Cartraud, J.-F. Remacle, A computational approach to handle complex microstructure geometries, Computer Methods in Applied Mechanics and Engineering 192 (28–30) (2003) 3163–3177.

[4] G. Wells, L. Sluys, R. D. Borst, Simulating the propagation of displacement discontinuities in a regularised strain-softening medium, International Journal for Numerical Methods in Engineering 53 (5) (2002) 1235–1256.

[5] J. Melenk, I. Babuška, The partition of unity finite element method: Basic theory and applications, Computer Methods in Applied Mechanics and Engineering 139 (1-4) (1996) 289–314, ISSN 00457825, doi:10.1016/S0045-7825(96)01087-0.

[6] I. Babuška, J. Melenk, The partition of unity method, International Journal for Numerical Methods in Engineering 40 (4) (1997) 727–758.

[7] T. Belytschko, R. Gracie, G. Ventura, A review of extended/generalized finite element methods for material modeling, Modelling and Simulation in Materials Science and Engineering 17 (4) (2009) 043001, ISSN 0965-0393, 1361-651X, doi: 10.1088/0965-0393/17/4/043001.

[8] T. Strouboulis, L. Zhang, I. Babuška, Generalized finite element method using mesh-based handbooks: application to problems in domains with many voids, Computer Methods in Applied Mechanics and Engineering 192 (28-30) (2003) 3109–3161, ISSN 00457825, doi:10.1016/S0045-7825(03)00347-5.

[9] J. Fish, Z. Yuan, Multiscale enrichment based on partition of unity, International Journal for Numerical Methods in Engineering 62 (10) (2005) 1341–1359, ISSN 0029-5981, 1097-0207, doi:10.1002/nme.1230.

[10] M. G. D. Geers, V. G. Kouznetsova, K. Matouš, J. Yvonnet, Homogenization Methods and Multiscale Modeling: Nonlinear Problems, in: E. Stein, R. de Borst, T. J. R. Hughes (Eds.), Encyclopedia of Computational Mechanics Second Edition, John Wiley & Sons, Ltd, Chichester, UK, ISBN 978-1-119-00379-3 978-1-119-17681-7, 1–34, doi:10.1002/9781119176817.ecm107, 2017.

[11] Y. Efendiev, J. Galvis, T. Y. Hou, Generalized multiscale finite element methods (GMsFEM), Journal of Computational Physics 251 (2013) 116–135, ISSN 00219991, doi:10.1016/j.jcp.2013.04.045.

[12] J. Plews, C. Duarte, Bridging multiple structural scales with a generalized finite element method, International Journal for Numerical Methods in Engineering 102 (3-4) (2015) 180–201, ISSN 00295981, doi:10.1002/nme.4703.

[13] C. Duarte, D.-J. Kim, Analysis and applications of a generalized finite element method with globallocal enrichment functions, Computer Methods in Applied Mechanics and Engineering 197 (6-8) (2008) 487–504, ISSN 00457825, doi:10.1016/j.cma.2007.08.017.

[14] M. V. Le, J. Yvonnet, N. Feld, F. Detrez, The Coarse Mesh Condensation Multiscale Method for parallel computation of heterogeneous linear structures without scale separation, Computer Methods in Applied Mechanics and Engineering 363 (2020) 112877, ISSN 00457825, doi:10.1016/j.cma.2020.112877.

[15] M. V. Le, J. Yvonnet, N. Feld, F. Detrez, Full-field elastic simulations for image-based heterogeneous structures with a Coarse Mesh Condensation Multiscale Method, International Journal for Multiscale Computational Engineering ISSN 1543-1649, doi:10.1615/IntJMultCompEng.2020034828.

[16] T. Zohdi, P. Wriggers, A domain decomposition method for bodies with heterogeneous microstructure based on material regularization, International Journal of Solids and Structures 36 (17) (1999) 2507–2525, ISSN 00207683, doi:10.1016/S0020-7683(98)00124-3.

[17] T. Zohdi, P. Wriggers, C. Huet, A method of substructuring large-scale computational micromechanical problems, Computer Methods in Applied Mechanics and Engineering 190 (43-44) (2001) 5639–5656, ISSN 00457825, doi:10.1016/S0045-7825(01)00189-X.

[18] L. Kaczmarczyk, C. J. Pearce, A corotational hybrid-Trefftz stress formulation for modelling cohesive cracks, Computer Methods in Applied Mechanics and Engineering 198 (15-16) (2009) 1298 – 1310, ISSN 0045-7825, doi:DOI:10.1016/j.cma.2008.11.018.

[19] J. Jirousek, A. Wroblewski, T-elements: state of the art and future trends, Archives of Computational Methods in Engineering 3 (4) (1996) 323–434.

[20] J. Teixeira de Freitas, Formulation of elastostatic hybrid-Trefftz stress elements, Computer Methods in Applied Mechanics and Engineering 153 (1998) 127 – 151.

[21] Q.-H. Qin, Q. Qin, The Trefftz finite and boundary element method, WIT Southampton, 2000.

[22] Q.-H. Qin, H. Wang, Matlab and C programming for Trefftz finite element methods, CRC Press, 2008.

[23] I. Herrera, Trefftz method: a general theory, Numerical Methods for Partial Differential Equations: An International Journal 16 (6) (2000) 561–580.

[24] I. Herrera, Trefftz method, in: Topics in boundary element research, Springer, 225–253, 1984.

[25] J. Zeman, M. Šejnoha, Numerical evaluation of effective elastic properties of graphite fiber tow impregnated by polymer matrix, Journal of the Mechanics and Physics of Solids 49 (1) (2001) 69–90, doi:10.1016/S0022-5096(00)00027-2.

[26] M. G. Rozman, M. Utz, Efficient reconstruction of multiphase morphologies from correlation functions, Physical Review E 63 (6), ISSN 1063-651X, 1095-3787, doi:10.1103/PhysRevE.63.066701.

[27] H. Lee, M. Brandyberry, A. Tudor, K. Matouš, Three-dimensional reconstruction of statistically optimal unit cells of polydisperse particulate composites from microtomography, Physical Review E 80 (6) (2009) 061301, ISSN 1539-3755, 1550-2376, doi:10.1103/PhysRevE.80.061301.

[28] M. Yang, A. Nagarajan, B. Liang, S. Soghrati, New algorithms for virtual reconstruction of heterogeneous microstructures, Computer Methods in Applied Mechanics and Engineering 338 (2018) 275–298, ISSN 00457825, doi:10.1016/j.cma.2018.04.030.

[29] D. Balzani, L. Scheunemann, D. Brands, J. Schrder, Construction of two- and three-dimensional statistically similar RVEs for coupled micro-macro simulations, Computational Mechanics 54 (5) (2014) 1269–1284, ISSN 0178-7675, 1432-0924, doi:10.1007/s00466-014-1057-6.

[30] J. Zeman, M. Šejnoha, From random microstructures to representative volume elements, Modelling and Simulation in Materials Science and Engineering 15 (4) (2007) S325–S335, ISSN 0965-0393, 1361-651X, doi:10.1088/0965-0393/15/4/S01.

[31] L. Scheunemann, D. Balzani, D. Brands, J. Schrder, Design of 3D statistically similar Representative Volume Elements based on Minkowski functionals, Mechanics of Materials 90 (2015) 185–201, ISSN 01676636, doi:10.1016/j.mechmat.2015.03.005.

[32] S. Torquato, Random heterogeneous materials: Microstructure and macroscopic properties, no. 16 in Interdisciplinary applied mathematics, Springer, New York, ISBN 0-387-95167-9, 2002.

[33] Y. Jiao, F. Stillinger, S. Torquato, Modeling heterogeneous materials via two-point correlation functions: Basic principles, Physical Review E 76 (3) (2007) 031110, ISSN 1539-3755, 1550-2376, doi:10.1103/PhysRevE.76.031110.

[34] Y. Jiao, F. H. Stillinger, S. Torquato, A superior descriptor of random textures and its predictive capacity, Proceedings of the National Academy of Sciences 106 (42) (2009) 17634–17639, ISSN 0027-8424, 1091-6490, doi:10.1073/pnas.0905919106.

[35] B. Lu, S. Torquato, Lineal-path function for random heterogeneous materials, Physical Review A 45 (2) (1992) 922–929, ISSN 1050-2947, 1094-1622, doi:10.1103/PhysRevA.45.922.

[36] H. Kumar, C. Briant, W. Curtin, Using microstructure reconstruction to model mechanical behavior in complex microstructures, Mechanics of Materials 38 (8-10) (2006) 818–832, ISSN 01676636, doi:10.1016/j.mechmat.2005.06.030.

[37] J. Havelka, A. Kučerová, J. Skora, Compression and reconstruction of random microstructures using accelerated lineal path function, Computational Materials Science 122 (2016) 102–117, ISSN 09270256, doi:10.1016/j.commatsci.2016.04.044.

[38] G. L. Povirk, Incorporation of microstructural information into models of two-phase materials, Acta Metallurgica et Materialia 43 (8) (1995) 3199 – 3206, ISSN 0956-7151, doi:http://dx.doi.org/10.1016/0956-7151(94)00487-3.

[39] C. Yeong, S. Torquato, Reconstructing random media, Physical Review E 57 (1) (1998) 495–506, ISSN 1063-651X, 1095-3787, doi:10.1103/PhysRevE.57.495.

[40] D. Basanta, M. A. Miodownik, E. A. Holm, P. J. Bentley, Using genetic algorithms to evolve three-dimensional microstructures from two-dimensional micrographs, Metallurgical and Materials Transactions A 36 (7) (2005) 1643–1652, ISSN 1073-5623, 1543-1940, doi:10.1007/s11661-005-0026-2.

[41] N. C. Kumar, K. Matouš, P. H. Geubelle, Reconstruction of periodic unit cells of multimodal random particulate composites using genetic algorithms, Computational Materials Science 42 (2) (2008) 352–367, ISSN 09270256, doi:10.1016/j.commatsci.2007.07.043.

[42] D. Fullwood, S. Kalidindi, S. Niezgoda, A. Fast, N. Hampson, Gradient-based microstructure reconstructions from distributions using fast Fourier transforms, Materials Science and Engineering: A 494 (1-2) (2008) 68–72, ISSN 09215093, doi:10.1016/j.msea.2007.10.087.

[43] D. T. Fullwood, S. R. Niezgoda, S. R. Kalidindi, Microstructure reconstructions from 2-point statistics using phase-recovery algorithms, Acta Materialia 56 (5) (2008) 942–948, ISSN 13596454, doi:10.1016/j.actamat.2007.10.044.

[44] X. Liu, V. Shapiro, Random heterogeneous materials via texture synthesis, Computational Materials Science 99 (2015) 177–189, ISSN 09270256, doi:10.1016/j.commatsci.2014.12.017.

[45] P. Tahmasebi, M. Sahimi, Cross-Correlation Function for Accurate Reconstruction of Heterogeneous Media, Physical Review Letters 110 (7) (2013) 078002, ISSN 0031-9007, 1079-7114, doi:10.1103/PhysRevLett.110.078002.

[46] R. Bostanabad, A. T. Bui, W. Xie, D. W. Apley, W. Chen, Stochastic microstructure characterization and reconstruction via supervised learning, Acta Materialia 103 (2016) 89–102, ISSN 13596454, doi:10.1016/j.actamat.2015.09.044.

[47] B. Biswal, C. Manwart, R. Hilfer, S. Bakke, P. ren, Quantitative analysis of experimental and synthetic microstructures for sedimentary rock, Physica A: Statistical Mechanics and its Applications 273 (3-4) (1999) 452–475, ISSN 03784371, doi:10.1016/S0378-4371(99)00248-4.

[48] Y. Saito, M. Enomoto, Monte Carlo Simulation of Grain Growth, ISIJ International 32 (3) (1992) 267–274, ISSN 0915-1559, doi:10.2355/isijinternational.32.267.

[49] C. Krill III, L.-Q. Chen, Computer simulation of 3-D grain growth using a phase-field model, Acta Materialia 50 (12) (2002) 3059–3075, ISSN 13596454, doi:10.1016/S1359-6454(02)00084-8.

[50] S. Falco, J. Jiang, F. De Cola, N. Petrinic, Generation of 3D polycrystalline microstructures with a conditioned Laguerre-Voronoi tessellation technique, Computational Materials Science 136 (2017) 20–28, ISSN 09270256, doi:10.1016/j.commatsci.2017.04.018.

[51] J. Alsayednoor, P. Harrison, Evaluating the performance of microstructure generation algorithms for 2-d foam-like representative volume elements, Mechanics of Materials 98 (2016) 44–58, ISSN 01676636, doi:10.1016/j.mechmat.2016.04.001.

[52] D. W. Cooper, Random-sequential-packing simulations in three dimensions for spheres, Physical Review A 38 (1) (1988) 522–524, ISSN 0556-2791, doi:10.1103/PhysRevA.38.522.

[53] J. Segurado, J. Llorca, A numerical approximation to the elastic properties of sphere-reinforced composites, Journal of the Mechanics and Physics of Solids 50 (10) (2002) 2107–2121, ISSN 00225096, doi:10.1016/S0022-5096(02)00021-2.

[54] B. D. Lubachevsky, F. H. Stillinger, Geometric properties of random disk packings, Journal of Statistical Physics 60 (5-6) (1990) 561–583, ISSN 0022-4715, 1572-9613, doi:10.1007/BF01025983.

[55] A. Donev, S. Torquato, F. H. Stillinger, Neighbor list collision-driven molecular dynamics simulation for nonspherical hard particles. I. Algorithmic details, Journal of Computational Physics 202 (2) (2005) 737–764, ISSN 00219991, doi:10.1016/j.jcp.2004.08.014.

[56] E. Ghossein, M. Lvesque, Random generation of periodic hard ellipsoids based on molecular dynamics: A computationally-efficient algorithm, Journal of Computational Physics 253 (2013) 471–490, ISSN 00219991, doi:10.1016/j.jcp.2013.07.004.

[57] M. De Giorgi, A. Carofalo, V. Dattoma, R. Nobile, F. Palano, Aluminium foams structural modelling, Computers & Structures 88 (1-2) (2010) 25–35, ISSN 00457949, doi:10.1016/j.compstruc.2009.06.005.

[58] Y. Chen, R. Das, M. Battley, Effects of cell size and cell wall thickness variations on the stiffness of closed-cell foams, International Journal of Solids and Structures 52 (2015) 150–164, ISSN 00207683, doi:10.1016/j.ijsolstr.2014.09.022.

[59] H. Mebatsion, P. Verboven, B. Verlinden, Q. Ho, T. Nguyen, B. Nicola, Microscale modelling of fruit tissue using Voronoi tessellations, Computers and Electronics in Agriculture 52 (1-2) (2006) 36–48, ISSN 01681699, doi:10.1016/j.compag.2006.01.002.

[60] A. Chakraborty, M. M. Perales, G. V. Reddy, A. K. Roy-Chowdhury, Adaptive Geometric Tessellation for 3D Reconstruction of Anisotropically Developing Cells in Multilayer Tissues from Sparse Volumetric Microscopy Images, PLoS ONE 8 (8) (2013) e67202, ISSN 1932-6203, doi:10.1371/journal.pone.0067202.

[61] M. Doškář, J. Novák, A jigsaw puzzle framework for homogenization of high porosity foams, Computers & Structures 166 (2016) 33–41, ISSN 00457949, doi:10.1016/j.compstruc.2016.01.003.

[62] A. Simone, L. Gibson, The effects of cell face curvature and corrugations on the stiffness and strength of metallic foams, Acta Materialia 46 (11) (1998) 3929–3935, ISSN 13596454, doi:10.1016/S1359-6454(98)00072-X.

[63] A. Lyckegaard, E. M. Lauridsen, W. Ludwig, R. W. Fonda, H. F. Poulsen, On the Use of Laguerre Tessellations for Representations of 3D Grain Structures, Advanced Engineering Materials 13 (3) (2011) 165–170, ISSN 14381656, doi:10.1002/adem.201000258.

[64] D. P. Mitchell, Generating antialiased images at low sampling densities, ACM SIGGRAPH Computer Graphics 21 (4) (1987) 65–72, ISSN 00978930, doi:10.1145/37402.37410.

[65] D. Dunbar, G. Humphreys, A spatial data structure for fast Poisson-disk sample generation, ACM Transactions on Graphics 25 (3) (2006) 503, ISSN 07300301, doi:10.1145/1141911.1141915.

[66] T. R. Jones, Efficient Generation of Poisson-Disk Sampling Patterns, Journal of Graphics Tools 11 (2) (2006) 27–36, ISSN 1086-7651, doi:10.1080/2151237X.2006.10129217.

[67] B. Sonon, B. Franois, T. Massart, A unified level set based methodology for fast generation of complex microstructural multi-phase RVEs, Computer Methods in Applied Mechanics and Engineering 223-224 (2012) 103–122, ISSN 00457825, doi: 10.1016/j.cma.2012.02.018.

[68] B. Sonon, T. Massart, A Level-Set Based Representative Volume Element Generator and XFEM Simulations for Textile and 3D-Reinforced Composites, Materials 6 (12) (2013) 5568–5592, ISSN 1996-1944, doi:10.3390/ma6125568.

[69] B. Sonon, B. Franois, T. J. Massart, An advanced approach for the generation of complex cellular material representative volume elements using distance fields and level sets, Computational Mechanics 56 (2) (2015) 221–242, ISSN 0178-7675, 1432-0924, doi:10.1007/s00466-015-1168-8.

[70] T. J. Massart, B. Sonon, K. Ehab Moustafa Kamel, L. H. Poh, G. Sun, Level set-based generation of representative volume elements for the damage analysis of irregular masonry, Meccanica 53 (7) (2018) 1737–1755, ISSN 0025-6455, 1572-9648, doi: 10.1007/s11012-017-0695-0.

[71] T. Kanit, S. Forest, I. Galliet, V. Mounoury, D. Jeulin, Determination of the size of the representative volume element for random composites: statistical and numerical approach, International Journal of Solids and Structures 40 (13-14) (2003) 3647–3679, ISSN 00207683, doi:10.1016/S0020-7683(03)00143-4.

[72] I. Gitman, H. Askes, L. Sluys, Representative volume: Existence and size determination, Engineering Fracture Mechanics 74 (16) (2007) 2518–2534, ISSN 00137944, doi:10.1016/j.engfracmech.2006.12.021.

[73] J. Dirrenberger, S. Forest, D. Jeulin, Towards gigantic RVE sizes for 3D stochastic fibrous networks, International Journal of Solids and Structures 51 (2) (2014) 359–376, ISSN 00207683, doi:10.1016/j.ijsolstr.2013.10.011.

[74] W. Voigt, Theoretische studien uber die elasticitatsverhaltnisse des krystalle, I, II, Abh. Ges. Wiss., Gottingen .

[75] A. Reuss, Calculation of the flow limits of mixed crystals on the basis of the plasticity of monocrystals, Z. Angew. Math. Mech 9 (1929) 49–58.

[76] A. Reuss, Computation of the yield point of mixed crystals due to hiring for single crystals, Math. Phys 9 (1929) 49–58.

[77] A. Fritsch, C. Hellmich, Universalmicrostructural patterns in cortical and trabecular, extracellular and extravascular bone materials: micromechanics-based prediction of anisotropic elasticity, Journal of Theoretical Biology 244 (4) (2007) 597–620.

[78] B. Pichler, C. Hellmich, Upscaling quasi-brittle strength of cement paste and mortar: A multi-scale engineering mechanics model, Cement and Concrete Research 41 (5) (2011) 467–476.

[79] K. Hofstetter, C. Hellmich, J. Eberhardsteiner, Micromechanical modeling of solid-type and plate-type deformation patterns within softwood materials. A review and an improved approach .

[80] J. D. Eshelby, The Determination of the Elastic Field of an Ellipsoidal Inclusion, and Related Problems, Proceedings of the Royal Society A: Mathematical, Physical and Engineering Sciences 241 (1226) (1957) 376–396, ISSN 1364-5021, 1471-2946, doi: 10.1098/rspa.1957.0133.

[81] V. Maz'ya, G. Schmidt, Approximate approximations, American Mathematical Society, Providence, RI, 2007.

[82] Z. Hashin, S. Shtrikman, A variational approach to the theory of the elastic behaviour of multiphase materials, Journal of the Mechanics and Physics of Solids 11 (2) (1963) 127–140.

[83] R. Beran, Testing for uniformity on a compact homogeneous space, Journal of Applied Probability 5 (1) (1968) 177–195.

[84] G. W. Milton, N. Phan-Thien, New bounds on effective elastic moduli of two-component materials, Proceedings of the Royal Society of London. A. Mathematical and Physical Sciences 380 (1779) (1982) 305–331.

[85] R. Hill, A self-consistent mechanics of composite materials, Journal of the Mechanics and Physics of Solids 13 (4) (1965) 213–222.

[86] S. Kanaun, V. Levin, Self-consistent methods for composites: Vol. 1: Static problems, vol. 148, Springer Science & Business Media, 2007.

[87] T. Mori, K. Tanaka, Average stress in matrix and average elastic energy of materials with misfitting inclusions, Acta metallurgica 21 (5) (1973) 571–574.

[88] Y. Benveniste, A new approach to the application of Mori-Tanaka's theory in composite materials, Mechanics of materials 6 (2) (1987) 147–157.

[89] L. Svoboda, S. Šulc, T. Janda, J. Vorel, J. Novák, μMech micromechanics library, Advances in Engineering Software 100 (2016) 148–160.

[90] P. Suquet, Elements of homogenization theory for inelastic solid mechanics, Homogenization techniques for composite media .

[91] J.-C. Michel, H. Moulinec, P. Suquet, Effective properties of composite materials with periodic microstructure: a computational approach, Computer methods in applied mechanics and engineering 172 (1-4) (1999) 109–143.

[92] J. Zeman, J. Vondřejc, J. Novák, I. Marek, Accelerating a FFT-based solver for numerical homogenization of periodic media by conjugate gradients, Journal of Computational Physics 229 (21) (2010) 8065–8071.

[93] C. Meng, M. Fehler, B. Hager, Elastic medium containing interacting fluid inclusions, Composite Structures 256 (2021) 113018.

[94] C. Meng, Extending Esh3D Code to Solve Interacting Eshelby's Inhomogeneity Problems, Earth and Space Science 6 (8) (2019) 1569–1577, ISSN 2333-5084, doi: 10.1029/2019EA000594.

[95] C. Meng, C. Gu, B. Hager, An Eshelby solution-based finite-element approach to heterogeneous fault-zone modeling, Seismological Research Letters 91 (1) (2020) 465–474.

[96] J. Kepler, Harmonice mundi (linz, 1619), English edition: Harmonies of the world, Book 5.

[97] B. Grnbaum, G. C. Shephard, Tilings and patterns, A Series of books in the mathematical sciences, W.H. Freeman, New York, ISBN 0-7167-1193-1, 1987.

[98] L. Leuzzi, G. Parisi, Thermodynamics of a tiling model, Journal of Physics A: Mathematical and General 33 (23) (2000) 4215.

[99] D. Aristoff, C. Radin, First order phase transition in a model of quasicrystals, Journal of Physics A: Mathematical and Theoretical 44 (2011) 255001.

[100] E. Winfree, F. Liu, L. A. Wenzler, N. C. Seeman, Design and self-assembly of two-dimensional DNA crystals, Nature 394 (6693) (1998) 539–544.

[101] P. W. Rothemund, N. Papadakis, E. Winfree, Algorithmic self-assembly of DNA Sierpinski triangles, PLoS Biol 2 (12) (2004) e424.

[102] E. Benson, A. Mohammed, J. Gardell, S. Masich, E. Czeizler, P. Orponen, B. Högberg, DNA rendering of polyhedral meshes at the nanoscale, Nature 523 (7561) (2015) 441–444.

[103] J. Stam, Aperiodic texture mapping, European Research Consortium for Informatics and Mathematics, 1997.

[104] J. Shade, M. F. Cohen, D. P. Mitchell, Tiling layered depth images .

[105] S. Hiller, O. Deussen, A. Keller, Tiled blue noise samples, in: Vision, Modeling, and Visualization (VMV), 2001.

[106] M. F. Cohen, J. Shade, S. Hiller, O. Deussen, Wang Tiles for image and texture generation, ACM Transactions on Graphics 22 (3) (2003) 287–294, ISSN 07300301, doi: 10.1145/882262.882265.

[107] A. A. Efros, W. T. Freeman, Image quilting for texture synthesis and transfer, in: Proceedings of ACM SIGGRAPH 2001, ACM Press, Los Angeles, ISBN 1-58113-374-X, 341–346, doi:10.1145/383259.383296, 2001.

[108] J. Kopf, D. Cohen-Or, O. Deussen, D. Lischinski, Recursive Wang tiles for real-time blue noise, vol. 25, ACM, 2006.

[109] A. Lagae, P. Dutré, An alternative for Wang tiles: colored edges versus colored corners, ACM Transactions on Graphics 25 (4) (2006) 1442–1459, ISSN 07300301, doi: 10.1145/1183287.1183296.

[110] L.-Y. Wei, Tile-based texture mapping on graphics hardware, in: Proceedings of the ACM SIGGRAPH/EUROGRAPHICS conference on Graphics hardware, ACM, 55–63, 2004.

[111] K. Culik, J. Kari, An Aperiodic Set of Wang Cubes, Journal of Universal Computer Science (10), ISSN 0948695X, doi:10.3217/jucs-001-10-0675.

[112] P. G. Sibley, P. Montgomery, G. E. Marai, Wang cubes for video synthesis and geometry placement, in: ACM SIGGRAPH 2004 Posters, ACM, 20, 2004.

[113] A. Lu, D. S. Ebert, W. Qiao, M. Kraus, B. Mora, Volume illustration using wang cubes, ACM Transactions on Graphics (TOG) 26 (2) (2007) 11.

[114] J. Novák, A. Kučerová, J. Zeman, Compressing random microstructures via stochastic Wang tilings, Physical Review E 86 (4), ISSN 1539-3755, 1550-2376, doi:10.1103/PhysRevE.86.040104.

[115] M. Doškář, J. Novák, J. Zeman, Aperiodic compression and reconstruction of real-world material systems based on Wang tiles, Physical Review E 90 (6) (2014) 062118, doi:10.1103/PhysRevE.90.062118.

[116] M. Doškář, J. Novák, A jigsaw puzzle framework for homogenization of high porosity foams, Computers & Structures 166 (2016) 33–41.

[117] M. Doškář, J. Zeman, D. Jarušková, J. Novák, Wang tiling aided statistical determination of the Representative Volume Element size of random heterogeneous materials, European Journal of Mechanics - A/Solids 70 (2018) 280–295, ISSN 09977538, doi:10.1016/j.euromechsol.2017.12.002.

[118] M. Doškář, J. Zeman, P. Krysl, J. Novák, Microstructure-informed reduced modes synthesized with Wang tiles and the Generalized Finite Element Method, Computational Mechanics 68 (2) (2021) 233–253, ISSN 0178-7675, 1432-0924, doi:10.1007/s00466-021-02028-y.

Chapter 2

MICROMECHANICS ENHANCED FINITE ELEMENT FORMULATION

The trigger for the work presented in this chapter was the analysis and design of particulate thermoplastic composites with short glass fiber reinforcement that would suit the injection molding fabrication, with foreseen target applications in automotive industry. The particular goal of related research agenda was the development of a methodology, experimental plus computational, to design thermoplastics' smeared reinforcement in such a way it would allow for earlier demolding of cast products during manufacturing, providing they will preserve their geometry unchanged. The later requirement was critical, as the earlier demolding is performed under higher temperatures than the conventional reinforcement-free thermoplastic products are able to sustain without substantial geometry deterioration. The motivation behind this development was fulled namely by the quest for energy efficient manufacturing processes and also by the financial saving promises due to the production speedup related to shorter cooling down periods of the molds. The theoretically and computationally oriented hypotheses on the crucial plastic deformation forming mechanisms were based on the detailed solution of local thermomechanical fields down to the microlevel, providing large macrolevel domains to be taken into account. The methodology proposed in the following chapter stems from the mixed Trefftz Finite Element formulation with local enrichment functions based on the Eshelby solution to a problem of ellipsoidal inhomogeneity embedded in infinite media exposed to a far-field strain excitation.

List of source journal papers and book chapters

Novák, J., Kaczmarczyk, Ł., Grassl, P., Zeman, J., and Pearce, C. J. (2012). A micromechanics-enhanced finite element formulation for modelling heterogeneous materials. *Computer Methods in Applied Mechanics and Engineering*, 201:53–64.

Pearce, C., Kaczmarczyk, L., and Novak, J. (2010). Multiscale modelling strategies for heterogeneous materials. In *Comuputational Technology Reviews*, volume 2, pages 23–49. Saxe-Coburg Publications.

A micromechanics-enhanced finite element formulation for modelling heterogeneous materials

Jan Novák

Experimental Centre, Faculty of Civil Engineering, Czech Technical University in Prague, Czech Republic

Łukasz Kaczmarczyk

School of Engineering, University of Glasgow, Glasgow G12 8QQ, UK

Peter Grassl

School of Engineering, University of Glasgow, Glasgow G12 8QQ, UK

Chris J. Pearce

School of Engineering, University of Glasgow, Glasgow G12 8QQ, UK

Jan Zeman

Department of Mechanics, Faculty of Civil Engineering, Czech Technical University in Prague, Czech Republic

Abstract

In the analysis of composite materials with heterogeneous microstructures, full resolution of the heterogeneities using classical numerical approaches can be computationally prohibitive. This paper presents a micromechanics-enhanced finite element formulation that accurately captures the mechanical behaviour of heterogeneous materials in a computationally efficient manner. The strategy exploits analytical solutions derived by Eshelby for ellipsoidal inclusions in order to determine the mechanical perturbation fields as a result of the underlying heterogeneities. Approximation functions for these perturbation fields are then incorporated into a finite element formulation to augment those of the macroscopic fields. A significant feature of this approach is that the finite element mesh does not explicitly resolve the heterogeneities and that no additional degrees of freedom are introduced. In this paper, hybrid-Trefftz stress finite elements are utilised and performance of the proposed formulation is demonstrated with numerical examples. The method is restricted here to elastic particulate composites with ellipsoidal inclusions but it has been designed to be extensible to a wider class of materials comprising arbitrary shaped inclusions.

Keywords: Micromechanics; Equivalent inclusion method; Eshelby's solution; Heterogeneous materials; Hybrid-stress finite elements; Displacement perturbations

Email addresses: novakja@fsv.cvut.cz (Jan Novák), lukasz@civil.gla.ac.uk (Łukasz Kaczmarczyk), grassl@civil.gla.ac.uk (Peter Grassl), pearce@civil.gla.ac.uk (Chris J. Pearce), jan.zeman@cvut.cz (Jan Zeman)

1. Introduction

In the analysis of materials with complex microstructures, full resolution of the heterogeneities using classical numerical approaches such as the Finite Element method can be computationally prohibitive. To overcome this, one option is to model the macroscale problem using equivalent properties; however, this can lead to a critical loss of information about the finer scale behaviour and poor understanding of the heterogeneities' influence on the macroscale response. Numerical approaches such as computational homogenization (often called FE^2) provide an alternative strategy [1, 2]. These techniques comprise nested Finite Element analyses, where each macroscopic material point response is determined via the numerical solution of an RVE subject to the macroscopic strains. Although such approaches have significant potential for certain classes of problems, they are still computationally demanding and are restricted to situations involving clear separation of scales.

The objective of this work is to develop a Finite Element formulation for modelling the macroscopic mechanical problem that is enhanced to capture the influence of the underlying heterogeneities. In our approach, the Finite Element mesh is not required to explicitly resolve the heterogeneities. Closed-form expressions for the perturbation of the mechanical fields due to the presence of the heterogeneities are determined and these are then utilised to enhance the Finite Element formulation.

The ability to capture the effect of microstructural features independently of the underlying finite element mesh has been an ongoing challenge in computational mechanics research. Partition of Unity methods [3, 4, 5, 6] provide a potential solution to this problem, without mesh refinement, by extending a given solution space with additional functions and has been successfully applied to problems such as cracks and material interfaces. The application of this approach in the context of the current work will be briefly discussed in this paper, whereby the closed-form solutions derived for the mechanical perturbation fields are used to extend the classical finite element method. However, it will be shown that there are some disadvantages to this approach for the particular problem at hand and an alternative approach, centred on the Hybrid-Trefftz stress element formulation [7], represents the main focus of this paper. This method does not result in additional degrees of freedom, although it does involve an additional, albeit relatively minor, computational overhead.

The heterogeneities, although currently restricted to simple shapes (ellipsoids), can be randomly sized and randomly distributed without reference to the finite element mesh. Therefore, the proposed approach has the potential to be applicable to a wide range of composite materials, such as fibre reinforced composites [8], porous media [9, 10], functionally graded materials [11], etc. Moreover, it can be extended to general inclusion shapes by evaluating the perturbation functions numerically [12, 13].

The paper is structured as follows. The methodology of the proposed strategy is described in **Section 2**. Construction of the perturbation approximation functions for Finite Element Analysis is derived in **Section 3**. The implementation into the Hybrid-Trefftz stress element formulation containing an arbitrary number of inclusions is presented in **Section 4**. **Section 5** comprises examples demonstrating the model's performance. Finally we present the conclusions as well as a discussion on future research directions. An appendix is included that highlights some important, but rather technical, aspects of the proposed technique in order to keep the paper self-contained.

2. Micromechanics approach

This section outlines the strategy to calculate the perturbation of mechanical fields due to a heterogeneous microstructure, exploiting the Equivalent Inclusion Method [14] in conjunction with analytical micromechanics. Our objective is to convert the heterogeneous problem into an equivalent homogeneous problem and to derive analytical expressions for the perturbations of the stress, strain and displacement fields that we can then utilise within a finite element formulation.

Consider a body consisting of clearly distinguishable heterogeneities in a matrix (Fig. 1a) subjected to a displacement $\overline{\mathbf{u}}$ and traction $\overline{\mathbf{t}}$ field. The stiffness of such a material is decom-

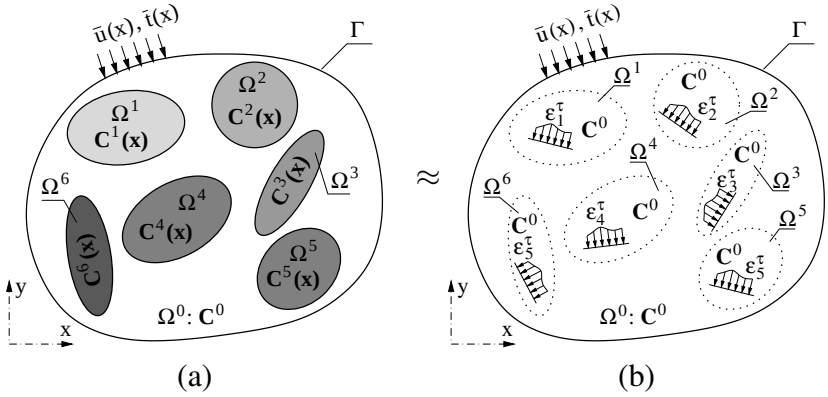

Figure 1: Principle of Equivalent Inclusion Method: a) composite body with inclusions, b) homogeneous reference body with additional equivalent eigenstrains

posed as follows [14, 13]

$$\mathbf{C} = \mathbf{C}^0 + V\mathbf{C}^* \tag{1}$$

where $\mathbf{C}^0$ is the stiffness tensor of a homogeneous matrix Ω^0 and $\mathbf{C}^* = \sum_i^N [\mathbf{C}^i - \mathbf{C}^0]$ is due to the presence of N inclusions. $\mathbf{C}^*$ is nonzero only within the domain $\Omega = \Omega^1 \cup \cdots \cup \Omega^N$, so that

$$V = \begin{cases} 0 \text{ in } \Omega^0 \\ 1 \text{ in } \Omega \end{cases} \tag{2}$$

As a result of the heterogeneities, the mechanical fields (displacement, strains, stresses) experience a perturbation for which we will derive closed-form expressions based on analytical micromechanics. Symbolically, we can express the decomposition of the mechanical fields as follows:

$$\mathbf{u} = \mathbf{u}^0 + \mathbf{u}^*, \quad \boldsymbol{\varepsilon} = \boldsymbol{\varepsilon}^0 + \boldsymbol{\varepsilon}^*, \quad \boldsymbol{\sigma} = \boldsymbol{\sigma}^0 + \boldsymbol{\sigma}^* \tag{3}$$

where, the superscript $\cdot^0$ indicates the macroscopic component of the fields in the absence of heterogeneities and superscript $\cdot^*$ indicates the perturbation (or microscopic) component due to the presence of the heterogeneities. It is worth noting that, traditionally, in analytical micromechanics, the macroscopic fields are assumed to be uniform across the domain, e.g. [15, 16]. Here it is assumed that they can be position dependent functions of the Neumann and Dirichlet boundary conditions.

The perturbation fields are determined by employing the equivalent inclusion method for a single heterogeneity embedded in a matrix and then extended here for multiple heterogeneities. In the equivalent inclusion method, the heterogeneous solid is replaced by an

equivalent homogeneous solid with uniform material stiffness $\mathbf{C}^0$ everywhere (Fig. 1a, b) and suitable stress-free eigenstrains $\boldsymbol{\varepsilon}_i^\tau$ applied in the inclusions Ω^i so that the homogeneous equivalent solid has the same mechanical fields as the original heterogeneous solid.

2.1. Equivalent inclusion method for single heterogeneity problem

Consider first a single heterogeneity embedded in a matrix. Following Eshelby's fundamental work [17], this problem can be decomposed into two problems of known solution and then assembled back via superposition [14, 17], see Fig. 2. In brief, the solution of the

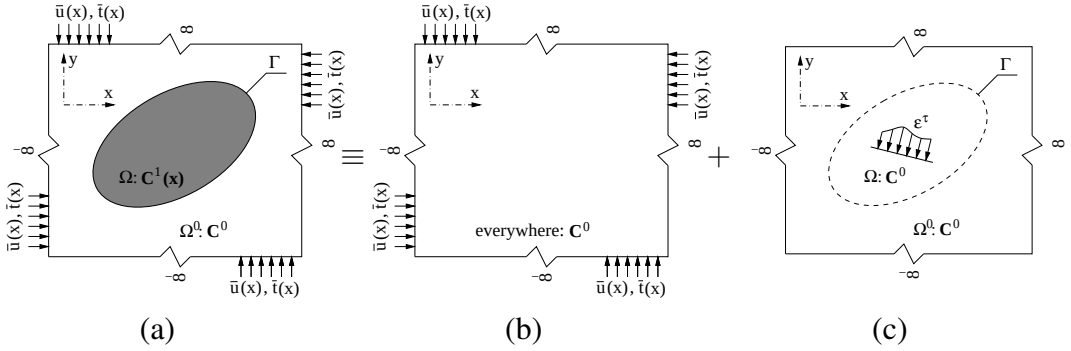

Figure 2: Equivalent Inclusion Method: a) inhomogeneity problem, b) infinite homogeneous body, c) homogeneous inclusion problem

inhomogeneity problem requires the determination of the transformation eigenstrain $\boldsymbol{\varepsilon}_i^\tau$ that induces the identical local mechanical response as the original heterogeneous body.

In the original heterogeneous body, the stress state can be expressed as

$$\boldsymbol{\sigma} = \boldsymbol{\sigma}^0 + \boldsymbol{\sigma}^* = \mathbf{C} : [\boldsymbol{\varepsilon}^0 + \boldsymbol{\varepsilon}^*] \tag{4}$$

In the homogeneous solid, we add a stress-free eigenstrain $\boldsymbol{\varepsilon}^\tau$ inside the domain of the inclusion, which has the same material stiffness $\mathbf{C}^0$ as the matrix such that

$$\boldsymbol{\sigma} = \mathbf{C}^0 : [\boldsymbol{\varepsilon}^0 + \boldsymbol{\varepsilon}^* - \boldsymbol{\varepsilon}^\tau] \tag{5}$$

It should be noted that $\boldsymbol{\varepsilon}^\tau = 0$ in the matrix.

Given that the macroscopic stress is $\boldsymbol{\sigma}^0 = \mathbf{C}^0 : \boldsymbol{\varepsilon}^0$, it can be see from equating Eqs. (4) and (5), that the stress perturbation in the homogeneous solid can be expressed as

$$\boldsymbol{\sigma}^* = \mathbf{C}^0 : [\boldsymbol{\varepsilon}^* - \boldsymbol{\varepsilon}^\tau] \tag{6}$$

Furthermore, equating Eqs. (4) and (5) also results in the following expression:

$$\mathbf{C} : [\boldsymbol{\varepsilon}^0 + \boldsymbol{\varepsilon}^*] = \mathbf{C}^0 : [\boldsymbol{\varepsilon}^0 + \boldsymbol{\varepsilon}^* - \boldsymbol{\varepsilon}^\tau] \tag{7}$$

where the transformation eigenstrain is as yet unknown. Eshelby's solution of the homogeneous inclusion problem [17], relates the eigenstrain to the perturbation strain as follows

$$\boldsymbol{\varepsilon}^* = \mathbf{S} : \boldsymbol{\varepsilon}^\tau \tag{8}$$

where $\mathbf{S}$ denotes the Eshelby tensor and is a function of the heterogeneity's geometry and the material stiffness of both the matrix and heterogeneity. Substituting this expression into Eq. (7) and rearranging yields

$$\left[\mathbf{C}-\mathbf{C}^0\right] : \boldsymbol{\varepsilon}^0 = \left[\mathbf{C}^0 : \mathbf{S} - \mathbf{C} : \mathbf{S} - \mathbf{C}^0\right] : \boldsymbol{\varepsilon}^\tau \tag{9}$$

This can be recast in a compact form to give an expression for the eigenstrain $\boldsymbol{\varepsilon}^\tau$ which depends on the homogeneous strain $\boldsymbol{\varepsilon}^0$, the material stiffness of both the matrix and heterogeneity and the Eshelby tensor as

$$\boldsymbol{\varepsilon}^\tau = \mathbf{B} : \boldsymbol{\varepsilon}^0 \tag{10}$$

where the tensor $\mathbf{B}$ is provided by:

$$\mathbf{B} = -\left[\mathbf{C}^* : \mathbf{S} + \mathbf{C}^0\right]^{-1} : \mathbf{C}^* \tag{11}$$

Once the transformation eigenstrain has been determined, the stress perturbation can be computed from Eq. (6) in the form

$$\boldsymbol{\sigma}^* = \mathbf{C}^0 : [\mathbf{S} - \mathbf{I}] : \mathbf{B} : \boldsymbol{\varepsilon}^0 \tag{12}$$

It can be seen that the stress perturbation depends on stiffness of the different material phases, the macroscopic strain field and the geometry of the heterogeneity. This closed-form expression for the stress perturbation is at the heart of the proposed finite element enrichment to be discussed later in this paper. It is also useful to derive an expression for the displacement perturbation field as follows

$$\mathbf{u}^* = \boldsymbol{\mathcal{L}} : \boldsymbol{\varepsilon}^\tau = \boldsymbol{\mathcal{L}} : \mathbf{B} : \boldsymbol{\varepsilon}^0 \tag{13}$$

where the operator $\boldsymbol{\mathcal{L}}$ is a third order tensor, mapping $\boldsymbol{\varepsilon}^\tau \rightarrow \mathbf{u}^*$. For the sake of conciseness and to keep the paper self-contained, the detailed derivation of this operator can be found in **Appendix Appendix A**.

2.2. Multiple inclusion problem via Self-balancing algorithm

In the case of multiple inclusions, the mechanical perturbation fields are essentially determined from the Eshelby solution for each individual inclusions, as described above. However, it is also necessary to introduce an iterative self-balancing procedure (Tab. 1) to ensure that the solution correctly reflects the influence of multiple inclusions.

This procedure iteratively modifies the eigenstrain inside any given inclusion i, to account for the influence of the remaining inclusions $N \backslash i$. First, the eigenstrain $\boldsymbol{\varepsilon}_i^\tau$ for each inclusion i is calculated (Eq. 10) without reference to the other inclusions (**Line 2**). Next, the associated perturbation strain $\boldsymbol{\varepsilon}_i^*$ for each inclusion i is evaluated (Eq. 8) at the centre of all other inclusions (**Line 3**).

The mutual interaction of inclusions is then taken into account via a correction of the eigenstrain ($\Delta\boldsymbol{\varepsilon}_i^\tau$). For each inclusion i, this correction is calculated (**Line 8**) from the inverse of the inclusion's Eshelby tensor $\mathbf{S}_i^{-1}$ and the perturbation strains of all other inclusions, evaluated at the centroid of inclusion i. The perturbation strain resulting from inclusion j at the centre of inclusion i is denoted as $\boldsymbol{\varepsilon}_{i,j}^*$. This is demonstrated in Fig. 3 for a two inclusion problem in 1D. The eigenstrain correction is then used to calculate the correction to the perturbation strains (**Line 11**). Finally, the perturbation strain is updated (**Line 12**).

The algorithm continues until a small Euclidean norm between the last two iterations of the total eigenstrains is achieved. At convergence, the corresponding stress and displacement perturbations are recalculated from the corrected transformation eigenstrains.

The computational complexity of this algorithm is $O(N^2)$. However, this can be improved by taking into account only those inclusions which have a non-negligible influence to the inclusion of interest i. This has been found to give a significant computational speed-up.

	Self Balancing Algorithm $(\boldsymbol{\varepsilon}_i^0, \mathbf{B}_i, \mathbf{S}_i, \mathbf{S}_i^{-1}, N)$
1	**For** $(i \leq N)$
2	$\quad \boldsymbol{\varepsilon}_i^\tau = \mathbf{B}_i : \boldsymbol{\varepsilon}_i^0$ (Eq. 10)
3	$\quad \boldsymbol{\varepsilon}_i^* = \mathbf{S}_i : \boldsymbol{\varepsilon}_i^\tau$ (Eq. 8)
4	$\quad$ **Set** $\Delta\boldsymbol{\varepsilon}_i^* = \boldsymbol{\varepsilon}_i^*$
5	**EndFor**
6	**Do**
7	$\quad$ **For** $(i \leq N)$
8	$\quad\quad \Delta\boldsymbol{\varepsilon}_i^\tau = \sum_{j\setminus i}^N \mathbf{S}_i^{-1} : \Delta\boldsymbol{\varepsilon}_{i,j}^*$ (Eq. 8)
9	$\quad\quad \boldsymbol{\varepsilon}_i^\tau = \boldsymbol{\varepsilon}_i^\tau + \Delta\boldsymbol{\varepsilon}_i^\tau$
10	$\quad\quad \Delta\boldsymbol{\varepsilon}_i^* = \mathbf{S}_i : \Delta\boldsymbol{\varepsilon}_i^\tau$
11	$\quad$ **EndFor**
12	**While** $\left(\sum_i^N \|\Delta\boldsymbol{\varepsilon}_i^*\| > \eta\right)$

Table 1: Self-balancing algorithm. Note, that η stands for an acceptable error.

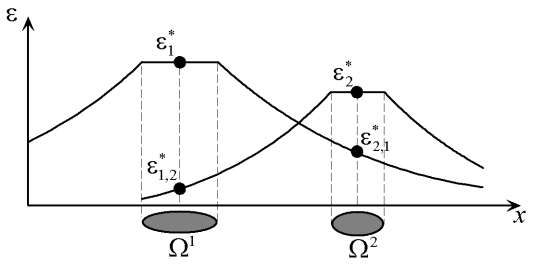

Figure 3: Principle of self-balancing algorithm for double inclusion problem in 1D.

3. Construction of perturbation approximation functions for FEA

The above methodology can be utilised to formulate an enhanced Finite Element formulation. The primary task is to determine appropriate approximation functions for the mechanical perturbation fields $\mathbf{u}^*$, $\boldsymbol{\varepsilon}^*$ and $\boldsymbol{\sigma}^*$ based on the analytical micromechanics developed above and which can then augment the standard macroscopic field approximations. It should be noted that the Voigt-Mandel notation is exclusively used in the forthcoming text.

The perturbation field approximation functions are determined a priori as a linear combination of the perturbation fields evaluated analytically for six load cases, with self-equilibrium enforced by means of the self-balancing algorithm outlined above (Tab. 1). Each load case corresponds to a unit component of the macroscopic strain vector $\epsilon_i^0,\ i = 1, \ldots, 6$ and the

resulting analytically determined stress, strain and displacement perturbation fields are arranged, column-by-column into $\mathfrak{s}^*_{6\times6}$, $\mathfrak{e}^*_{6\times6}$ and $\mathfrak{u}^*_{3\times6}$ matrices, respectively:

$$\mathfrak{s}^* = \left[\begin{array}{ccc} {}^1\sigma^* & \dots & {}^6\sigma^* \end{array} \right], \mathfrak{e}^* = \left[\begin{array}{ccc} {}^1\epsilon^* & \dots & {}^6\epsilon^* \end{array} \right] \tag{14}$$

$$\mathfrak{u}^* = \left[\begin{array}{ccc} {}^1\mathsf{u}^* & \dots & {}^6\mathsf{u}^* \end{array} \right] \tag{15}$$

where the left superscript refers to a specific load case, 1 to 6.

3.1. Partition of unity method

Partition of Unity (PU) Methods (for example the eXtended Finite Element Method) extend the underlying basis functions used for interpolating the displacement field by adding an appropriate set of additional functions. Following [18, 19] it has been shown that the displacement field $\mathsf{u}(\mathbf{x})$ within an element can be interpolated by

$$\mathsf{u}(\mathbf{x}) = \sum_{i=1}^{n} \left(\mathsf{N}^i(\mathbf{x})\mathsf{a}^i + \mathsf{N}^i\mathsf{N}_\gamma(\mathbf{x})\mathsf{b}^i \right) \tag{16}$$

where n is the number of nodes per element, $\mathsf{N}^i(\mathbf{x}) = N^i(\mathbf{x})\mathsf{I}$ is the standard matrix of element shape functions for node i, I is the identity matrix and a^i the standard displacement degrees of freedom at node i. N_γ is a matrix containing the additional basis terms and b^i are the associated additional degrees of freedom at node i. It is important to recognise that the element shape functions form a partition of unity, i.e.

$$\sum_{i=1}^{n} N^i(\mathbf{x}) = 1 \tag{17}$$

The six analytically derived displacement perturbation functions contained in $\mathfrak{u}^*$ can be used as the additional functions N_γ to augment the standard basis functions. Thus

$$\mathsf{N}_\gamma(\mathbf{x}) = \left[\begin{array}{cccccccccc} {}^1u_1^*(\mathbf{x}) & \dots & {}^6u_1^*(\mathbf{x}) & 0 & \dots & 0 & 0 & \dots & 0 \\ 0 & \dots & 0 & {}^1u_2^*(\mathbf{x}) & \dots & {}^6u_2^*(\mathbf{x}) & 0 & \dots & 0 \\ 0 & \dots & 0 & 0 & \dots & 0 & {}^1u_3^*(\mathbf{x}) & \dots & {}^6u_3^*(\mathbf{x}) \end{array} \right] \tag{18}$$

With this at hand, the PU-based finite element formulation can be derived, see for example [20]. PU methods are particularly useful in problems where the extension of the basis functions is introduced on a node by node basis, so that additional degrees of freedom are only introduced at nodes where the basis is extended. One obvious example of such a local feature that can be modelled in this way is discrete cracks [20]. However, this favourable property is not exploited here because we wish to model a large number of heterogeneities throughout the domain. In 3D problems, there are 3 standard displacement degrees of freedom per node; this would be extended by an additional 18 degrees of freedom per node with the proposed approach.

It is also worth noting that for standard finite elements, the volume integration of the discrete system of equations is relatively straightforward. However, extension of the basis functions to include the perturbation functions in Eq. (18) makes this process significantly more arduous. For these reasons, an alternative Finite Element approach using Hybrid Trefftz Stress elements [21, 7] is considered where the standard basis function is not extended, as with PU methods, but enhanced such that no additional degrees of freedom are introduced. This is described in the next section.

4. Hybrid-Trefftz stress element formulation

In this section a finite element formulation based on an enhancement of a hybrid-Trefftz stress (HTS) element formulation [7] is presented. The problem requires a solution to the dis-

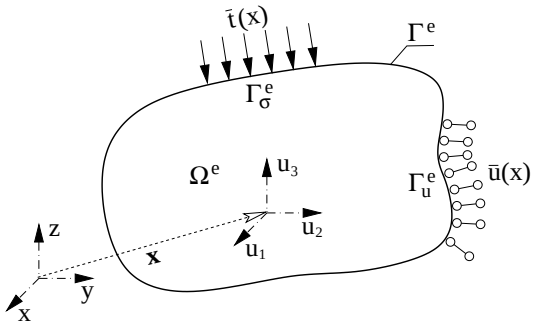

Figure 4: Elastic body representing HTS element

placement $\mathbf{u}$ and stress $\boldsymbol{\sigma}$ fields as a result of given boundary displacements $\overline{\mathbf{u}}$ and tractions $\overline{\mathbf{q}}$ on Γ_u^e and Γ_σ^e, respectively. The displacement and stress fields must fulfil the following governing equations:

$$\begin{array}{lll} \mathsf{L}^{\mathsf{T}}\sigma = 0 & \text{in } \Omega^e & \ldots \text{Cauchy equilibrium equation} \\ \mathsf{L}\mathsf{u} = \epsilon & \text{in } \Omega^e & \ldots \text{compatibility equation} \\ \sigma = \mathsf{C}\epsilon & \text{in } \Omega^e & \ldots \text{constitutive equation} \\ \mathsf{N}\sigma = \bar{\mathsf{t}} & \text{on } \Gamma_\sigma^e & \ldots \text{equilibrium equation on } \Gamma_\sigma^e \\ \mathsf{u} = \overline{\mathsf{u}} & \text{on } \Gamma_u^e & \ldots \text{compatibility equation on } \Gamma_u^e \end{array} \tag{19}$$

where σ and ϵ are the column matrix representation of the second order stress and strain tensor, respectively, u represents the displacement vector, C is the matrix representation of fourth order stiffness tensor and finally $\overline{\mathsf{u}}$ and $\bar{\mathsf{t}}$ represent the applied displacements and tractions, respectively. The gradient operator L and the matrix of directional cosines N of the outward normal to element boundary Γ^e have the following forms [22]

$$\mathsf{L} = \begin{bmatrix} \partial/\partial x & 0 & 0 \\ 0 & \partial/\partial y & 0 \\ 0 & 0 & \partial/\partial z \\ \partial/\partial y & \partial/\partial x & 0 \\ 0 & \partial/\partial z & \partial/\partial y \\ \partial/\partial z & 0 & \partial/\partial x \end{bmatrix}, \quad \mathsf{N} = \begin{bmatrix} n_x & 0 & 0 & 0 & n_z & n_y \\ 0 & n_y & 0 & n_z & 0 & n_x \\ 0 & 0 & n_z & n_y & n_x & 0 \end{bmatrix} \tag{20}$$

4.1. Stress, strain and displacement approximations

The macroscopic stress field within the HTS element is approximated as

$$\sigma^0 = \mathsf{S}_v^0 \mathsf{v} \text{ in } \Omega^e \tag{21}$$

where v is the vector of generalised stress degrees of freedom, S_v^0 denotes the matrix of stress approximation functions chosen so as to automatically satisfy the equilibrium conditions Eq. $(19)^{1,4}$. Thus,

$$\mathsf{L}^{\mathsf{T}}\mathsf{S}_v^0\mathsf{v} = \mathsf{0} \text{ in } \Omega^e \tag{22}$$

and

$$\mathsf{t} = \mathsf{N}\mathsf{S}_v^0\mathsf{v} \text{ on } \Gamma^e \tag{23}$$

where t represents the traction vector induced by the macroscopic stress approximation field.

The macroscopic strain and displacement fields are expressed analogously to Eq. (21) as

$$\epsilon^0 = \mathsf{E}_v^0\mathsf{v} \quad \text{and} \quad \mathsf{u}^0 = \mathsf{U}_v^0\mathsf{v} \tag{24}$$

where E_v^0 and U_v^0 are directly associated with the stress approximation by means of the compatibility equation $(19)^2$ and constitutive equation $(19)^3$ as

$$\mathsf{S}_v^0 = \mathsf{C}^0\mathsf{E}_v^0 = \mathsf{C}^0\mathsf{L}\mathsf{U}_v^0 \tag{25}$$

Since the stress approximation functions S_v^0 are typically polynomial functions, the integration of E_v^0 to get U_v^0 is relatively straightforward.

Rather than extend the solution space to capture the influence of the heterogeneities, as was briefly described in Section 3.1, here we enhance the macroscopic approximations to include the influence of the heterogeneities, thereby not increasing the number of unknowns. The total stress (macroscopic plus perturbation) field within the HTS element is approximated, following Eq. (3), as

$$\sigma = \sigma^0 + \sigma^* = \left(\mathsf{S}_v^0 + \mathsf{S}_v^*\right)\mathsf{v} \text{ in } \Omega^e \tag{26}$$

where S_v^* is the perturbation counterpart to S_v^0. S_v^* can be constructed from Eq. (14):

$$\sigma^* = \mathfrak{s}^*\epsilon^0 \tag{27}$$

where $\mathfrak{s}^*$ is the set of analytically defined stress perturbations for six load cases, each one representing a unit component of the macroscopic strain Eq. (14). For the purposes of constructing S_v^*, we approximate the macroscopic strain field as constant within each finite element and computed as the volume average of the actual macroscopic strain field. From Eq. (24),

$$\epsilon^{0,\text{ave}} = \frac{1}{|\Omega^e|}\int_{\Omega^e}\epsilon^0\,\mathrm{d}\Omega^e = \frac{1}{|\Omega^e|}\int_{\Omega^e}\mathsf{E}_v\,\mathrm{d}\Omega^e\mathsf{v} = \mathsf{E}_v^{\text{ave}}\mathsf{v} \tag{28}$$

Substituting $\epsilon^{0,\text{ave}}$ for ϵ^0 into Eq. (27) leads to

$$\sigma^* = \mathfrak{s}^*\mathsf{E}_v^{\text{ave}}\mathsf{v} \tag{29}$$

Thus, the matrix of stress perturbation approximation functions is:

$$\mathsf{S}_v^* = \mathfrak{s}^*\mathsf{E}_v^{\text{ave}} \tag{30}$$

Analogously, the approximation of total strain and displacement fields within the element domain is given by

$$\epsilon = \left(\mathsf{E}_v^0 + \mathsf{E}_v^*\right)\mathsf{v} \quad \text{and} \quad \mathsf{u} = \left(\mathsf{U}_v^0 + \mathsf{U}_v^*\right)\mathsf{v} \tag{31}$$

where the perturbation approximation matrices U_v^* and E_v^* are, as with their macroscopic counterparts, directly associated with the stress approximation as

$$\mathsf{S}_v^* = \mathsf{C}^0\mathsf{E}_v^* = \mathsf{C}^0\mathsf{L}\mathsf{U}_v^* \tag{32}$$

It is worthwhile noting that the stress perturbation fields and the corresponding traction perturbation fields, approximated as $\sigma^* = \mathsf{S}_v^*\mathsf{v}$ and $\mathsf{t}^* = \mathsf{N}\mathsf{S}_v^*\mathsf{v}$, remain in self-equilibrium.

4.2. Static boundary conditions

Contrary to general condition in Eq. (19)[4], the equilibrium on the element traction boundary is imposed only in the weighted residual sense as:

$$\int_{\Gamma_\sigma^e} \mathsf{W}_1^{\mathsf{T}} \left[\mathsf{N} \left(\sigma^0 + \sigma^* \right) - \bar{\mathsf{t}} \right] \, \mathrm{d}\Gamma^e = 0 \tag{33}$$

along with W_1 representing the matrix of weighting functions. Replacing the total stress field in Eq. (33) by its approximation from Eq. (26), the traction boundary condition becomes

$$\int_{\Gamma_\sigma^e} \mathsf{W}_1^{\mathsf{T}} \mathsf{N} \left(\mathsf{S}_v^0 + \mathsf{S}_v^* \right) \mathsf{v} \, \mathrm{d}\Gamma^e = \int_{\Gamma_\sigma^e} \mathsf{W}_1^{\mathsf{T}} \bar{\mathsf{t}} \, \mathrm{d}\Gamma^e \tag{34}$$

4.3. Kinematic boundary conditions

Compatibility inside the element domain Ω^e is also enforced in a weighted residual sense, such that:

$$\int_{\Omega^e} \mathsf{W}_2^{\mathsf{T}} \left(\epsilon^0 + \epsilon^* - \mathsf{L}\mathsf{u} \right) \, \mathrm{d}\Omega^e = 0 \tag{35}$$

Next, utilising integration by parts and applying Green's theorem to $\mathsf{W}_2^{\mathsf{T}}\mathsf{L}\mathsf{u}$, Eq. (35) results in

$$\begin{aligned} \int_{\Omega^e} \mathsf{W}_2^{\mathsf{T}} \left(\mathsf{E}_v^0 + \mathsf{E}_v^* \right) \mathsf{v} \, \mathrm{d}\Omega^e \quad &+ \quad \int_{\Omega^e} (\mathsf{L}^{\mathsf{T}}\mathsf{W}_2)^{\mathsf{T}} \mathsf{u} \, \mathrm{d}\Omega^e \\ &- \quad \int_{\Gamma_\sigma^e} (\mathsf{N}\mathsf{W}_2)^{\mathsf{T}} \, \mathsf{u} \, \mathrm{d}\Gamma^e = \int_{\Gamma_u^e} (\mathsf{N}\mathsf{W}_2)^{\mathsf{T}} \, \bar{\mathsf{u}} \, \mathrm{d}\Gamma^e \end{aligned} \tag{36}$$

With the current formulation, it is not necessarily possible to find a solution to both Eqs. (34) & (36) that satisfies both traction and kinematic boundary conditions acting on the element boundary. As a consequence, Eq. (36) is relaxed by introducing an additional and independent approximation of displacements on the element traction boundary:

$$\mathsf{u}_\Gamma = \mathsf{U}_\Gamma \mathsf{q} \text{ in } \Gamma_\sigma^e \tag{37}$$

where q stands for the set of displacement unknowns and U_Γ is the matrix of boundary displacement approximation functions. Such a formulation of the stress element leads to a hybrid approach [7, 21].

Given the above consideration, introducing Eq. (37) into Eq. (36) results in

$$\begin{aligned} \int_{\Omega^e} \mathsf{W}_2^{\mathsf{T}} \left(\mathsf{E}_v^0 + \mathsf{E}_v^* \right) \mathsf{v} \, \mathrm{d}\Omega^e \quad &+ \quad \int_{\Omega^e} (\mathsf{L}^{\mathsf{T}}\mathsf{W}_2)^{\mathsf{T}} \mathsf{u} \, \mathrm{d}\Omega^e \\ &- \quad \int_{\Gamma_\sigma^e} (\mathsf{N}\mathsf{W}_2)^{\mathsf{T}} \, \mathsf{u}_\Gamma \, \mathrm{d}\Gamma^e = \int_{\Gamma_u^e} (\mathsf{N}\mathsf{W}_2)^{\mathsf{T}} \, \bar{\mathsf{u}} \, \mathrm{d}\Gamma^e \end{aligned} \tag{38}$$

4.4. Weighting functions

In order to achieve an energy-consistent formulation, it is required that all weighted terms within the integrals defined above have the dimension of work. The weighting functions then directly follow from the integrands in Eq. (33) and Eq. (35) representing the increment of

internal work of strains within Ω^e and external work of tractions on Γ^e_σ, respectively. These functions thus admit the following forms:

$$\mathsf{W}_1 = \mathsf{U}_\Gamma, \qquad \mathsf{W}_2 = \mathsf{S}^0_v \tag{39}$$

First, introducing Eq. $(39)^2$ into Eq. (38) and taking into account condition (22) yields

$$\int_{\Omega^e} \left(\mathsf{S}^0_v\right)^\mathsf{T} \left(\mathsf{E}^0_v + \mathsf{E}^*_v\right) \mathsf{v}\, \mathrm{d}\Omega^e - \int_{\Gamma^e_\sigma} \left(\mathsf{N}\mathsf{S}^0_v\right)^\mathsf{T} \mathsf{U}_\Gamma \mathsf{q}\, \mathrm{d}\Gamma^e = \int_{\Gamma^e_u} \left(\mathsf{N}\mathsf{S}^0_v\right)^\mathsf{T} \bar{\mathsf{u}}\, \mathrm{d}\Gamma^e \tag{40}$$

Second, introducing Eq. $(39)^1$ into the traction boundary condition (34) yields

$$\int_{\Gamma^e_\sigma} \mathsf{U}^\mathsf{T}_\Gamma \mathsf{N}(\mathsf{S}^0_v + \mathsf{S}^*_v)\mathsf{v}\, \mathrm{d}\Gamma^e = \int_{\Gamma^e_\sigma} \mathsf{U}^\mathsf{T}_\Gamma \bar{\mathsf{t}}\, \mathrm{d}\Gamma^e \tag{41}$$

Combining Eqs. (40) & (41) results in a coupled system of linear equations that can be expressed in compact form as

$$\begin{bmatrix} \mathsf{F} & -\mathsf{A}^\mathsf{T} \\ -(\mathsf{A}+\mathsf{A}^*) & 0 \end{bmatrix} \begin{bmatrix} \mathsf{v} \\ \mathsf{q} \end{bmatrix} = \begin{bmatrix} \mathsf{p}_\mathsf{u} \\ -\mathsf{p}_\sigma \end{bmatrix} \tag{42}$$

where the submatrices on the left-hand side follow from Eqs (40, 41) and are given by the following integrals

$$\mathsf{F} = \int_{\Omega^e} \left(\mathsf{S}^0_v\right)^\mathsf{T} \left(\mathsf{E}^0_v + \mathsf{E}^*_v\right)\, \mathrm{d}\Omega^e = \int_{\Gamma^e} \mathsf{N} \left(\mathsf{S}^0_v\right)^\mathsf{T} \left(\mathsf{U}^0_v + \mathsf{U}^*_v\right)\, \mathrm{d}\Gamma^e \tag{43}$$

$$\mathsf{A} = \int_{\Gamma^e_\sigma} \mathsf{U}_\Gamma \mathsf{N}\mathsf{S}^0_v\, \mathrm{d}\Gamma^e \quad \text{and} \quad \mathsf{A}^* = \int_{\Gamma^e_\sigma} \mathsf{U}_\Gamma \mathsf{N}\mathsf{S}^*_v\, \mathrm{d}\Gamma^e \tag{44}$$

and for the terms on the right-hand side it holds

$$\mathsf{p}_\mathsf{u} = \int_{\Gamma^e_u} \left(\mathsf{N}\mathsf{S}^0_v\right)^\mathsf{T} \bar{\mathsf{u}}\, \mathrm{d}\Gamma^e, \text{ and } \quad \mathsf{p}_\sigma = \int_{\Gamma^e_\sigma} \mathsf{U}^\mathsf{T}_\Gamma \bar{\mathsf{t}}\, \mathrm{d}\Gamma^e \tag{45}$$

Note that Eq. (43) illustrates that the F matrix can be evaluated via a boundary rather than volume integral. Thus all terms in Eq. (42) can be evaluated using boundary integrals only. The size of the system of equations to be solved simultaneously can be reduced via static condensation, representing a significant reduction in computational effort. First, from the first equation in Eq. (42), the generalised stress degrees of freedom v are expressed in terms of the displacement degrees of freedom q as

$$\mathsf{v} = \mathsf{F}^{-1}(\mathsf{p}_\mathsf{u} + \mathsf{A}^\mathsf{T}\mathsf{q}) \tag{46}$$

This is then substituted into the second equation of Eq. (42) to yield:

$$((\mathsf{A}+\mathsf{A}^*)\mathsf{F}^{-1}\mathsf{A}^\mathsf{T})\mathsf{q} = \mathsf{p}_\sigma - (\mathsf{A}+\mathsf{A}^*)\mathsf{F}^{-1}\mathsf{p}_\mathsf{u} \tag{47}$$

This sparse system of equations is then solved for the displacement degrees of freedom q. Subsequently, the stress degrees of freedom v can then be calculated on an element-by-element basis.

Our implementation of these HTS elements for composite materials (C-HTS elements) utilises displacement degrees of freedom that are associated with element faces rather than vertices. This has the advantage that the bandwidth of the stiffness matrix is minimised, as is interprocessor communication.

5. Numerical Examples

The performance of the key components of the proposed strategy (micromechanical solution, self-balancing algorithm, finite element analysis convergence, etc.), in terms of efficiency and accuracy, have been explored through two numerical examples.

5.1. Three ellipsoidal inclusions in matrix

This example comprises three ellipsoidal inclusions embedded in a cube of matrix. The geometry of the problem is illustrated in Fig. 5 and details of the ellipsoids are given in Table 2, including the semi-axes' dimensions, centroid coordinates and Euler angles ϕ, ν and ψ, which are successive rotations of the semi-axes a_1, a_2 and a_3 about global coordinate axes z, x and z, respectively. The cube has side lengths of 600. The displacement boundary conditions were prescribed on faces $x = 300$, $y = 300$ and $z = 300$ as $\overline{u}_x = 0$, $\overline{u}_y = 0$ and $\overline{u}_z = 0$, respectively. The remaining faces at $x = -300$, $y = -300$ and $z = -300$ were subject to uniform normal unit tractions. The Young's modulus for the homogeneous matrix was chosen as $E = 1$ and for the heterogeneities as $E = 2$. Poisson's ratio was chosen as $\nu = 0.1$ for both materials. All units are consistent.

It is worthwhile noting that the small contrast in stiffness between the two materials was chosen deliberately to maximise the extent of the perturbation fields emanating from the heterogeneities. Large contrasts in stiffness between the matrix and heterogeneities lead to perturbation fields that decay rapidly with distance from the heterogeneities. The close proximity of the three ellipsoidal heterogeneities to each other was also chosen deliberately in order to demonstrate the ability of the formulation to capture the interaction of multiple heterogeneities. Furthermore, the close proximity of one of the ellipsoids to a traction boundary was chosen to demonstrate the ability of the formulation to capture boundary effects.

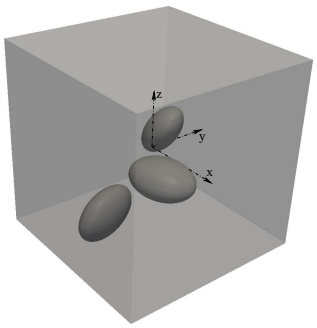

Figure 5: Geometry and topology of triple inclusion problem

Incl.	Centroid coordinates			Semiaxes dim.			Euler angles of $\max a_i$		
	x	y	z	a_1	a_2	a_3	ϕ	ν	ψ
1	-48.07	78.27	14.81	50	75	100	74.21	48.44	-48.07
2	16.45	178.64	-154.51	50	100	75	37.27	22.27	-25.51
3	127.93	-65.94	-27.32	100	75	50	46.74	11.17	-26.30

Table 2: Topology and geometry of ellipsoidal inclusions of triple inclusion problem

The problem was analysed using two three-dimensional finite element meshes with different densities, comprising C-HTS elements. The coarse mesh comprised 24 elements and

540 DOFs (Fig. 6a) and the second, refined, mesh comprised 192 elements and 3888 DOFs (Fig. 6b). Results from the two enhanced finite element analyses are plotted in the yz-plane

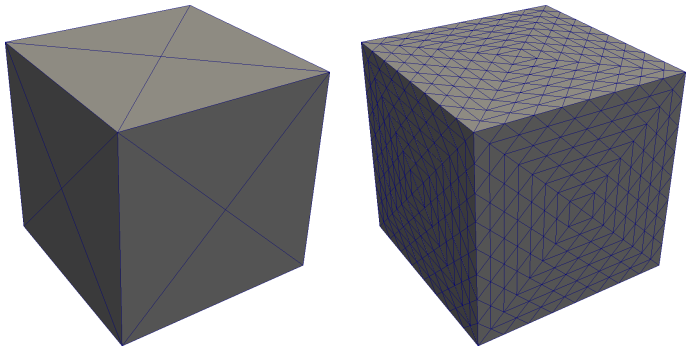

(a) (b)

Figure 6: Triple inclusion task discretization by C-HTS elements: a) Coarse mesh with 24 enhanced elements (540 DOFs) b) Finer mesh with 1,536 enhanced elements (29,376 DOFs)

(at $x = 0$). Fig. 7a and Fig. 8a show the two meshes in this plane. The σ_{yy} stress component for both analyses are shown in Fig. 7b and Fig. 8b.

In addition, a reference finite element analysis of the same problem was undertaken for comparison sake. The reference analysis utilised HTS elements but without the proposed enhancement. Unlike the other two analyses, the reference analysis utilised a mesh that explicitly resolved the three ellipsoidal heterogeneities and comprised $309,406$ tetrahedrons with $5,596,776$ DOFs (Fig. 9a). The corresponding mesh and stress results of the reference analysis are shown in Fig. 9. Comparison of the stress results from the enhanced formulation and the reference analysis leads to the relative error plots shown in Fig. 7c and Fig. 8c. It can be seen that even the very coarse mesh with the enhanced formulation results in good agreement.

Further comparison of the stress results is shown in Fig. 10, where it can been seen that along the traction boundary, the finer mesh of enhanced elements is able to capture the imposed constant stress field more accurately than the very much finer reference mesh.

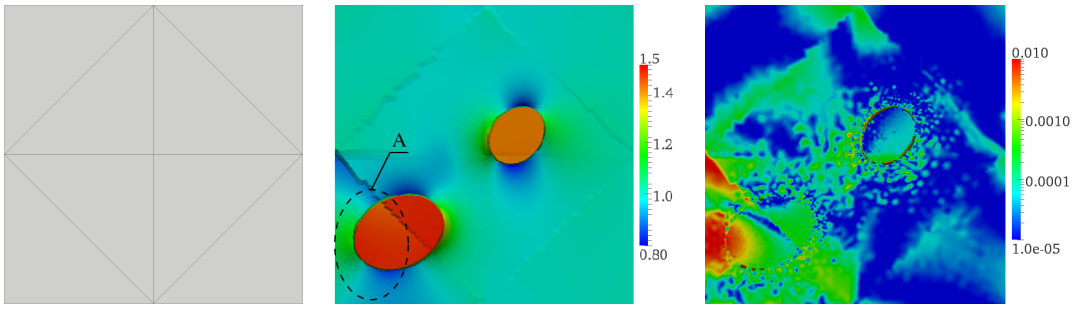

(a) (b) (c)

Figure 7: Coarse mesh solution: a) Enhanced finite element mesh in yz plane at $x = 0$, b) σ_{yy} in yz plane, c) error calculated as $(\sigma_{yy}^{\text{ref}} - \sigma_{yy})^2/\sigma_{yy}^2$

The perturbation fields are based on the assumption of a heterogeneity in an infinite medium but the enhanced formulation still exhibits convergence in the regions strongly influenced by the traction boundary.

(a) (b) (c)

Figure 8: Finer mesh solution: a) Enhanced finite element mesh in yz plane at $x = 0$, b) σ_{yy} in yz plane, c) error calculated as $(\sigma_{yy}^{\text{ref}} - \sigma_{yy})^2/\sigma_{yy}^2$

(a) (b)

(c) (d)

Figure 9: Reference analysis: a) discretization of entire body containing 309,406 tetrahedra, b) mesh refinement on surface of heterogeneities, c) Reference finite element mesh in yz plane at $x = 0$, d) σ_{yy}^{ref} in yz plane.

5.2. L-shaped specimen

The proposed modelling strategy is also demonstrated on an example with a large number of inclusion. A 3D L-shaped specimen with fully fixed boundary conditions on the right surface of the right-hand arm and normal traction applied on the top surface of the left-hand arm is analysed, see Fig. 11. The length of the plate is 300 in both x and y direction, the depth is 150 in z direction. The Young moduli were chosen as $E = 1$ and $E = 2$ for matrix and inclusion respectively. Poisson's ratio was $\nu = 0.1$ for both material phases. The microstructure comprised 2,523 spherical inclusions varying in size between 4 and 8 with a uniform spatial distribution (Fig. 11b). All units are consistent.

The solution for three different mesh densities (Fig. 11c, d & e) are compared in Fig. 12.

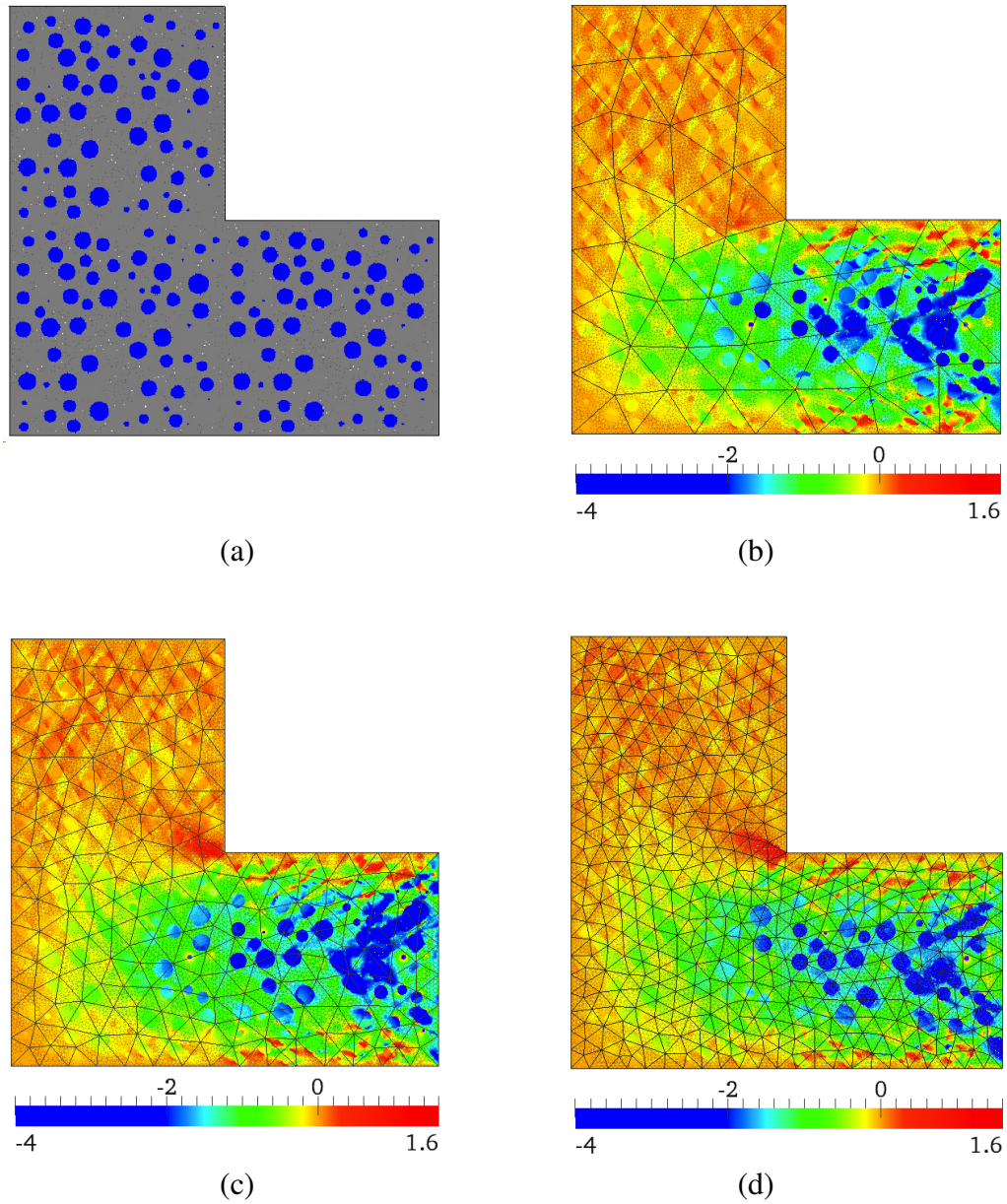

Figure 12: Solution of L-shaped specimen on x-y mid-plane. a) microstructure. Plots of σ_{xy} resulting from b) coarse mesh, c) medium mesh and d) fine mesh.

6. Conclusions

A new micromechanics-enhanced finite element formulation has been presented for modelling the influence of a large number of heterogeneities in composite materials in a computationally efficient manner. The strategy exploits closed form solutions derived by Eshelby for ellipsoidal inclusions in order to determine the mechanical perturbation fields as a result of the underlying heterogeneities. Approximation functions for these perturbation fields are then incorporated into a finite element formulation to augment those of the macroscopic fields. A significant feature of this approach is that the finite element mesh does not explicitly resolve the heterogeneities.

The proposed technique has been implemented into a hybrid-Trefftz stress (HTS) element

formulation and it has been shown that the resulting enhanced elements (C-HTS) require significantly fewer degrees of freedom to capture the detailed mechanical response compared to standard finite elements. The paper also demonstrates how the proposed micromechanics approach could be used within a Partition-of-Unity (PoU) formulation, although we conclude that this does not fully exploit the advantages of PoU methods and that the proposed hybrid-Trefftz formulation is most appropriate.

A self-balancing algorithm is used to determine the mutual interactions between inclusions, assuming that the eigenstrain fields are uniform within the domain of each inclusion. It was found that even for topologies exhibiting extremely small distances between the inclusions, this assumption is sufficient. Furthermore, it has been shown that boundary effects, that are not accounted for by the classical micromechanical solution due to the assumption of an infinite medium, can be captured through local mesh refinement.

We have implemented this formulation into our FE code that is optimized for parallel computing. Additional parallelization of the micromechanical aspects of the formulation needs to be investigated for increased efficiency. Further research is required in order to incorporate other improvements such as nonuniform eigenstrains [14] and debonding effects [23].

Acknowledgements

Funding by the Glasgow Research Partnership in Engineering (GRPE) under project "Multi-scale modelling of fibre reinforced composites" is gratefully acknowledged. This research was partially supported by the Czech Science Foundation trough project GAČR 103/09/P490 and by the Ministry of Education, Youth and Sports of the Czech Republic trough project MSM 684077003. All the analyses were performed by means of **YAFFEMS** FE code. For more details we refer to the code's homepage at `http://code.google.com/p/yaffems`.

Appendix A. Detailed solution of perturbation displacements

The displacement perturbation field in an infinite homogeneous material due to an uniform eigenstrain ε^{τ}_{ij} applied to an ellipsoidal region Ω is provided by the following integral equation [14, Eq. (11.30)]

$$u^{*}_{i} = \frac{1}{8\pi(1-\nu)} \left[\Psi_{jk,jki} - 2\nu\Phi_{kk,i} - 4(1-\nu)\Phi_{ik,k}\right] \tag{A.1}$$

where ν denotes the Poisson ratio and the elliptic potentials Ψ_{ij} and Φ_{ij} are defined as [14, Eq. (11.32)]

$$\Psi_{ij} = \varepsilon^{\tau}_{ij} \int_{\Omega} |\mathbf{x} - \mathbf{x}'| \, \mathrm{d}\mathbf{x}' = \varepsilon^{\tau}_{ij}\psi, \quad \text{and} \quad \Phi_{ij} = \varepsilon^{\tau}_{ij} \int_{\Omega} \frac{1}{|\mathbf{x} - \mathbf{x}'|} \, \mathrm{d}\mathbf{x}' = \varepsilon^{\tau}_{ij}\phi \tag{A.2}$$

The integrals ϕ and ψ in Eq. (A.2) are the harmonic and bi-harmonic potentials respectively. Note that in Eq. (A.1) and thereafter, standard index notation is employed, together with the generalised summation convection due to Mura [14]. Thus, a repeated index is summed according to the Einstein summation rule (e.g. $a_i b_{ij} = \sum_{i=1}^{3} a_i b_j$), whereas a non-repeated upper-case index equals to the lower-case equivalent (e.g. $a_i b_i c_{Ij} = \sum_{i=1}^{3} a_i b_i c_{ij}$). The symbol $a_{jk,i}$ denotes the partial derivative of a_{jk} with respect to the coordinate x_i.

By combining Eq. (A.1) and Eq. (A.2), we obtain

$$u_i^* = \frac{1}{8\pi(1-\nu)}\left[\varepsilon_{jk}^{\tau}\psi_{,jki} - 2\nu\delta_{jk}\varepsilon_{jk}^{\tau}\phi_{,i} - 4(1-\nu)\delta_{ij}\varepsilon_{jk}^{\tau}\phi_{,k}\right] \tag{A.3}$$

Similarly to Eshelby's approach [17] , the displacement perturbations are expressed in compact form:

$$u_i^* = L_{ijk}^{\varepsilon}\varepsilon_{jk}^{\tau}, \qquad L_{ijk}^{\varepsilon} = \frac{1}{8\pi(1-\nu)}\left[\psi_{,jki} - 2\nu\delta_{jk}\phi_{,i} - 4(1-\nu)\delta_{ij}\phi_{,k}\right] \tag{A.4}$$

where the third-order operator L_{ijk} maps a transformation eigenstrain ε_{jk}^{τ} to the displacement perturbation field u_i^*. It is therefore analogous to the well-known Eshelby tensor [17], which relates a transformation eigenstrain to the strain perturbation field.

The operator L_{ijk} can be conveniently expressed in terms of the Ferrers-Dyson elliptic integrals, e.g. [14, Eq. (11.36)]

$$\begin{aligned} I(\lambda) &= 2\pi a_1 a_2 a_3 \int_{\lambda}^{\infty} \frac{\mathrm{d}s}{\Delta(s)}, \\ I_i(\lambda) &= 2\pi a_1 a_2 a_3 \int_{\lambda}^{\infty} \frac{\mathrm{d}s}{(a_i^2+s)\Delta(s)}, \\ I_{ij}(\lambda) &= 2\pi a_1 a_2 a_3 \int_{\lambda}^{\infty} \frac{\mathrm{d}s}{(a_i^2+s)(a_j^2+s)\Delta(s)} \end{aligned} \tag{A.5}$$

where a_i stands for the i-th semi-axis of ellipsoid Ω and $\Delta(s)$ is obtained from

$$\Delta^2(s) = \prod_{i=1}^{3}(a_i+s)^2 \tag{A.6}$$

The variable λ is the largest positive root of equation [14, Eq. (11.37)]

$$\frac{x_i x_i}{(a_I+\lambda)^2} = 1 \tag{A.7}$$

Notice that λ and is generally position dependent and non-zero for the points x_i placed outside the inclusion domain Ω, hence called the exterior points. Contrary, $\lambda = 0$ for interior points.

All integrals in (A.5) admit a closed-form expression in terms of the Legendre-Jacobi integrals of the first and second kind, defined as a fuction of an auxiliary angle θ, [14, Eq. (12.17)]. It is worth noting that its definition via [14, Eq (11.18)]

$$\theta = \sin^{-1}\sqrt{1-\frac{a_3^2}{a_1^2}} \tag{A.8}$$

is valid for interior points only and and not everywhere as stated in [14]. Thus, it needs to be replaced with a general formula:

$$\theta = \sin^{-1}\sqrt{\frac{a_1^2-a_3^2}{a_1^2+\lambda}} \tag{A.9}$$

available, e.g. in [24, 25]. Moreover, the following identity [14, Eq. (11.40.4)]

$$[x_n x_n I_{i\ldots jN}(\lambda)]_{,p} = 2x_p I_{i\ldots jP} + I_{i\ldots j,p}(\lambda) \tag{A.10}$$

will be repeatedly proved useful in the sequel.

It follows from Eq. (A.4) that to express operator L^{ε}_{ijk}, we need to evaluate the first-order derivatives of the potential ϕ and the third-order derivatives of ψ. To this end, we start with expressions [14, Eq. (11.38)]

$$\phi(\lambda) = \tfrac{1}{2}\left[I(\lambda) - x_n x_n I_N(\lambda)\right] \tag{A.11}$$

and

$$\psi_{,i}(\lambda) = \tfrac{1}{2} x_i \Big\{ 2\phi(\lambda) - a_I^2 \left[I_I(\lambda) - x_n x_n I_{IN}(\lambda)\right] \Big\} = \tfrac{1}{2} x_i Q(\lambda) \tag{A.12}$$

Employing Eq. (A.10), the first derivative of ϕ becomes

$$\phi_{,i}(\lambda) = \tfrac{1}{2}\left\{ I_{,i}(\lambda) - \left[x_n x_n I_N(\lambda)\right]_{,i} \right\} = \tfrac{1}{2}\left[I_{,i}(\lambda) - 2x_i I_I(\lambda) - I_{,i}(\lambda)\right] = -x_i I_I(\lambda) \tag{A.13}$$

The third derivative of potential ψ is expressed from Eq. (A.12) as

$$\psi_{,ijk}(\lambda) = \tfrac{1}{2}\left[\delta_{ij} Q_{,k}(\lambda) + \delta_{ik} Q_{,j}(\lambda) + x_i Q_{,jk}(\lambda)\right] \tag{A.14}$$

With the help of Eqs. (A.13) and (A.10), the term $Q_{,j}$ can be evaluated from

$$Q_{,j}(\lambda) = 2\phi_{,j}(\lambda) - a_I^2 \left[I_I(\lambda) - x_n x_n I_{IN}(\lambda)\right]_{,j} = 2x_j \left[a_I^2 I_{IJ}(\lambda) - I_J(\lambda)\right] \tag{A.15}$$

This provides the second derivatives of Q in the form

$$Q_{,jk}(\lambda) = 2\Big\{ \delta_{jk} \left[a_I^2 I_{IJ}(\lambda) - I_J(\lambda)\right] + x_j \left[a_I^2 I_{IJ,k}(\lambda) - I_{J,k}(\lambda)\right] \Big\} \tag{A.16}$$

After utilising the derivatives of $Q(\lambda)$ and re-ordering the indices, Eq. (A.14) becomes

$$\begin{aligned} \psi_{jki}(\lambda) = {} & x_i \delta_{jk} \left[a_J^2 I_{JI}(\lambda) - I_I(\lambda)\right] + x_k \delta_{ji} \left[a_J^2 I_{JK}(\lambda) - I_K(\lambda)\right] \\ & + x_j \delta_{ki} \left[a_J^2 I_{JK}(\lambda) - I_K(\lambda)\right] + x_j x_k \left[a_J^2 I_{JK,i}(\lambda) - I_{K,i}(\lambda)\right] \end{aligned} \tag{A.17}$$

with $I_{IJ,k}$ and $I_{I,j}$ provided by [14, Eqs. (11.40.1, 11.40)]

$$\begin{aligned} I_{i\ldots jk,p}(\lambda) &= \frac{-2\pi a_1 a_2 a_3}{(a_i^2+\lambda)\ldots(a_j^2+\lambda)(a_k^2+\lambda)\Delta(\lambda)} \lambda_{,p}, \\ \lambda_{,p} &= \frac{2x_p}{a_P^2+\lambda} \frac{(a_I^2+\lambda)^2}{x_i x_i} \end{aligned} \tag{A.18}$$

Now we are in a position to evaluate L^{ε}_{ijk} in terms of the Ferrers-Dyson integrals. Introducing Eqs. (A.13) and (A.17) into Eq. (A.4) gives

$$\begin{aligned} [8\pi(1-\nu)]\, L^{\varepsilon}_{ijk} = {} & x_i \delta_{jk} \left[a_J^2 I_{JI}(\lambda) - I_I(\lambda)\right] + (x_k \delta_{ji} + x_j \delta_{ki}) \left[a_J^2 I_{JK}(\lambda) - I_K(\lambda)\right] \\ & + x_j x_k \left[a_J^2 I_{JK,i}(\lambda) - I_{K,i}(\lambda)\right] + 2\nu \delta_{jk} x_i I_I(\lambda) + 4(1-\nu)\delta_{ij} x_k I_K(\lambda) \Big\} \end{aligned} \tag{A.19}$$

Since $\lambda = 0$ for the points inside the inclusion, recall Eq. (A.7), all derivatives of $I_{i\ldots j}$ vanish as well. Therefore, Eq. (A.19) yields

$$\begin{aligned}\left[8\pi(1-\nu)\right] L^{\varepsilon,\mathrm{int}} = {} & x_i\delta_{jk}\left[a_J^2 I_{JI}(\lambda) - I_I(\lambda)\right] + (x_k\delta_{ji} + x_j\delta_{ki})\left[a_J^2 I_{JK}(\lambda) - I_K(\lambda)\right] \\ & + \nu\delta_{jk}x_i I_I(\lambda) + 4(1-\nu)\delta_{ij}x_k I_K(\lambda)\end{aligned} \tag{A.20}$$

and Eq. (A.4) receives its final form

$$L^{\varepsilon}_{ijk} = L^{\varepsilon,\mathrm{int}}_{ijk} + \frac{1}{8\pi(1-\nu)} x_j x_k \left[a_J^2 I_{JK,i}(\lambda) - I_{K,i}(\lambda)\right] \tag{A.21}$$

For implementation purposes, it is worth noting that Eq. (A.4) admits the Voigt representation:

$$\begin{Bmatrix} u_1^* \\ u_2^* \\ u_3^* \end{Bmatrix} = \begin{bmatrix} L_{111} & L_{122} & L_{133} & L_{112} & L_{123} & L_{113} \\ L_{211} & L_{222} & L_{233} & L_{212} & L_{223} & L_{213} \\ L_{311} & L_{322} & L_{333} & L_{312} & L_{323} & L_{313} \end{bmatrix} \begin{Bmatrix} \varepsilon_{11}^{\tau} \\ \varepsilon_{22}^{\tau} \\ \varepsilon_{33}^{\tau} \\ 2\varepsilon_{12}^{\tau} \\ 2\varepsilon_{23}^{\tau} \\ 2\varepsilon_{13}^{\tau} \end{Bmatrix} \tag{A.22}$$

[1] F. Feyel, J.-L. Chaboche, FE^2 multiscale approach for modelling the elastoviscoplastic behaviour of long fibre SiC/Ti composite materials, Computer Methods in Applied Mechanics and Engineering 183 (3-4) (2000) 309 – 330.

[2] M. Geers, V. Kouznetsova, W. Brekelmans, Multi-scale computational homogenization: Trends and challenges, Journal of Computational and Applied Mathematics 234 (2010) 2175 – 2182.

[3] N. Sukumar, D. Chopp, N. Moës, T. Belytschko, Modeling holes and inclusions by level sets in the extended finite-element method, Computer Methods in Applied Mechanics and Engineering 190 (46–47) (2001) 6183–6200.

[4] N. Moës, J. Dolbow, T. Belytschko, A finite element method for crack growth without remeshing, International Journal for Numerical Methods in Engineering 46 (1) (1999) 131–150.

[5] N. Moës, M. Cloirec, P. Cartraud, J.-F. Remacle, A computational approach to handle complex microstructure geometries, Computer Methods in Applied Mechanics and Engineering 192 (28–30) (2003) 3163–3177.

[6] G. Wells, L. Sluys, R. D. Borst, Simulating the propagation of displacement discontinuities in a regularised strain-softening medium, International Journal for Numerical Methods in Engineering 53 (5) (2002) 1235–1256.

[7] L. Kaczmarczyk, C. J. Pearce, A corotational hybrid-Trefftz stress formulation for modelling cohesive cracks, Computer Methods in Applied Mechanics and Engineering 198 (15-16) (2009) 1298 – 1310. doi:DOI:10.1016/j.cma.2008.11.018.

[8] P. Kabele, Multiscale framework for modeling of fracture in high performance fiber reinforced cementitious composites, Engineering Fracture Mechanics 74 (1-2) (2007) 194 – 209, fracture of Concrete Materials and Structures. doi:DOI:10.1016/j.engfracmech.2006.01.020.

[9] P. Nicolaou, S. Semiatin, A hybrid micromechanical-macroscopic model for the analysis of the tensile behavior of cavitating materials, Metallurgical and Materials Transactions A 35 (13) (2004) 1141–1149.

[10] A. Fritsch, C. Hellmich, L. Dormieux, Ductile sliding between mineral crystals followed by rupture of collagen crosslinks: Experimentally supported micromechanical explanation of bone strength, Journal of Theoretical Biology 260 (2) (2009) 230 – 252. doi:DOI:10.1016/j.jtbi.2009.05.021.

[11] Z. Sharif-Khodaei, J. Zeman, Microstructure-based modeling of elastic functionally graded materials: One dimensional case, Journal of Mechanics of Materials and Structures 3 (2008) 1773–1796. arXiv:0802.0511.

[12] V. Maz'ya, G. Schmidt, Approximate approximations, American Mathematical Society, Providence, RI, 2007.

[13] J. Novák, Calculation of elastic stresses and strains inside a medium with multiple isolated inclusions, in: M. Papadrakakis, B. Topping (Eds.), Proceedings of the Sixth International Conference on Engineering Computational Technology, Stirlingshire, UK, 2008, p. 16 pp, paper 127. doi:10.4203/ccp.89.127.

[14] T. Mura, Micromechanics of Defects in Solids., Martinus Nijhoff Publishers, P. O. Box 163, 3300 AD Dordrecht, The Netherlands, 1987. 587.

[15] J. Vorel, M. Šejnoha, Evaluation of homogenized thermal conductivities of imperfect carbon-carbon textile composites using the mori-tanaka method, Structural Engineering and Mechanics 33 (4) (2009) 429–446.

[16] B. Pichler, S. Scheiner, C. Hellmich, From micron-sized needle-shaped hydrates to meter-sized shotcrete tunnel shells: micromechanical upscaling of stiffness and strength of hydrating shotcrete, Acta Geotechnica 3 (4) (2008) 273–294.

[17] J. D. Eshelby, The determination of the elastic field of an ellipsoidal inclusion, and related problems, Proceedings of the Royal Society of London. Series A, Mathematical and Physical Sciences 241 (1226) (1957) 376–396.

[18] J. Melenk, I. Babuška, The partition of unity finite element method: Basic theory and applications, Computer Methods in Applied Mechanics and Engineering 139 (1–4) (1996) 289–314.

[19] I. Babuška, J. Melenk, The partition of unity method, International Journal for Numerical Methods in Engineering 40 (4) (1997) 727–758.

[20] G. Wells, Discontinuous modelling of strain localisation and failure, Ph.D. thesis, Delft University of Technology (2001).

[21] J. Teixeira de Freitas, Formulation of elastostatic hybrid-trefftz stress elements, Computer Methods in Applied Mechanics and Engineering 153 (1998) 127 – 151.

[22] Z. Bittnar, J. Šejnoha, Numerical methods in structural mechanics, American Society of Civil Engineers, 1996.

[23] J. Ju, Y. Ko, Micromechanical Elastoplastic Damage Modeling of Progressive Interfacial Arc Debonding for Fiber Reinforced Composites, International Journal of Damage Mechanics 17 (4) (2008) 307.

[24] J. D. Eshelby, The elastic field outside an ellipsoidal inclusion, Proceedings of the Royal Society of London. Series A, Mathematical and Physical Sciences (1959) 561–569.

[25] M. Rahman, On the Newtonian potentials of heterogeneous ellipsoids and elliptical discs, Proceedings: Mathematical, Physical and Engineering Sciences 457 (2013) (2001) 2227–2250.

Chapter 3

EFFICIENT EVALUATION OF MICROMECHANICAL FIELDS

To incorporate as many microstructural details as possible into the coarse scale finite element analysis we focused on the development of analytical or semi-analytical technique that would be computationally robust, capable of treating thousands of inclusions, and yet feasible to implement. As for the solution strategy, we adopted Eshelby's closed form solution to ellipsoidal inclusion in infinite media exposed to uniform eigenstrains. Regarding the implementation architecture, no hardware specific operations as e.g. GPU computing or binary operation based speed-ups were desirable besides conventional CPU and memory manipulation based coding, all this with respect to expected needs by the members of Computational Mechanics/Micromechanics community and foreseen open source license regulations of the developed library. As for the quest for the later mentioned feedback from Micromechanics community, it is worth noting, that, besides the developed algorithms to account for interactions among multiple inclusions, the library was also equipped by rather conventional homogenization strategies based on Mean Field Theories and, as we called it, the Direct Integration Method to asses the overall material properties from both, self-compatible/equilibriated local fields inside and outside the inclusions.

List of source journal papers and book chapters

Svoboda, L., Šulc, S., Janda, T., Vorel, J., and Novák, J. (2016). μMech micromechanics library. *Advances in Engineering Software*, 100:148–160.

μMECH Micromechanics Library

Ladislav Svoboda

Department of Mechanics, Faculty of Civil Engineering, Czech Technical University in Prague, Czech Republic

Stanislav Šulc

Department of Mechanics, Faculty of Civil Engineering, Czech Technical University in Prague, Czech Republic

Tomáš Janda

Department of Mechanics, Faculty of Civil Engineering, Czech Technical University in Prague, Czech Republic

Jan Vorel

Department of Mechanics, Faculty of Civil Engineering, Czech Technical University in Prague, Czech Republic

Jan Novák

Experimental Centre, Faculty of Civil Engineering, Czech Technical University in Prague, Czech Republic

Abstract

The paper presents the project of an open source C/C++ library of analytical solutions to micromechanical fields within media with ellipsoidal heterogeneities. The solutions are based on Eshelby's stress-free, in general polynomial, eigenstrains and equivalent inclusion method. To some extent, the interactions among inclusions in a non-dilute medium are taken into account by means of the self-compatibility algorithm. Moreover, the library is furnished with a powerful I/O interface and conventional homogenization tools. Advantages and limitations of the implemented strategies are addressed through comparisons with reference solutions by means of the Finite Element Method.

Keywords: C/C++ Library; Micromechanics; Eshelby solution; Polynomial eigenstrains; Multiple inclusion problem; Internal/External fields; Analytical homogenization schemes

1. Introduction

In this paper we present a C/C++ library of analytical solutions to classical micromechanical problems. In particular, the library μMECH provides users with routines evaluating

Email addresses: ladislav.svoboda@fsv.cvut.cz (Ladislav Svoboda), sulcstanda@seznam.cz (Stanislav Šulc), tomas.janda@fsv.cvut.cz (Tomáš Janda), jan.vorel@fsv.cvut.cz (Jan Vorel), novakja@fsv.cvut.cz (Jan Novák)

perturbations of local mechanical fields as strains, stresses, and displacements within a composite medium consisting of isolated ellipsoidal inhomogeneities embedded in an infinite matrix. The implemented, purely analytical solutions to both internal and external fields, i.e. inside and outside inclusion domains, are based on the influential J. D. Eshelby work [1] and are accomplished in two and three dimensions. The library deals with the heterogeneity problem by means of the equivalent inclusion method. It substitutes heterogeneities with appropriate inclusions subjected to transformation stress free eigenstrains consistent with applied far-field strains [1]. Both, constant and polynomial transformation eigenstrains are allowed. The latter is conveniently used to deal with the interacting multiple inclusions. In particular, the interactions among inclusions in a non-dilute media are taken into account by means of the so called self-compatibility algorithm, the fixed version of its ill-posed predecessor reported in [2]. In multiple inclusion problems, contact points among inclusions are allowed however penetrations are not.

μMECH was principally designed as a subroutine of Finite Element packages (FEM), justifying so a generic structure of the code and I/O interfaces. It is capable providing Generalized Finite Element environments with subscale enrichment functions to take into account perturbations in macro-field patterns due to microstructural details so as to avoid homogenization based upscaling [2]. Nonetheless, in order to comply with expectations of the micromechanics community, the library has been equipped with several homogenization routines based on direct numerical integration of local fields or conventional techniques as dilute approximation [1], Mori-Tanaka [3], and Self-consistent schemes [4].

The paper is structured as follows. In Section 2 we introduce the theoretical background of implemented techniques. In particular, we start with the definition of perturbation fields, give some basics to the Equivalent inclusion method, continue with a brief exposition to the aspects of Eshelby solution due to polynomial stress-free eigenstrains, self-compatibility algorithm and conclude with a summary on homogenization schemes. In Section 3 we comment on the architecture of μMECH, the structure of I/O interfaces, and license regulations. Numerical examples compared with reference solutions by means of FEM are discussed in Section 4. Final remarks concluding the exposition are given in Section 5.

2. Background

In what follows, we give a very brief introduction to theoretical background of implemented strategies in μMECH library. The entire Section 2 can be omitted by readers versed in classical micromechanics. As for the notation used throughout the section, we mostly use the compact tensorial form denoted by different font styles in bold depending on particular order of the tensors. However, where the exposition requires, we resort to standard tensorial notation with indices. For instance,

$$c_i = A_{ijkl} a_{kl} b_j = \mathbf{A} : \boldsymbol{a} \cdot \mathbf{b} = \mathbf{c}$$

Also, note that the superscripts over state variables do not stand for power indices. In the case of stiffness or concentration tensors, in general fourth order tensors, analogical indices are written as subscripts and superscripts are reserved e.g. for $\bullet^{-1}$ inverse operator. In addition, i, j, k, l, m, q are reserved for tensorial indices, r, s denote the inclusion enumerators, and p stands for the iteration loop increment.

2.1. Perturbation fields

Let assume an infinite isotropic homogeneous body with separated heterogeneities, Fig. 1. Moreover, consider the body be the subject to some macroscopic excitation, e.g. a remote strain induced by a combination of displacement and traction fields $\mathbf{u}(\mathbf{x}), \mathbf{t}(\mathbf{x})$ applied to the boundary $\partial\Omega_0$ at infinity. The stiffness of such a composite can be decomposed as [5, 6]

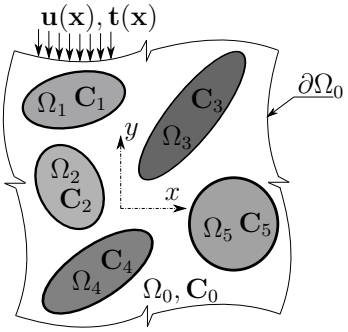

Figure 1: Infinite composite body with ellipsoidal inhomogeneities.

$$\mathbf{C}(\mathbf{x}) = \mathbf{C}_0 + \overline{\mathbf{C}}(\mathbf{x}) \tag{1}$$

where $\mathbf{C}_0$ represents the fourth order tensor of elastic constants of the matrix Ω_0 and $\overline{\mathbf{C}}(\mathbf{x}) = \mathbf{C}(\mathbf{x}) - \mathbf{C}_0$ is its piecewise constant complement to $\mathbf{C}(\mathbf{x})$ due to the presence of $1, \ldots, n$ heterogeneities. Note, $\overline{\mathbf{C}}(\mathbf{x})$ is nonzero only for $\mathbf{x} \in \bigcup_{r=1}^{n} \Omega_r$. As a result of applied loads, the heterogeneous body experiences local fields that can be decomposed by analogy to Eq. (1) as

$$\mathbf{u}(\mathbf{x}) = \mathbf{u}^0(\mathbf{x}) + \overline{\mathbf{u}}(\mathbf{x}), \quad \boldsymbol{\varepsilon}(\mathbf{x}) = \boldsymbol{\varepsilon}^0 + \overline{\boldsymbol{\varepsilon}}(\mathbf{x}), \quad \boldsymbol{\sigma}(\mathbf{x}) = \boldsymbol{\sigma}^0 + \overline{\boldsymbol{\sigma}}(\mathbf{x}) \tag{2}$$

Here, the superscript $\bullet^0$ indicates the homogeneous (macroscopic) component of the state variables in the absence of heterogeneities and $\overline{\bullet}$ stands for its perturbation (microscopic) counterpart induced by their presence. Determination of the perturbation fields is based on the equivalent inclusion method as proposed by Eshelby in [1]. Here, we first limit the exposition to a single ellipsoidal heterogeneity embedded in a homogeneous matrix undergoing a uniform remote strain excitation and then explore some possibilities to take into account interactions among multiple heterogeneities.

2.2. Equivalent inclusion method for single heterogeneity problem

When seeking for local fields by means of the equivalent inclusion method, we replace the heterogeneity problem, Fig. 2a, by an equivalent inclusion problem consisting of the homogeneous matrix exposed to a suitable stress-free eigenstrain $\boldsymbol{\varepsilon}^\tau(\mathbf{x})$ which vanishes everywhere except for $\mathbf{x} \in \Omega_1$, Fig. 2c, supplement to external loads applied at infinity, Fig. 2b, see [1] for further details. The solution of the inclusion problem then primarily requires the determination of the transformation eigenstrain $\boldsymbol{\varepsilon}^\tau(\mathbf{x})$ that induces identical perturbation to the homogeneous fields as it would occur due to the original inhomogeneity. As there are no other inclusions surrounding that of our concern, $\boldsymbol{\varepsilon}^\tau(\mathbf{x})$ remains constant in Ω_1, that is we can write $\boldsymbol{\varepsilon}^\tau(\mathbf{x} \in \Omega_1) = \boldsymbol{\varepsilon}^\tau$. According to Hook's law and decompositions in Eq. $(2)^{2,3}$, local stresses rendered by the inhomogeneity problem, Fig. 2a, read as

$$\boldsymbol{\sigma}(\mathbf{x}) = \boldsymbol{\sigma}^0 + \overline{\boldsymbol{\sigma}}(\mathbf{x}) = \mathbf{C}(\mathbf{x}) : [\boldsymbol{\varepsilon}^0 + \overline{\boldsymbol{\varepsilon}}(\mathbf{x})] \tag{3}$$

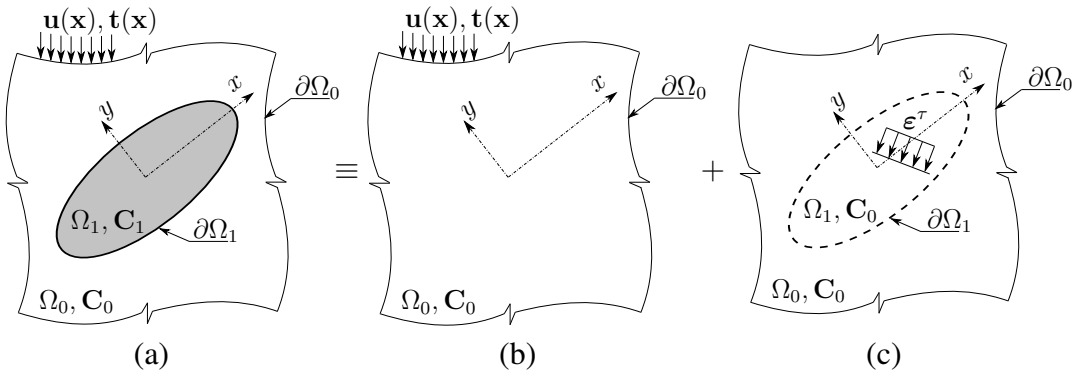

Figure 2: Equivalent inclusion method, a) inhomogeneity problem, b) infinite homogeneous body with allied loads, c) homogeneous inclusion problem.

For the equivalent problem holds

$$\boldsymbol{\sigma}(\mathbf{x}) = \mathbf{C}_0 : [\boldsymbol{\varepsilon}^0 + \overline{\boldsymbol{\varepsilon}}(\mathbf{x}) - \boldsymbol{\varepsilon}^\tau(\mathbf{x})] \tag{4}$$

Given the fact that $\boldsymbol{\sigma}^0 = \mathbf{C}_0 : \boldsymbol{\varepsilon}^0$, it yields from Eq. (2)[3] and Eq. (4)

$$\overline{\boldsymbol{\sigma}}(\mathbf{x}) = \mathbf{C}_0 : [\overline{\boldsymbol{\varepsilon}}(\mathbf{x}) - \boldsymbol{\varepsilon}^\tau(\mathbf{x})] \tag{5}$$

Now, equating the rhs's of Eqs. (3–4),

$$\mathbf{C}(\mathbf{x}) : [\boldsymbol{\varepsilon}^0 + \overline{\boldsymbol{\varepsilon}}(\mathbf{x})] = \mathbf{C}_0 : [\boldsymbol{\varepsilon}^0 + \overline{\boldsymbol{\varepsilon}}(\mathbf{x}) - \boldsymbol{\varepsilon}^\tau(\mathbf{x})] \tag{6}$$

and taking into account the following fundamental solution for $\overline{\boldsymbol{\varepsilon}}(\mathbf{x})$

$$\overline{\boldsymbol{\varepsilon}}(\mathbf{x}) = \mathbf{S}(\mathbf{x}) : \boldsymbol{\varepsilon}^\tau \tag{7}$$

where $\mathbf{S}(\mathbf{x})$ denotes the Eshelby tensor evaluated at an arbitrary point $\mathbf{x}$, results

$$[\mathbf{C}(\mathbf{x}) - \mathbf{C}_0] \; : \boldsymbol{\varepsilon}^0 = [\mathbf{C}_0 : \mathbf{S}(\mathbf{x}) - \mathbf{C}(\mathbf{x}) : \mathbf{S}(\mathbf{x}) - \mathbf{C}_0] \; : \boldsymbol{\varepsilon}^\tau \tag{8}$$

The definition of $\mathbf{S}(\mathbf{x})$ tensor is as in Eq. (14) and Eq. (16)[1] while the detailed derivation can be found e.g. in [1, 5]. Finally, Eq. (8) gives rise the sought stress free transformation eigenstrain $\boldsymbol{\varepsilon}^\tau$ in the form

$$\boldsymbol{\varepsilon}^\tau = \mathbf{Q} : \boldsymbol{\varepsilon}^0 \tag{9}$$

where tensor $\mathbf{Q}$ reads as

$$\mathbf{Q} = -\left[\,\overline{\mathbf{C}}_1 : \mathbf{S}(\mathbf{0}) + \mathbf{C}_0\right]^{-1} \; : \overline{\mathbf{C}}_1 \tag{10}$$

Once the transformation eigenstrain has been determined, Eq. (9), the stress perturbation can be computed from Eq. (5) and displacement perturbations as

$$\overline{\mathbf{u}}(\mathbf{x}) = \boldsymbol{\mathcal{L}}(\mathbf{x}) : \boldsymbol{\varepsilon}^\tau = \boldsymbol{\mathcal{L}}(\mathbf{x}) : \mathbf{Q} : \boldsymbol{\varepsilon}^0 \tag{11}$$

where the operator $\boldsymbol{\mathcal{L}}(\mathbf{x})$ is the third order Eshelby tensor-like operator mapping $\boldsymbol{\varepsilon}^\tau \mapsto \overline{\mathbf{u}}(\mathbf{x})$ whose detailed derivation can be found in [2].

2.3. Single inclusion problem for polynomial eigenstrains

The solution to a single inclusion in the infinite matrix loaded by a constant eigenstrain stated formally in equation Eq. (7) was generalized by Sendeckyj (1967) and Moschovidis (1975) for eigenstrains prescribed in a general polynomial form [5, and references therein]. For a simpler exposition, here we summarize only the solution to the single inclusion under linear eigenstrain excitation, though the solution to the problem with quadratic eigenstrains is also implemented to some extent in current version of μMECH. Going back to index based Einstein summation convention, the prescribed linear eigenstrain field that is nonzero only for $\mathbf{x} \in \Omega_1$, is defined as

$$\varepsilon^{\tau}_{ij}(\mathbf{x}) = \varepsilon^{\tau}_{ij} + \varepsilon^{\tau}_{ijk} x_k \tag{12}$$

where ε^{τ}_{ij} is the constant part of the imposed eigenstrain identical to that from the previous paragraph, and ε^{τ}_{ijk} contains its gradient complements in k-th coordinate direction. By analogy to Eq. (7), it holds

$$\overline{\varepsilon}_{ij}(\mathbf{x}) = S_{ijkl}(\mathbf{x})\varepsilon^{\tau}_{kl} + S_{ijklm}(\mathbf{x})\varepsilon^{\tau}_{klm} \tag{13}$$

The solution thus reduces to seeking for components of tensors S_{ijkl} and S_{ijklm}, which depend only on the proportions of the semi-axes of Ω_1 and matrix Poisson's ratio ν_0. In particular, for exterior points, i.e. $\mathbf{x} \notin \Omega_1$, the following definitions hold [5]

$$\begin{aligned} S_{ijkl}(\mathbf{x}) = [&\psi_{,klij} - 2\nu_0\delta_{kl}\phi_{,ij} \\ &- (1-\nu_0)(\phi_{,kj}\delta_{il} + \phi_{,ki}\delta_{jl} + \phi_{,lj}\delta_{ik} + \phi_{,li}\delta_{jk})]/[8\pi(1-\nu_0)] \end{aligned} \tag{14}$$

$$\begin{aligned} S_{ijklm}(\mathbf{x}) = [&\psi_{m,klij} - 2\nu_0\delta_{kl}\phi_{m,ij} \\ &- (1-\nu_0)(\phi_{m,kj}\delta_{il} + \phi_{m,ki}\delta_{jl} + \phi_{m,lj}\delta_{ik} + \phi_{m,li}\delta_{jk})]/[8\pi(1-\nu_0)] \end{aligned} \tag{15}$$

On the other hand, for all points $\mathbf{x}$ inside Ω_1, the above tensors read as

$$S_{ijkl}(\mathbf{x}) = S_{ijkl}(\mathbf{0}), \quad S_{ijklm}(\mathbf{x}) = S_{ijklm,q}(\mathbf{0})x_q \tag{16}$$

Symbol δ_{ij} denotes the Kronecker delta and $\bullet_{,i}$ stands for the first derivative in i-th direction. The potentials ϕ and ϕ_i and the first derivative of potential ψ and ψ_i are defined as

$$\begin{aligned} \phi(\mathbf{x}) = V(\mathbf{x}), \quad \phi_i(\mathbf{x}) = a_i^2 x_i V_i(\mathbf{x}), \quad \psi_{,i}(\mathbf{x}) &= x_i[V(\mathbf{x}) - a_i^2 V_i(\mathbf{x})] \\ \psi_{i,j}(\mathbf{x}) = -\frac{1}{4}\delta_{ij}a_i^2\{V(\mathbf{x}) - x_k^2 V_k(\mathbf{x}) - a_i^2[V_i(\mathbf{x}) - x_k^2 V_{ki}(\mathbf{x})]\} \\ + a_i^2 x_i x_j[V_j(\mathbf{x}) - a_i^2 V_{ji}(\mathbf{x})] \end{aligned} \tag{17}$$

with a_i being ellipsoidal semi-axe lengths sorted in descending order and index k being the summation index. Elliptic integrals V, V_i and V_{ij}, respectively, read

$$V(\mathbf{x}) = \frac{I(\lambda) - x_k^2 I_k(\lambda)}{2}, \quad V_i(\mathbf{x}) = \frac{I_i(\lambda) - x_k^2 I_{ik}(\lambda)}{2}, \quad V_{ij}(\mathbf{x}) = \frac{I_{ij}(\lambda) - x_k^2 I_{ijk}(\lambda)}{2} \tag{18}$$

where I, I_i, I_{ij} and I_{ijk} are λ-variable dependent elliptic integrals. The value of λ for a given point $\mathbf{x} \in \Omega_1$ is the largest positive root of the cubic equation

$$\frac{x_1^2}{a_1^2 + \lambda} + \frac{x_2^2}{a_2^2 + \lambda} + \frac{x_3^2}{a_3^2 + \lambda} = 1 \tag{19}$$

and zero otherwise. The elliptic integrals I and I_i are expressed as

$$\begin{aligned}
I(\lambda) &= b(a_1^2-a_3^2)^{-\frac{1}{2}}F(\theta,c),\\
I_1(\lambda) &= b(a_1^2-a_2^2)^{-1}(a_1^2-a_3^2)^{-\frac{1}{2}}[F(\theta,c)-E(\theta,c)],\\
I_2(\lambda) &= b[(a_1^2-a_2^2)^{-1}(a_2^2-a_3^2)^{-1}(a_1^2-a_3^2)^{\frac{1}{2}}E(\theta,c)-(a_1^2-a_2^2)^{-1}(a_1^2-a_3^2)^{-\frac{1}{2}}F(\theta,c)\\
&\quad -(a_2^2-a_3^2)^{-1}(a_3^2+\lambda)^{\frac{1}{2}}(a_1^2+\lambda)^{-\frac{1}{2}}(a_2^2+\lambda)^{-\frac{1}{2}}],\\
I_3(\lambda) &= b(a_2^2-a_3^2)^{-1}(a_1^2-a_3^2)^{-\frac{1}{2}}[(a_1^2-a_3^2)^{\frac{1}{2}}(a_2^2+\lambda)^{\frac{1}{2}}(a_1^2+\lambda)^{-\frac{1}{2}}(a_3^2+\lambda)^{-\frac{1}{2}}]
\end{aligned} \tag{20}$$

with $b = 4\pi a_1 a_2 a_3$, $\theta = \arcsin\sqrt{1-a_3^2/a_1^2}$, and $c = \sqrt{(a_1^2-a_2^2)/(a_1^2-a_3^2)}$. Functions F and E are the incomplete Legendre elliptic integrals defined as

$$F(\theta,c) = \int_0^\theta \frac{\mathrm{d}w}{\sqrt{1-c^2\sin^2 w}}, \quad E(\theta,c) = \int_0^\theta \sqrt{1-c^2\sin^2 w}\;\mathrm{d}w \tag{21}$$

In addition, higher order integrals I_{ij} and I_{ijk} are expressed by means of those of the lower orders and by substituting $\alpha = (a_i^2 - a_j^2)$ as follows

$$\begin{aligned}
I_{ij}(\lambda) &= [I_j(\lambda) - I_i(\lambda)]/\alpha, \quad I_{iij}(\lambda) = [I_{ij}(\lambda) - I_{ii}(\lambda)]/\alpha \quad \forall\, i \neq j,\\
I_{ii}(\lambda) &= \frac{1}{3}[\frac{b}{(a_i^2+\lambda)^2\Delta(\lambda)} - I_{ij}(\lambda) - I_{ik}(\lambda)], \quad I_{ijk}(\lambda) = [I_{jk}(\lambda) - I_{ik}(\lambda)]/\alpha,\\
I_{iii}(\lambda) &= \frac{1}{5}[\frac{b}{(a_i^2+\lambda)^2\Delta(\lambda)} - I_{iij}(\lambda) - I_{iik}(\lambda)] \quad \forall\, i \neq j \neq k \neq i
\end{aligned} \tag{22}$$

Finally, $\Delta(\lambda)$ reads as

$$\Delta(\lambda) = \sqrt{(a_1^2+\lambda)(a_2^2+\lambda)(a_3^2+\lambda)} \tag{23}$$

2.4. Multiple-inclusion problem

In the case of an infinite matrix with multiple inclusions, the perturbation fields within Ω_r, Fig. 1, are no longer uniformly distributed as a result of their mutual interactions. In μMECH, we account for the interactions only approximately by assuming the eigenfields within r-th inclusion be still constant, however, influenced by local changes of state variables due to the remaining inclusions, namely those nearby Ω_r. In particular, we control the "compatibility" of the perturbation strain field inside each inclusion calculated by means of Eq. (7). The key ingredient of these formulas, $\boldsymbol{\varepsilon}_r^0$, mapped to $\boldsymbol{\varepsilon}_r^\tau$ through $\mathbf{Q}_r$, is recursively increased by perturbation strains $\overline{\boldsymbol{\varepsilon}}_{s\to r}$ arising from the presence of $s = 1,\ldots,n$ inclusions. That is why, we have different $\boldsymbol{\varepsilon}_r^0$ for each of $1,\ldots,r,\ldots,n$ inclusions. Individual contributions $\overline{\boldsymbol{\varepsilon}}_{s\to r}$ to $\boldsymbol{\varepsilon}_r^{0,\mathrm{tot}}$ are measured in the center of Ω_r, Fig. 3a. Thus, $\boldsymbol{\varepsilon}_r^{0,\mathrm{tot}}$ in the p-th iteration loop of the self-compatibility procedure reads as

$${}^p\boldsymbol{\varepsilon}_r^{0,\mathrm{tot}} \overset{\mathrm{def}}{=} \boldsymbol{\varepsilon}^0 + \sum_{s\backslash r}^{n} {}^p\overline{\boldsymbol{\varepsilon}}_{s\to r} \tag{24}$$

where the contributions ${}^p\overline{\boldsymbol{\varepsilon}}_{s\to r}$ are evaluated from the previous remote field ${}^{p-1}\boldsymbol{\varepsilon}_r^{0,\mathrm{tot}}$; the $s\backslash r$ operation excludes inclusion r from the set of n inclusions. The initial remote strain $\boldsymbol{\varepsilon}^0$

	Self Compatibility Algorithm $(\boldsymbol{\varepsilon}_r^0, \boldsymbol{\varepsilon}_r^\tau, \mathbf{Q}_r, \mathbf{S}_r, n)$
1	**Do**
2	**For** $(r \leq n)$
3	$\boldsymbol{\varepsilon}_r^{\tau,\mathrm{prev}} = \boldsymbol{\varepsilon}_r^\tau$
4	$\boldsymbol{\varepsilon}_r^{0,\mathrm{tot}} = \boldsymbol{\varepsilon}^0 + \sum_{s\setminus r}^n \overline{\boldsymbol{\varepsilon}}_{s\to r}$
5	$\boldsymbol{\varepsilon}_r^\tau = \mathbf{B}_r : \boldsymbol{\varepsilon}_r^{0,\mathrm{tot}}$
6	$\Delta\boldsymbol{\varepsilon}_r^\tau = \boldsymbol{\varepsilon}_r^\tau - \boldsymbol{\varepsilon}_r^{\tau,\mathrm{prev}}$
7	**EndFor**
8	**While** $\left(\sum_r^n \|\Delta\boldsymbol{\varepsilon}_r^\tau\| > \eta\right)$

Table 1: *Self-compatibility* algorithm. In principle, within each iteration loop we consider the effect of s-th inclusion on inclusion r as an additional external load entering the solution to its equivalent stress-free eigenstrain $\boldsymbol{\varepsilon}_r^\tau$. This means, in each iteration, we recalculate $\boldsymbol{\varepsilon}_r^{0,tot}$ for every single inclusion as the sum of the prescribed homogeneous strain $\boldsymbol{\varepsilon}^0$ and its perturbations due to remaining inclusions $\overline{\boldsymbol{\varepsilon}}_{s\to r}$ evaluated in the centroid of inclusion r, line 4. Next, $\boldsymbol{\varepsilon}_r^\tau$ is updated, line 5. The algorithm continues until an acceptable tolerance η between the Euclidean norms of the two consecutive stress-free eigenstrains ε_r^τ is achieved, line 8.

is imposed to the matrix surrounding all inclusions at the beginning of the procedure, i.e. ${}^1\boldsymbol{\varepsilon}_r^{0,\mathrm{tot}} = \boldsymbol{\varepsilon}^0$. The line-by-line definition of the iterative algorithm based on Eq. (24) follows in Tab. 1. At its convergence, the stress and displacement perturbations corresponding to compatible transformation eigenstrains are recalculated according to Eq. (5) and Eq. (11). It is worthwhile to note that the algorithm does not depend on a particular sequence of inclusions, as follows from the elastic reciprocity theorem [7, and references therein]. The iterative procedure has been chosen since a closed form solution for the multiple inclusion problem does not exist and a numerical one would be prohibitively expensive, see e.g. [7]. The computational complexity of the so called *full* version of the algorithm is $O(n^2)$. However, this can be further reduced by taking into account only inclusions that have a non-negligible impact on the r-th inclusion of interest, usually those placed very nearby Ω_r or excessively large inclusions in the case of somehow disparate polydisperse. This algorithm is called *optimized* in μMECH. Its complexity reduces to $O(\xi n)$, where $\xi = \frac{1}{r}\sum_r \xi_r$ is the arithmetic average of the number of inclusions whose cut outs limited by radii[1] ρ_s centered in $\mathbf{x}_s$ embrace the r-th inclusion, Fig. 3b. Note, for $n \to \infty$ the complexity of *optimized* algorithm is $O(n)$ as $\xi = \mathrm{const} \ll n$.

2.5. Approximation to perturbation strain concentrations

When dealing with a dilute distribution of inclusions, constant strain and stress fields are assumed within Ω_r and no question on concentrations comes in play. However, the goal of μMECH is to proceed a few steps beyond, namely to non-dilute dispersions. The concentrations arising from mutual inclusion interactions are approximated by the following procedure, which stems from the approximate solution to the sought non-constant transformation eigenstrain $\boldsymbol{\varepsilon}_r^\tau(\mathbf{x})$ suitable for the decomposition in Eq. (12) or similar one of a higher degree.

Consider point a $\mathbf{x}$ inside the inclusion domain Ω_r, where we calculate the stress free

[1] A usual choice is 2.5 multiple of the longest semi-axis a_1.

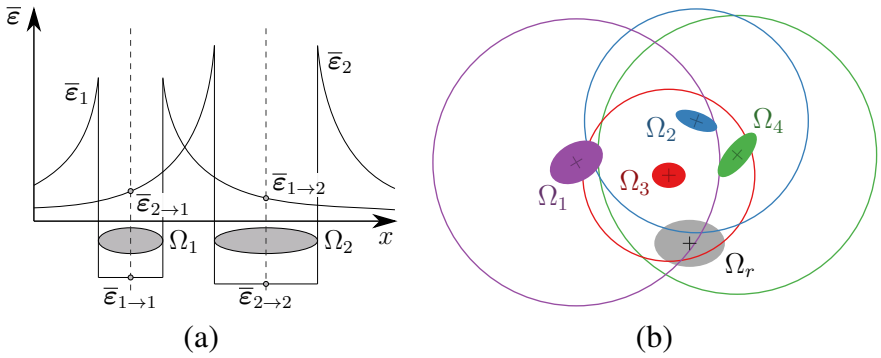

Figure 3: Illustration of self-compatibility algorithm, a) principle for double inclusion problem, b) inclusions having non-negligible impact on r-th inclusion $\xi_r = \|\Omega_1, \Omega_3, \Omega_4\| = 3$.

transformation eigenstrain as

$$\boldsymbol{\varepsilon}_r^\tau(\mathbf{x}) \approx \mathbf{Q}_r : \left[\boldsymbol{\varepsilon}^0 + \sum_{s\setminus r}^{n} \overline{\boldsymbol{\varepsilon}}_{s\to r}(\mathbf{x})\right] \tag{25}$$

Consequently we sample $\boldsymbol{\varepsilon}_r^\tau(\mathbf{x})$ in as many points $\mathbf{x}$ as necessary for a polynomial of chosen degree, three in the case case of Eq. (12). Finally, the solution to perturbation fields for points $\mathbf{x}$ in each domain Ω_r are obtained following the exposition given in Paragraph 2.3. For the points within the matrix, i.e. $\mathbf{x}$ outside the union $\bigcup_{r=1}^{n} \Omega_r$, the solutions are obtained by the sum of individual contributions attributed to each of $1, \ldots, n$ inclusions.

An alternative, and surprisingly well working, approach such that it does not call for the implementation of polynomial eigenstrain problem is, that the solutions to perturbation strains in the internal points are calculated by means of the basic Eshelby formula given in Eq. (7), as

$$\overline{\boldsymbol{\varepsilon}}_r(\mathbf{x}) \approx \mathbf{S}_r : \boldsymbol{\varepsilon}_r^\tau(\mathbf{x}) + \sum_{s\setminus r}^{n} \overline{\boldsymbol{\varepsilon}}_{s\to r}(\mathbf{x}) \tag{26}$$

where $\boldsymbol{\varepsilon}_r^\tau(\mathbf{x})$ is that provided by Eq. (25). By analogy to the latter approach, the solution in external points is obtained by adding up contributions from all inclusions.

Finally, it is worthwhile to note that the computational complexity can be controlled by the number of internal points chosen to approximate $\boldsymbol{\varepsilon}_r^\tau(\mathbf{x})$ by either of the approaches above. In addition, substantial savings can be made by choosing *optimized* mode running on the same principles as in the case of the self-compatibility algorithm.

2.6. Homogenization

Assuming non-elastic phenomena be entirely attributed to the microstructure evolution dynamics, the constitutive behavior of an arbitrary point $\mathbf{x}$ at an instant is governed by the following pair of equations [8],

$$\boldsymbol{\sigma}_r(\mathbf{x}) = \mathbf{C}_r : \boldsymbol{\varepsilon}_r(\mathbf{x}), \quad \boldsymbol{\varepsilon}_r(\mathbf{x}) = \mathbf{C}_r^{-1} : \boldsymbol{\sigma}_r(\mathbf{x}) \quad \text{for} \quad \mathbf{x} \in \Omega_r \tag{27}$$

where $r = 0, \ldots, n$. According to Hill's lemma [9, 8], the averages of the above local quantities $\boldsymbol{\sigma}(\mathbf{x})$ and $\boldsymbol{\varepsilon}(\mathbf{x})$ are coupled with their macroscopic conjugates $\boldsymbol{\Sigma}, \boldsymbol{E}$ as

$$\langle \boldsymbol{\sigma}(\mathbf{x}) \rangle = \langle \mathbf{C}(\mathbf{x}) \colon \boldsymbol{\varepsilon}(\mathbf{x}) \rangle = \sum_r^n c_r \mathbf{C}_r \colon \langle \boldsymbol{\varepsilon}_r(\mathbf{x}) \rangle = \sum_r^n c_r \mathbf{C}_r \colon \boldsymbol{\varepsilon}_r = \mathbb{C} \colon \boldsymbol{E},$$
$$\langle \boldsymbol{\varepsilon}(\mathbf{x}) \rangle = \langle \mathbf{C}^{-1}(\mathbf{x}) \colon \boldsymbol{\sigma}(\mathbf{x}) \rangle = \sum_r^n c_r \mathbf{C}_r^{-1} \colon \langle \boldsymbol{\sigma}_r(\mathbf{x}) \rangle = \sum_r^n c_r \mathbf{C}_r^{-1} \colon \boldsymbol{\sigma}_r = \mathbb{C}^{-1} \colon \boldsymbol{\Sigma} \tag{28}$$

It is evident, that the effective elastic stiffness and compliance tensors depend on the elastic properties of each phase $\mathbf{C}_r$ and volume fractions c_r. In addition, they depend on mutual interactions given by the intrinsic geometrical arrangement of the phases and the compatibility or equilibrium requirements, encoded in concentration factors $\mathbf{A}_r, \mathbf{B}_r$ for which it holds [10, 1]

$$\boldsymbol{\varepsilon}_r = \mathbf{A}_r : \boldsymbol{E}, \; \boldsymbol{\sigma}_r = \mathbf{B}_r : \boldsymbol{\Sigma} \tag{29}$$

Plugging the latter definitions in last two terms of Eq. (28) gives

$$\mathbb{C} = \sum_r^n c_r \mathbf{C}_r : \mathbf{A}_r, \quad \mathbb{C}^{-1} = \sum_r^n c_r \mathbf{C}_r^{-1} : \mathbf{B}_r \tag{30}$$

Now, identifying by $r = 0$ a matrix phase in which the remaining heterogeneities are fully embedded, and taking into account the fact that $c_0 \mathbf{A}_0 = \mathbb{I} - \sum_{r=1}^n c_r \mathbf{A}_r$, $c_0 \mathbf{B}_0 = \mathbb{I} - \sum_{r=1}^n c_r \mathbf{B}_r$, where $\mathbb{I}$ is the fourth order identity tensor, and considering $c_0 = 1 - \sum_{r=1}^n c_r$, yields

$$\mathbb{C} = \mathbf{C}_0 + \sum_r^n c_r \overline{\mathbf{C}}_r : \mathbf{A}_r, \quad \mathbb{C}^{-1} = \mathbf{C}_0^{-1} + \sum_r^n c_r \overline{\mathbf{C}}_r^{-1} : \mathbf{B}_r \tag{31}$$

where, according to Eq. (1), it holds

$$\overline{\mathbf{C}}_r = \mathbf{C}_r - \mathbf{C}_0 \tag{32}$$

From now on, the central question is how to evaluate the concentration factors $\mathbf{A}_r$ and $\mathbf{B}_r$ for a medium with multiple inclusions.

2.6.1. Homogenization by direct integration of approximate local fields

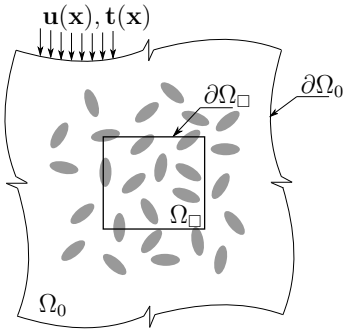

Figure 4: Two-dimensional illustration of DIM subdomain $\Omega_\square$ in cluster of inclusions embedded in infinite matrix Ω_0.

The Direct Integration Method (DIM) stems of the numerical integration of local stresses and strains in the subregion $\Omega_\square$, Fig. 4, of a larger cluster of inclusions embedded in the matrix and arising from the successive load steps by a single unitary component of ε^0_{ij} while the other vanish, see e.g. [4]. Thus, the set of nine ij-th components[2] of the fourth order tensor of effective stiffness moduli is rendered as

$$\mathbb{C} = \mathbb{E}^{-1} : \mathbb{\Sigma} \tag{33}$$

where

$$\mathbb{\Sigma}_{ijkl} \overset{\varepsilon^0_{ij}=1}{=} \langle \sigma_{kl} \rangle = \frac{1}{|\Omega_\square|} \int_{\Omega_\square} \sigma_{kl} \, \mathrm{d}\Omega, \quad \mathbb{E}_{ijkl} \overset{\varepsilon^0_{ij}=1}{=} \langle \varepsilon_{kl} \rangle = \frac{1}{|\Omega_\square|} \int_{\Omega_\square} \varepsilon_{kl} \, \mathrm{d}\Omega \tag{34}$$

This homogenization procedure assumes the subregion boundary $\partial\Omega_\square$ be sufficiently far from the boundary of the cluster of all inclusions entering the analysis in order to guarantee vanishing boundary effects. In addition, it is considered that the subregion's volume and geometry is representative to the solved microstructure. In other words, it should form its Representative Volume Element (RVE) [9]. It is also worthwhile to note that the shape of $\Omega_\square$ is completely arbitrary. It does not even need to form a continuous domain.

2.6.2. Dilute approximation

Suppose the dispersion of inclusions distributed in the infinite matrix is low or, say, dilute. Under such conditions, inclusions do not interact, and as a consequence, the macroscopic strain $\boldsymbol{E}$ from Eq. (28) and Eq. (29) can be imagined as equal to the remote strain $\boldsymbol{\varepsilon}^0$ from the exposition introduced in Paragraph 2.1. So that, expanding Eq. (2)[2] by means of Eq. (7) gives the local strains inside r-th inclusion in the form

$$\boldsymbol{\varepsilon}_r = \boldsymbol{\varepsilon}^0 + \mathbf{S}_r : \boldsymbol{\varepsilon}^\tau_r \overset{\text{Eq. (9)}}{=} \boldsymbol{\varepsilon}^0 + \mathbf{S}_r : \mathbf{Q}_r : \boldsymbol{\varepsilon}^0 = \mathbf{A}^{\mathrm{dil}}_r : \boldsymbol{\varepsilon}^0 \tag{35}$$

where

$$\mathbf{A}^{\mathrm{dil}}_r = (\mathbb{I} + \mathbf{S}_r : \mathbf{Q}_r) \tag{36}$$

By analogy, considering $\mathbf{\Sigma}$ to approach $\boldsymbol{\sigma}^0$ and taking into account Eq. (4) and Eq. (29)[2] gives

$$\mathbf{B}^{\mathrm{dil}}_r = [\mathbb{I} + \mathbf{Q}_r : (\mathbf{S}_r - \mathbb{I})] \tag{37}$$

2.6.3. Mori-Tanaka approximation

The Mori-Tanaka approximation to concentration factors falls into the class of the so called mean-field theory methods. Namely, the inclusion interactions are accounted for by making use of the assumption that each inclusion is embedded separately in a large volume of a matrix which is subjected to a uniform remote stress or strain equal to as yet unknown averages [3]. In particular, the aim is to arrive at concentration factors $\mathbf{A}^{\mathrm{MT}}_r$, $\mathbf{B}^{\mathrm{MT}}_r$ as functions of the polarization tensors which are equal to dilute concentration factors from Eq. (36) and Eq. (37). Thus, the strain and stress in the r-th inclusion, respectively, reads as

$$\boldsymbol{\varepsilon}_r = \mathbf{A}^{\mathrm{dil}}_r \boldsymbol{\varepsilon}_0, \quad \boldsymbol{\sigma}_r = \mathbf{B}^{\mathrm{dil}}_r \boldsymbol{\sigma}_0 \tag{38}$$

[2] one column or row in Voight-Mandel notation

From the strains averaged over the entire spectrum of n inclusions plus that in the matrix phase, one can deduce, see e.g. [11],

$$\langle\boldsymbol{\varepsilon}\rangle = \left(c_0\mathbb{I} + \sum_{r=1}^{n} c_r\mathbf{A}_r^{\mathrm{dil}}\right)\boldsymbol{\varepsilon}_0 \Rightarrow \boldsymbol{\varepsilon}_0 = \left(c_0\mathbb{I} + \sum_{r=1}^{n} c_r\mathbf{A}_r^{\mathrm{dil}}\right)^{-1}\langle\boldsymbol{\varepsilon}\rangle \tag{39}$$

Introducing Eq. $(39)^2$ into Eq. $(38)^1$, we arrive at

$$\boldsymbol{\varepsilon}_r = \mathbf{A}_r^{\mathrm{dil}}\left(c_0\mathbb{I} + \sum_{r=1}^{n} c_r\mathbf{A}_r^{\mathrm{dil}}\right)^{-1}\langle\boldsymbol{\varepsilon}\rangle = \mathbf{A}_r^{\mathrm{MT}}\langle\boldsymbol{\varepsilon}\rangle = \mathbf{A}_r^{\mathrm{MT}}\boldsymbol{E} \tag{40}$$

such that entering back to Eq. $(28)^1$ gives effective stiffness moduli stored in $\mathbb{C}$. By analogy, starting the above analysis from Eq. $(38)^2$ gives the Mori-Tanaka approximation to stress concentration factor $\mathbf{B}_r^{\mathrm{MT}}$ in the form

$$\mathbf{B}_r^{\mathrm{MT}} = \mathbf{B}_r^{\mathrm{dil}}\left(c_0\mathbb{I} + \sum_{r=1}^{n} c_r\mathbf{B}_r^{\mathrm{dil}}\right)^{-1} \tag{41}$$

yielding effective compliance moduli by making use of Eq. $(28)^2$.

2.6.4. Self-Consistent approximation

Interactions among $r = 1, \ldots, n$ phases are accounted for by assuming that each phase is an inclusion placed in the homogeneous medium of yet unknown overall properties of the aggregate of $n\backslash r$ remaining inclusions. It thus falls into the class of the so called effective medium methods. The Self-Consistent method is known to overestimate the interaction influence [12], which makes it specifically tailored for particulate media where a matrix phase, usually formed by fine particles, can not be clearly distinguished. Contrary to the approximations presented above, the Self-Consistent method results in implicit formulas [13]. Starting from the dilute approximation one can write

$$\mathbf{A}_r^{\mathrm{SC}} = (\mathbb{I} + \mathbf{S}_r^{\mathrm{SC}} : \mathbf{Q}_r^{\mathrm{SC}}), \quad \mathbf{B}_r^{\mathrm{SC}} = [\mathbb{I} + \mathbf{Q}_r^{\mathrm{SC}} : (\mathbf{S}_r^{\mathrm{SC}} - \mathbb{I})] \tag{42}$$

where the superscript $\bullet^{\mathrm{SC}}$ denotes explicit dependence of a quantity on material moduli coming from the Self-consistent approximation. In other words, stiffness moduli entering the formulas for $\mathbf{Q}$, Eq. (10) and $\mathbf{S}$, see e.g. [5], are functions of $\mathbf{C}^{\mathrm{CS}}$ by substitution for $\mathbf{C}^0$, notice especially Eqs. (1) and (10).

Note, that the so called Cai-Horii approximation is obtained after the first iteration of the Self-consistent scheme [14] where the quantities on the right-hand sides of both terms in Eq. (42) are functions of the properties coming out the dilute approximations in Eqs. (36–37).

2.6.5. Differential scheme

The differential scheme also falls into the family of effective medium methods. Contrary to the Self-Consistent approximation, this method builds the effective medium by incrementally adding inclusions to the matrix of effective properties obtained in previous steps. For instance, in the first step, μMECH adds the first inclusion to the virgin matrix of stiffness $\mathbf{C}_0$. In the next step, it adds another inclusion from the list to the matrix of effective properties obtained from the dilute approximation to the first step problem, and so on. It is clear that the previously homogenized matrix is not isotropic anymore unless the first inclusion was of the circular or spherical shape. That is why, μMECH performs numerical integration of elliptic potentials entering Eq. (14) for the Eshelby tensor $\mathbf{S}$, see e.g. [15, 16] for more details.

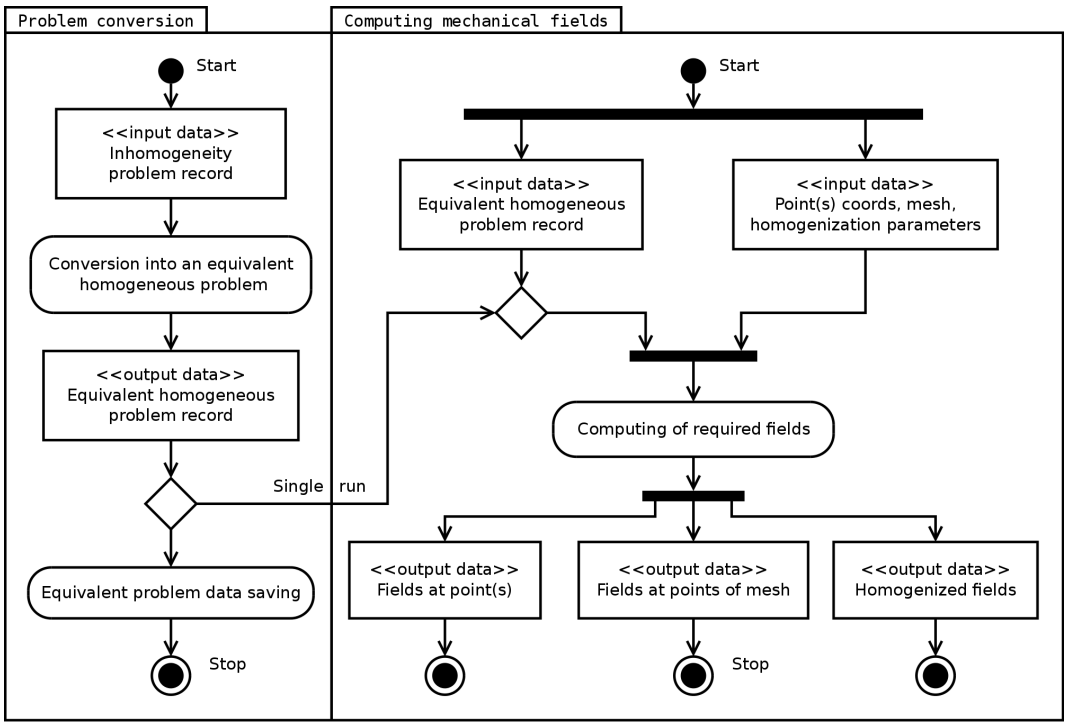

Figure 5: Implementation scheme.

3. Implementation

Recall that the μMECH library was primarily designed as a module of finite element packages. Its main goal is the evaluation and post-processing of macro-field perturbations, which may take over the role of microstructure-informed enrichments for partition of unity strategies. So far, the code is furnished with analytical solutions to two and three dimensional problems with inclusions of ellipsoidal shapes, such as an ellipse or a circle in two dimensions and an ellipsoid, sphere, oblate spheroid, prolate spheroid, penny, flat ellipsoid, cylinder, and elliptic cylinder in three dimensions. The 3D and 2D inputs can not be mixed as the library runs in either of the modes at a single instance. The functions are tuned in a way that inclusion of an arbitrary shape can be treated as a general ellipsoid with one or more degenerated semi-axes, e.g. a cylindrical fiber can be modeled as the ellipsoid with excessive a_1 semi-axis. By analogy, 2D plane strain conditions can be simulated as 3D cylinders with very long semi-axes parallel to global z coordinate. However, in this case, the solution losses from its computational efficiency and specific shapes should be preferred instead the degenerated ones, namely in situations when dealing with large numbers of inclusions (in orders of millions). Therefore, the inclusions defined as general ellipses/ellipsoids are automatically assigned relevant shapes according to the particular semi-axes dimensions by default.

A longer term ambition of the μMECH developers is to cover a maximum topics tackled by the micromechanics community. Therefore, the current release was also equipped with the classical homogenization techniques as discussed in Section 2. Moreover, to the best of our knowledge, the presented library is the only of its kind freely available at the time being.

3.1. Implementation scheme/Data flow structure

The general structure of μMECH is briefly outlined in Fig. 5. Basically, it splits in two major tasks, conversion of inhomogeneity problem to equivalent inclusion problem and evaluation of mechanical fields eventually homogenization. The first step is usually most time-consuming, however it needs to be performed only once and the appropriate data can be stored for subsequent analyzes over the same data, geometry and distribution of inhomogeneities to be exact[3]. The second branch of the algorithm can be called repeatedly to evaluate fields at different locations or to run different homogenization algorithms. However, in the single run cases, the code allows analyzes without saving and reading the auxiliary data.

Description of the inhomogeneity problem is required as the input for the first part of the algorithm. It consists of the geometry definitions (centroids, dimensions and rotation of semi-axes), material characteristics of the inhomogeneities and the matrix (Youngs modulus and Poisson's ratio), and definitions of imposed eigenstrains[4] and the remote strain tensors. The latter mentioned remote strains are handled as individual load cases and as such their number is arbitrary. The inhomogeneity inputs are converted into the equivalent problem by making use of Equivalent inclusion method and the self-compatibility procedure presented in Section 2. The stored data, if required, are the equivalent transformation eigenstrains $\boldsymbol{\varepsilon}_r^\tau$ and local (say internal) Eshelby tensors $\mathbf{S}_r$.

In the second part of the algorithm, mechanical fields at user-defined points, including those outside inclusions, are evaluated. Individual $\mathbf{x}$ coordinates can be entered one by one or in arbitrarily large sets, e.g. nodes or integration points of an FE mesh. Calculated fields may be postprocessed with the in-built post-processor and visualized with tools as Paraview, MayaVi, etc.[17, 18]. Another in-built feature is the homogenization of calculated local fields by DIM introduced in Section 2.6. Optionally, users can disable the self-compatibility algorithm and the evaluation of local fields and use alternative micromechanical approaches discussed also therein.

3.2. I/O data specification

The library is designed in a way a user or a master program invokes the feedback by using a set of C++ functions. Despite, the I/O data flow between μMECH and a governing instance can be realized via parameters of the interface functions, the exchange by means of files is also possible as it proved to be more practical especially for large number of inclusions. In both cases, the data have a unified syntax. Symmetric tensors are handled in a non-reduced form and together with non-symmetric tensors, e.g. $\mathbf{S}$, are stored in row-by-row vectors, in the so called Iliffe arrays. In 2D mode the input data can be reduced correspondingly, i.e. coordinates may have only two components, 2-nd order tensors are of dimensions 2×2, etc. In particular, following data are handled by means of files, the inhomogeneity and equivalent homogeneous problem records, grids of point coordinates[5] in which the mechanical fields are evaluated, and finally the sought fields themselves, see Fig. 5. The ASCII Visualization Tool Kit (VTK) format in both legacy and XML variants has been chosen as the native file syntax [19], as it is human-readable and can be visualized directly in a modeler or free

[3]Note again that the primary purpose of μMECH is feeding FE packages with subscale data.

[4]Due to the induced pore pressure or thermal expansion for example.

[5]it can be e.g. an FE triangulation

```
# vtk DataFile Version 3.0
3D - example, 2 inclusions
ASCII
DATASET UNSTRUCTURED_GRID
POINTS 2 float
-1.0   1.0  0.0
 2.0   0.0  0.0
POINT_DATA 2
VECTORS Semiaxes_dimensions float
1.0 1.0 1.0
1.0 0.7 0.4
VECTORS Euller_angles_deg float
0.0 0.0 0.0
35.0 0.0 0.0
SCALARS Youngs_modulus float 1
LOOKUP_TABLE default
5.5
2.4
SCALARS Poissons_ratio float 1
LOOKUP_TABLE default
0.3
0.3
TENSORS Imposed_eigenstrains float
0.0 0.0 0.0 0.0 0.0 0.0 0.0 0.0 0.0
0.0 0.0 0.0 0.0 0.0 0.0 0.0 0.0 0.0
FIELD unstructured_data 2
Matrix_record 1 2 float
1.0  0.4
Remote_strains 9 3 float
1.0 0.0 0.0 0.0 0.0 0.0 0.0 0.0 0.0
0.0 0.0 0.0 0.0 1.0 0.0 0.0 0.0 0.0
2.0 1.5 0.0 1.5 0.0 0.0 0.0 0.0 3.0
```

Table 2: Double inclusion problem input file in legacy VTK format.

visualization tool-kits [17, 18]. Therefore, the data can be easily controlled at any stage of the software development, debugging, or most importantly, in a routine use.

An example of the legacy VTK file with a composite media description is shown in Tab. 2. It describes the 3D matrix with a spherical and an ellipsoidal inclusions loaded by three remote strains. The dimension of the problem is explicitly determined by the "3D" keyword at the beginning of the second line, which is originally reserved for comments. The number of inclusions and centroid coordinates are given in the data block following the keyword "POINTS". Dimensions and rotation of semi-axes, and material characteristics of each inclusion are listed in the section introduced by "POINT_DATA". Finally, the data describing the infinite medium are specified in the section preceded by the "FIELD" keyword. In particular, these are Youngs modulus and Poisson's ratio of the matrix and the remote strain tensors.

3.3. Interface functions

The class `Problem` is the central element, better say a type, of the object-oriented source code and the vast majority of μMECH features is accessed through its public members. A rep-

```
 1 Problem *p = new Problem;
 2 p->read_input_file("inhomogeneity.vtk");
 3 p->input_data_initialize_and_check_consistency();
 4 p->convert_to_equivalent_problem();
 5 p->print_equivalent_problem("equivalent.vtk");
 6 delete p;
 7 p = new Problem;
 8 p->read_input_file("equivalent.vtk");
 9 p->input_data_initialize_and_check_consistency();
10 double coords[] = {0.5,0.0,0.0};
11 double **stress = AllocateArray2D(2,9);
12 p->giveFieldsOfPoint(NULL,NULL,stress,coords,'p',0,2);
13 p->printFieldsOnMeshVTK("results.vtk","mesh.vtk",'t',2,1);
14 p->print_visualization("visualization.vtk",5);
15 delete p;
16 DeleteArray2D(stress,2);
```

Table 3: Example code of μMECH interface.

resentative implementation calling crucial functions of the inhomogeneity problem analysis is listed in Tab. 3.

Line 2 is responsible for importing a complete problem description from the VTK file listed in Tab. 2. The data initialization and verification follows in line 3. Line 4 converts the inhomogeneity problem into the equivalent inclusion problem. The data for multiple use of the problem geometry are stored in line 5, if required. As demonstrated in lines 6-9, imports of both, the inhomogeneity and equivalent homogeneous problems work in the same fashion. Clearly, lines 5-9 or 6-9 can be omitted in the case of a single run.

The function `giveFieldsOfPoint` evaluates mechanical fields at a given point, lines 10-12. Displacement, strain and stress fields are returned by means of the first three parameters, respectively. Each of the parameters is a double pointer to the two-dimensional array. The first dimension is equal to the number of load cases, i.e. remote strains specified at the end of the input file, Tab. 2. The second dimension equals the length of the vector, in the case of displacements, or row-by-row stored tensors when recalling strains or stresses. Passing `NULL` pointer indicates that the corresponding quantities will not be calculated. The fourth parameter is a pointer to an array of the point coordinates. The next `char` parameter denotes the character of evaluated fields where 'p' stands for perturbations while 't' for their total counterparts, see Section 2. Finally, the last two parameters determine the index of the first load case and number of load cases to be comprised in the analysis. In this particular case, a pair of perturbation stress tensors due to the first (0-th in C-like syntax) and second remote strain excitations are evaluated in line 12. The data visualized in Paraview are shown in Fig. 6b.

In line 13, function `printFieldsOnMeshVTK` reads the FE mesh from *mesh.vtk* file and evaluates total fields in element nodes and the third given remote strain. Then the mesh with results is stored in the file *results.vtk*. Finally, line 14 performs triangulation of inclusion surfaces which is written in *visualization.vtk* file. The data visualized in Paraview are shown in Fig. 6a.

A detailed description of other interface functions can be found in tutorial [20] together with a number of ways how to control the analysis, e.g. functions for running different homogenization algorithms, the switch parameter between *full* and *optimal* version of either the self-compatibility procedure or evaluation of perturbation/total fields at different points, etc.

3.4. Technology

μMECH is a free open source software. It can be run, modified, and redistributed under the terms of the GNU Lesser General Public License as published by the Free Software Foundation; either version 2 of the License, or any later version [21]. The project has been implemented in C++, as it is easier to maintain accessibility of its generic structure while it also enables robust low level optimization of time-consuming algorithms. Multi platform CMake [22] was chosen to configure and build source code properly on client machines. A complete source code and documentation generated by Doxygen [23] script can be found at `http://mumech.cz`, together with a number of examples and input files by means of which we perform the compilation of an executable file and testing. All interface functions and examples are documented in a tutorial also available at the project website.

4. Numerical examples and performance

The capabilities of the μMECH library are briefly demonstrated through a 3D double inclusion task and a series of 2D multiple inclusion examples under plane strain conditions. The 3D analysis is composed of a pair of inclusions, one ellipsoid and sphere. The geometry, topology and material parameters together with the prescribed strain excitation are specified in Tab. 2. In addition, the geometry triangulated by μMECH and visualized in Paraview is shown in Fig. 6a while the distribution of axial stress σ_{11} is plotted in Fig. 6b. In order to dis-

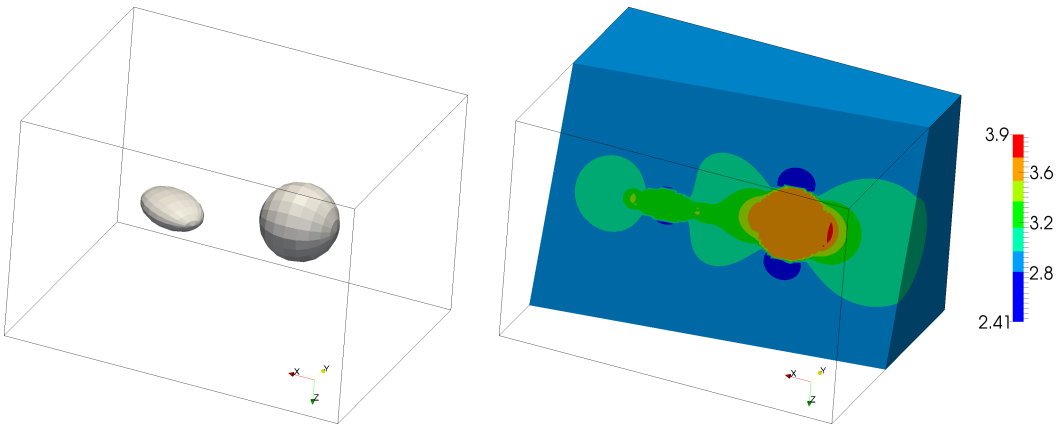

Figure 6: Example of 3D double inclusion problem, a) benchmark geometry, b) patterns of σ_{11}.

cuss the quality of solutions by μMECH we have compared the 2D analyzes with reference solutions by FEM. The tests were performed in the 2D setting for the better visualization purposes, however we have executed the same calculations by means of the 3D implementation with degenerated semi-axis and arrived at exactly the same results. The first task is the single elliptic inclusion problem. The second and third tasks are the triple inclusion tests

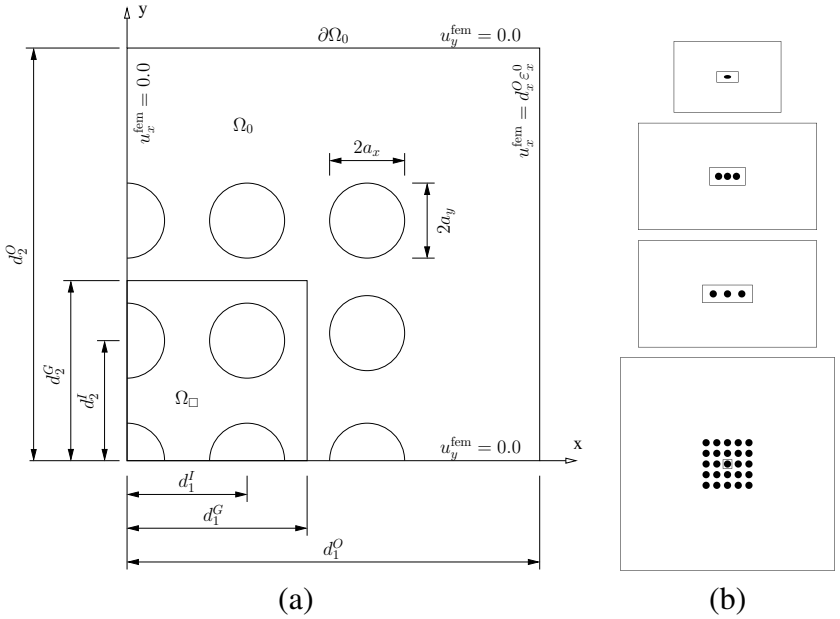

Figure 7: Geometry of 2D benchmarks, a) parametric setting of tested benchmarks, b) particular geometry of single, triple - narrow gaps, triple - wider gaps, and multiple inclusion test.

with centroids of circular inclusions aligned in x direction. The two tasks differ in the mutual distances among the inclusions. The last test comprises 25 circular inclusions distributed in a regular grid of 5×5 points in $x - y$ plane and representing inclusion centroids. The geometry of all four tests is given by the parameters in Tab. 4 whose meaning is evident from Fig. 7. The material parameters were set to $E_r = 10.0, \nu_r = 0.3, E_0 = 1.0, \nu_0 = 0.2$ for all the analyzes. Finally, the remote strain excitation imposed to the infinite matrix was such that $\boldsymbol{\varepsilon}_{11}^0 = 1.0$ while the other components vanished. Note, in the case of FE comparative analyzes, appropriate the remote strains were imposed by means of the boundary displacements $u_i^{\rm fem}$ applied on $\partial\Omega_0$. The particular magnitude of $u_i^{\rm fem}$ is evident from Fig. 7a. The

No. inclusions	a_1	a_2	d_1^I	d_2^I	d_1^G	d_2^G	d_1^O	d_2^O
1×1	1.0	0.5	-	-	3.0	1.5	15.0	10.0
3×1 (narrow gaps)	1.0	1.0	2.5	-	5.0	2.5	25.0	15.0
3×1 (wider gaps)	1.0	1.0	4.0	-	7.0	2.5	25.0	15.0
5×5	1.0	1.0	3.0	3.0	1.5	1.5	30.0	30.0

Table 4: Geometrical and topological parameters of four 2D tasks performed.

qualitative comparison of the three types of solutions, (i) a solution without performing self-compatibility algorithm (labeled as μMECH 1 in the sequel), (ii) a solution including the adjustment by means of the self-compatibility algorithm and the non-constant approximation to internal fields as proposed in Paragraph 2.5, and (iii) the previous solution μMECH 2 enhanced by the approximation to external fields calculated by means of linear transformation eigenstrains (labeled as μMECH 3). The distribution of σ_{11} for the single inclusion problem calculated by μMECH is shown in Fig. 8a. The comparison with the FEM solution in terms of total strain components in x–axis direction is evident from Fig. 8b. The series of

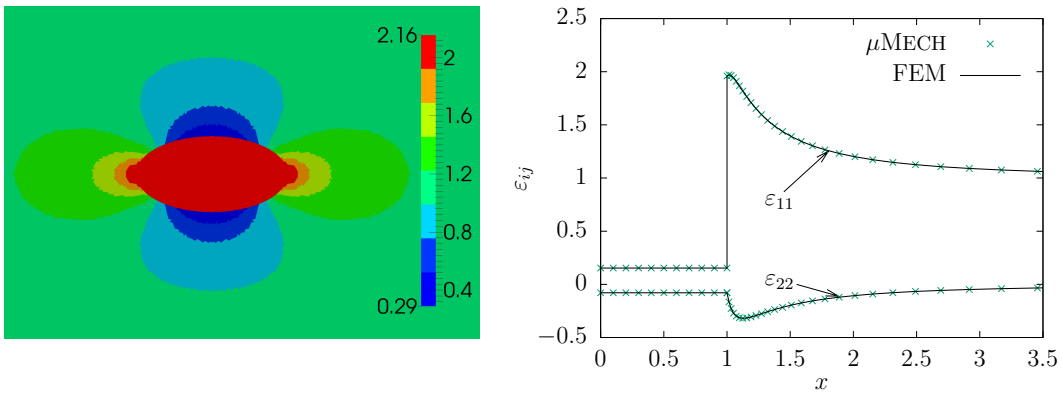

(a) (b)

Figure 8: Single inclusion test, a) patterns of σ_{11} calculated by μMECH, b) total strain components along x-axis.

figures with individual strain components compared with respect to FE solutions for remaining tasks are displayed in Fig. 9 and Fig. 10. Note namely the obvious local convergence of individual μMECH methods 1–3 to the reference solution. In the case of multiple inclusions, the mechanical fields within individual inclusions are not uniformly distributed as a result of their mutual interaction. There is an evident difference for strains taking place in the matrix, namely for inclusions positioned close to each other, Fig. 9a and Fig. 10. However, the mutual interactions quickly disappear with increasing spacing as shown in Fig. 9b. An interesting behavior can be observed in Fig. 10b,c from which it is obvious that μMECH 3 method looses in y–direction with respect to its 1–2 counterparts. The reason is the low polynomial order, linear to be exact, of $\boldsymbol{\varepsilon}^{\tau}(\mathbf{x})$ as indicated by analyzes with quadratic eigenstrains. A detailed justification of this hypothesis, however, is let for future work as the current implementation of the solution with quadratic eigenstrains is not furnished with analytical derivatives of elliptic potentials and the numerical differentiation is unstable enough to disable reliable testing. Looking carefully at Fig. 9c and Fig. 10b one can observe Gibbs-like phenomenon at the inclusion interfaces related to the fact the solution to external fields is constructed as the sum of individual contributions from all n inclusions entering the analysis, for details see Section 2. Clearly, this is nonphysical, though inevitable behavior that must be accepted when using current version of the μMECH library.

The quality of the μMECH solutions was further quantified in an average sense by means of the normalized error defined as

$$\mathrm{err} = \frac{\|\boldsymbol{e}\|}{\|\boldsymbol{e}^{\mathrm{tot}}\|} \times 100\% \tag{43}$$

where $\|\boldsymbol{e}\| = \sqrt{\int_{\Omega_\square} \boldsymbol{e}_\varepsilon : \mathbf{C} : \boldsymbol{e}_\varepsilon \,\mathrm{d}\Omega}$, $\|\boldsymbol{e}^{\mathrm{tot}}\| = \sqrt{\int_{\Omega_\square} \boldsymbol{\varepsilon} : \mathbf{C} : \boldsymbol{\varepsilon} \,\mathrm{d}\Omega}$, and $\boldsymbol{e}_\varepsilon = \boldsymbol{\varepsilon} - \boldsymbol{\varepsilon}^{\mathrm{fem}}$. The resulting values for the triplet of methods are listed in Tab. 5. The results clearly show the superiority of the μMECH 3 method over the remaining two. The last analyzes performed cover the testing of homogenization approaches, namely that based on the direct integration – DIM, and classical micromechanical schemes. Note, that in the case of DIM we took the integration domain $\Omega_\square$ as indicated in Fig. 7a. Results for two different volume fractions c_r, proportional to the gaps among the inclusions as parametrized in Tab. 4, are listed in Tab. 6 and Tab. 7. The fit among all schemes is remarkable but the Self-Consistent scheme which is

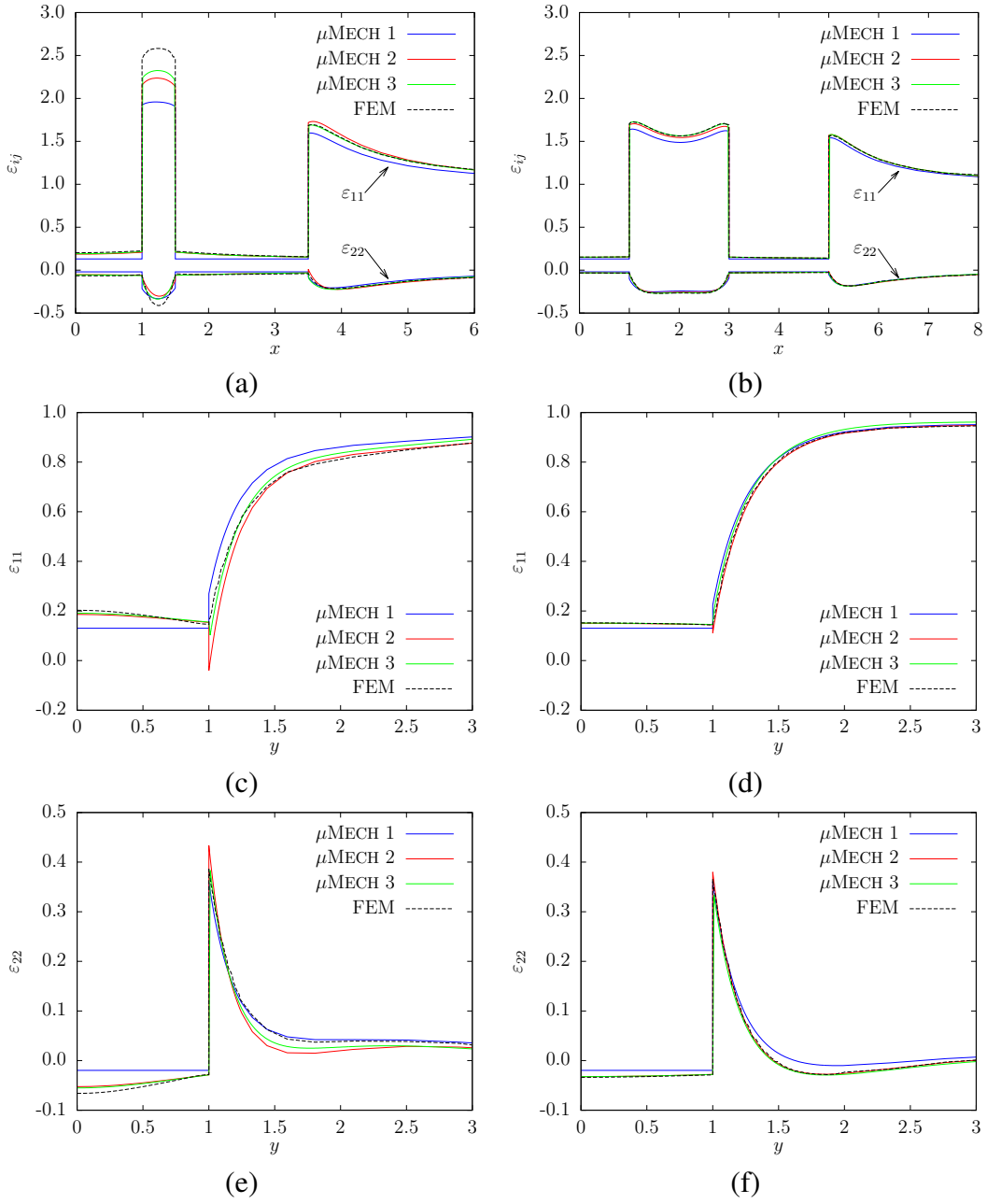

Figure 9: Triple inclusion tests, a,b) total strain components along x-axis for inclusions with narrow and wider gaps, respectively, c,d) total strain components along y-axis for inclusions with narrow and wider gaps, respectively.

known to overestimate the moduli for lower volume fractions of stiff inclusions. Moreover, it appears that for both configurations, either narrow or wider gaps, 3×3 inclusions adjacent to that inside $\Omega_{\square}$ is far sufficient for very accurate results.

5. Conclusions

In the present paper we discussed a new and, to the best of our knowledge, the only freely available library of solutions to micromechanical problems based on Eshelby's seminal work [1] and its subsequent extensive elaboration in classical textbooks as e.g. [5]. Con-

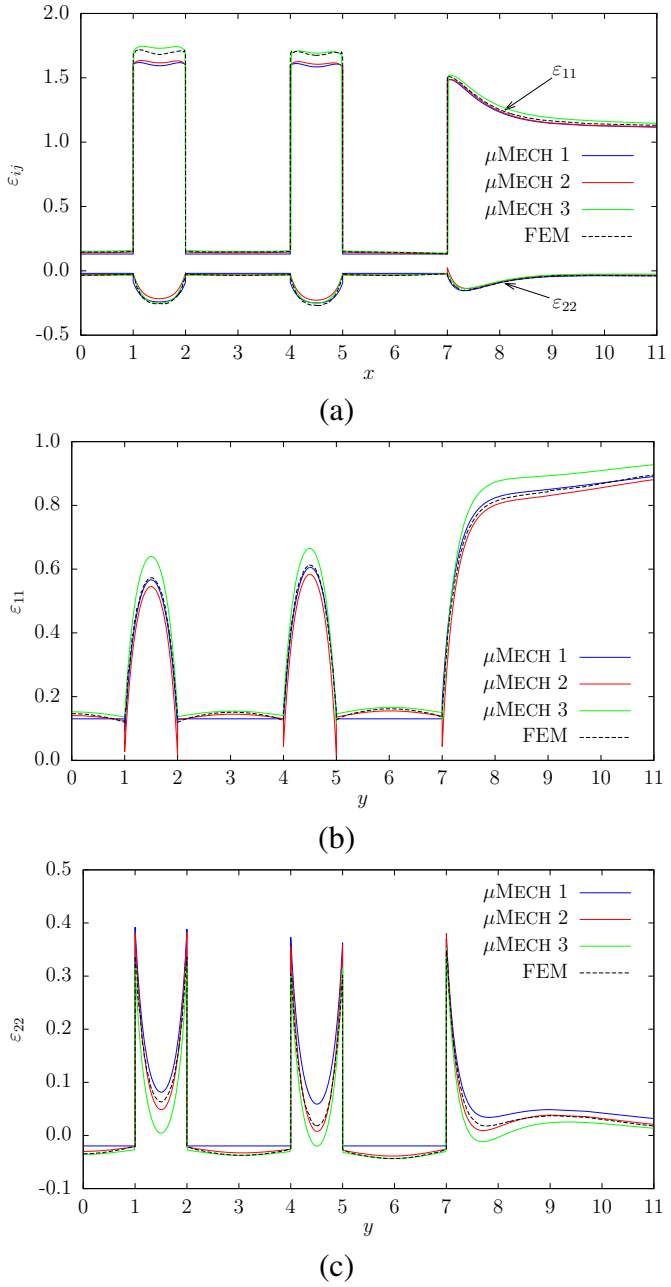

Figure 10: Multiple inclusion test, a) total strain components along x-axis, b) total strain components along y-axis.

trary to what is meant as a standard in classical micromechanics, the implemented strategies aim at the evaluation of perturbation or total local fields inside and outside ellipsoidal inclusions. The code also covers the solution to multiple inclusion problems by means of the so called self-compatibility algorithm. This strategy benefits from the solution to the inclusion problem with polynomial eigenstrains. As this is the crucial part of the code we will keep improving it in the future, possibly with the help of new members of the emerging developers community motivated also by means of the present paper. Besides, the library is furnished with classical homogenization theories such as Mori-Tanaka, Self-Consistent method etc. On the basis of the above comments, let us stress current features of the μMECH library and

Evaluation method	No. inclusions		
	3×1 (narrow gaps)	3×1 (wider gaps)	5×5
μMECH 1	17.1	3.9	4.5
μMECH 2	7.6	1.7	3.2
μMECH 3	6.9	1.4	2.6

Table 5: Normalized errors according to Eq. (43) and measured in %.

Computation scheme	Stiffness tensor moduli			Isotropic moduli	
	$C_{1111} = C_{2222}$	$C_{1112} = C_{2212}$	C_{1212}	E	ν
Self-Consistent	3.3461	1.0712	1.1374	2.82	0.24
Diff. Scheme	2.2149	0.6456	0.9093	1.92	0.22
Mori-Tanaka	2.6811	0.8005	0.9402	2.31	0.22
Dilute	1.9309	0.5357	0.6976	1.69	0.21
DIM 1×1	2.6833	0.7860	0.9264	2.31	0.22
DIM 3×3	2.8323	0.6265	0.8593	2.51	0.20
DIM 5×5	2.8417	0.6233	0.8541	2.52	0.20
DIM 7×7	2.8411	0.6261	0.8529	2.52	0.20
DIM 9×9	2.8406	0.6274	0.8525	2.52	0.20
FEM	2.8883	0.6531	0.8615	2.55	0.20

Table 6: Homogenized stiffness moduli for monodisperse with narrow gaps of $c_r = 0.5$. DIM results were obtained by means of μMECH 3 method. Isotropic moduli in last two columns were derived from eigenvalue analysis of $\mathbb{C}$ as reported in [24].

a few proposals for further development as follows.
Implemented features:

- solutions to internal and external fields in two and three dimensions,
- an approximate solution to the multiple inhomogeneity/inclusion problem by means of the self-compatibility algorithm,
- the solution to the equivalent inclusion problem with polynomial stress free transformation eigenstrains,
- a powerful I/O interface based on the VTK standard,
- various homogenization schemes as Mori-Tanaka, Self-consistent method, dilute approximation, direct integration, and the differential scheme.

Future development will focus on:

- a Galerkin-like approximation to the multiple inclusion problem with Eshelby functions at heart,
- a direct link between μMECH core implementation and a F# class for polynomial eigenstrain based solutions,
- a parallelization of the solution to the multiple inclusion problem,

Computation scheme	Stiffness tensor moduli			Isotropic moduli	
	$C_{1111} = C_{2222}$	$C_{1112} = C_{2212}$	C_{1212}	E	ν
Self-Consistent	1.8511	0.5235	0.6639	1.62	0.22
Diff. scheme	1.6587	0.4556	0.6630	1.46	0.21
Mori-Tanaka	1.7417	0.4808	0.6304	1.53	0.21
Dilute	1.5722	0.4228	0.5746	1.39	0.21
DIM 1×1	1.7524	0.4774	0.6272	1.54	0.21
DIM 3×3	1.7889	0.4400	0.6046	1.59	0.20
DIM 5×5	1.7904	0.4391	0.6036	1.59	0.20
DIM 7×7	1.7905	0.4392	0.6033	1.59	0.20
DIM 9×9	1.7905	0.4392	0.6032	1.59	0.20
FEM	1.7854	0.4388	0.6017	1.58	0.20

Table 7: Homogenized stiffness moduli for monodisperse with narrow gaps of $c_r = 0.35$. DIM results were obtained by means of μMECH 3 method. Isotropic moduli in last two columns were derived from eigenvalue analysis of $\mathbb{C}$ as reported in [24].

- a special care of the Gibbs-like phenomenon taking place at the inclusion interfaces.

Acknowledgements

The authors gratefully acknowledge the endowment of the Czech Science Foundation under the grant no. 13-22230S. We also thank Martin Doškář of CTU in Prague for careful reading of the manuscript and valuable comments on its scientific exposition.

References

[1] J. D. Eshelby, The determination of the elastic field of an ellipsoidal inclusion, and related problems, Proceedings of the Royal Society of London. Series A, Mathematical and Physical Sciences 241 (1226) (1957) 376–396. doi:10.1098/rspa.1957.0133.

[2] J. Novák, Ł. Kaczmarczyk, P. Grassl, J. Zeman, C. J. Pearce, A micromechanics-enhanced finite element formulation for modelling heterogeneous materials, Computer Methods in Applied Mechanics and Engineering 201 (2012) 53–64. doi:10.1016/j.cma.2011.09.003.

[3] T. Mori, K. Tanaka, Average stress in matrix and average elastic energy of materials with misfitting inclusions, Acta Metallurgica 21 (5) (1973) 571 – 574. doi:10.1016/0001-6160(73)90064-3.

[4] M. Šejnoha, J. Zeman, Micromechanics in practice, WIT Press, 2013.

[5] T. Mura, Micromechanics of Defects in Solids., Martinus Nijhoff Publishers, P. O. Box 163, 3300 AD Dordrecht, The Netherlands, 1987. 587.doi:10.1007/978-94-009-3489-4.

[6] J. Novák, Calculation of elastic stresses and strains inside a medium with multiple isolated inclusions, in: M. Papadrakakis, B. Topping (Eds.), Proceedings of the Sixth International Conference on Engineering Computational Technology, Stirlingshire, UK, 2008, p. 16 pp, paper 127. doi:10.4203/ccp.89.127.

[7] B. Pichler, C. Hellmich, et al., Estimation of influence tensors for eigenstressed multiphase elastic media with nonaligned inclusion phases of arbitrary ellipsoidal shape, Journal of Engineering Mechanics 136 (2010) 1043–1053. doi:10.1061/(ASCE)EM.1943-7889.0000138.

[8] J. Zeman, Analysis of composite materials with random microstructure, Ph.D. thesis, Czech Technical University (2003).

[9] R. Hill, Elastic properties of reinforced solids: Some theoretical principles, Journal of the Mechanics and Physics of Solids 11 (5) (1963) 357 – 372. doi:10.1016/0022-5096(63)90036-X.

[10] L. J. Walpole, On the overall elastic moduli of composite materials, Journal of the Mechanics and Physics of Solids 17 (4) (1969) 235–251. doi:10.1016/0022-5096(69)90014-3.

[11] H. J. Böhm, A short introduction to basic aspects of continuum micromechanics, Cdl-fmd Report 3.

[12] Y. Guéguen, T. Chelidze, M. Le Ravalec, Microstructures, percolation thresholds, and rock physical properties, Tectonophysics 279 (1-4) (1997) 23–35. doi:10.1016/S0040-1951(97)00132-7.

[13] R. Hill, A self-consistent mechanics of composite materials, Journal of the Mechanics and Physics of Solids 13 (4) (1965) 213 – 222. doi:10.1016/0022-5096(65)90010-4.

[14] M. Cai, H. Horii, A constitutive model and fem analysis of jointed rock masses, in: International journal of rock mechanics and mining sciences & geomechanics abstracts, Vol. 30, Elsevier, 1993, pp. 351–359. doi:10.1016/0148-9062(93)91719-Y.

[15] A. Gavazzi, D. Lagoudas, On the numerical evaluation of Eshelby's tensor and its application to elastoplastic fibrous composites, Computational Mechanics 7 (1) (1990) 13–19. doi:10.1007/BF00370053.

[16] J. Vorel, J. Zeman, M. Šejnoha, Homogenization of plain weave composites with imperfect microstructure. part ii. analysis of real-world materials, International Journal for Multiscale Computational Engineering 11 (5). doi:10.1615/IntJMultCompEng.2013004866.

[17] Paraview, home page.
URL http://www.paraview.org

[18] MayaVi, home page.
URL http://mayavi.sourceforge.net

[19] VTK file format, manual.
URL www.vtk.org/VTK/img/???le-formats.pdf

[20] muMECH, home page.
URL http://www.mumech.cz

[21] GNU Lesser General Public License.
URL http://www.gnu.org/copyleft/lgpl.html

[22] CMake, cross-platform make, home page.
URL http://www.cmake.org

[23] Doxygen, home page.
URL http://www.stack.nl/dimitri/doxygen/

[24] M. Doškář, J. Novák, A jigsaw puzzle framework for homogenization of high porosity foams, Computers & Structures 166 (2016) 33–41. doi:10.1016/j.compstruc.2016.01.003.

Chapter 4

SYNTHESIS OF RANDOM MICROSTRUCTURAL GEOMETRIES

Although Eshelby's based closed form solutions, inbuilt in the in-house developed μMech platform, allow for evaluating self-compatible strains and displacements and self-equilibrated stress fluctuations in infinite media containing hundreds of thousands ellipsoidal inclusions with a reasonable computational overhead, the goal was set to evaluate even higher numbers of inclusions of arbitrary shape. Such a target thus ultimately calls for using numerical strategies as Finite Element Method when it comes to generic inclusion shape and a strategy that would handle the vast number of heterogeneity and their complex spatial arrangement. This chapter thus deals with the introduction to the Wang tiling based microstructure modeling method that generalizes the periodic unit cell concept, still preserves the random character of heterogeneity spatial arrangement and is computational feasible at the same time. The method, as it is presented here, builds on the results of Computer Graphics community that is combined with approaches common in the field of Materials Engineering and microstructural modeling in particular. The results were promising that triggered the usage of similar principles for reconstructing geometrically consistent microstructure-enrichment functions presented in the final chapter.

List of selected journal papers and book chapters

Novák, J., Kučerová, A., and Zeman, J. (2012). Compressing random microstructures via stochastic wang tilings. *Physical Review E*, 86(4):040104.

Compressing Random Microstructures via Stochastic Wang Tilings

Jan Novák

Experimental Centre, Faculty of Civil Engineering, Czech Technical University in Prague, Czech Republic

Anna Kučerová

Department of Mechanics, Faculty of Civil Engineering, Czech Technical University in Prague, Czech Republic

Jan Zeman

Department of Mechanics, Faculty of Civil Engineering, Czech Technical University in Prague, Czech Republic

Abstract

This paper presents a stochastic Wang tiling based technique to compress or reconstruct disordered microstructures on the basis of given spatial statistics. Unlike the existing approaches based on a single unit cell, it utilizes a finite set of tiles assembled by a stochastic tiling algorithm, thereby allowing to accurately reproduce long-range orientation orders in a computationally efficient manner. Although the basic features of the method are demonstrated for a two-dimensional particulate suspension, the present framework is fully extensible to generic multi-dimensional media.

Keywords: Microstructure compression, reconstructing algorithms, Wang tiles, aperiodic tilings

In 1961, Hao Wang introduced a tiling concept based on square dominoes with colored edges permitting their mutual assembly in a geometrically compatible (hard) manner [1]. Since then, his tiles have been the subject of studies in discrete mathematics [2, 3, 4] and found an extensive use in computer graphics [5], game industry [6], theory of quasicrystals [7] or biology [8]. From the perspective of this paper, the appealing feature of Wang tilings is that they can compress and reproduce naturally looking planar patterns or three-dimensional surfaces by employing only a small number of distinct tiles [9, 3, 10]. Motivated by this observation, we further explore the potential of Wang tiles to represent long-range spatial correlations in disordered microstructures; a problem common to materials science [11], geostatistics [12] or image analysis [13].

In this regard, two closely related applications can be distinguished, namely the *microstructure reconstruction* [14, 15, 16] based on given spatial statistics and *microstructure compression* [17, 18, 19] aiming at efficient representation of materials structure in multi-scale computations [20]. Our focus is on the latter, since these procedures usually have the

Email addresses: novakja@fsv.cvut.cz (Jan Novák), Anna.Kucerova@cvut.cz (Anna Kučerová), jan.zeman@cvut.cz (Jan Zeman)

Published in Physical Review E

microstructure reconstruction techniques at heart, hereby covering the common features of both.

To the best of our knowledge, compression algorithms reported to date use a single cell (PUC) that is periodically extended to tile the plane in a deterministic manner [18]. Such structures then inevitably manifest strong long-range correlations with a period of the PUC dimensions. We shall demonstrate that these artifacts can be effectively controlled when utilizing small Wang tile sets [10, 3], carefully designed to capture morphological trademarks of compressed media, combined with fast stochastic Cohen-Shade-Hiller-Deussen (CSHD) tiling algorithm [5] for real-time texture generation. A potential of this approach will be demonstrated for equilibrium two-dimensional particulate suspensions consisting of equisized disks of radius ρ uniformly distributed in a homogeneous matrix, cf. [21].

To this goal, consider a two-dimensional microstructured domain $\mathcal{D}$ discretized by a regular square lattice. Each lattice cell contains specific morphological patterns that are compatible on contiguous boundaries, Fig. 1(b). If there are no missing cells in $\mathcal{D}$, the discretization is called a *valid tiling*, and a single cell is referred to as the *Wang tile* [1], Fig. 1(a). The tiles have different codes on their edges, lower-case Greek symbols in Fig. 1(a), and are not allowed to rotate when tiling a plane. The number of distinct tiles within $\mathcal{D}$ is limited, though arranged in such a fashion that none of them or any of their sub-sequence periodically repeats. The gathered distinct tiles are referred to as the *tile set*, Fig. 1(a). Sets that enable uncountably many, always aperiodic, tilings are called *aperiodic* [3, 4]. In real world applications, the assumption of strict aperiodicity of the tile sets is relaxed to aperiodicity of tilings, ensured e.g. by the CSHD algorithm [5] introduced next.

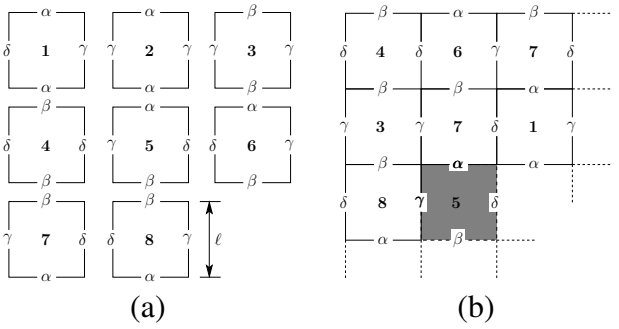

Figure 1: (a) A Wang tile set W8/2–2 with edge length ℓ and codes $\{\alpha, \beta, \gamma, \delta\}$. (b) Example of an aperiodic valid tiling.

Intuitively, the ability of a tile set to control long-range order effects arises from tile and edge code diversities, Fig. 1(a). Both factors are related, so that while the number of edge codes n_i^{c} in i–th spatial direction can be chosen arbitrarily, the number of tiles n^{t} must satisfy

$$n^{\mathrm{t}} = n^{\mathrm{NW}}\sqrt{n^{\mathrm{cs}}}, \tag{1}$$

where $n^{\mathrm{cs}} = (n_1^{\mathrm{c}} n_2^{\mathrm{c}})^2$ is the number of tiles in the complete set and $n^{\mathrm{NW}} = 2, \ldots, \sqrt{n^{\mathrm{cs}}}$ stands for the optional number of tiles with identical arrangement of north-western (NW) edge codes. The complete set of n^{cs} tiles is obtained by permuting the chosen codes c_i. In valid tilings, the south-eastern edge codes must match those assigned to NW edges, Fig. 1(b). Thus, the tiles in the complete set are sorted according to existing NW edge code combinations and the desired number of tiles in a user defined set is formed by selecting n^{NW} of

unique tiles from each group. Such a set is referred to as W$n^{\mathrm{t}}/n_1^{\mathrm{c}}$–$n_2^{\mathrm{c}}$ in what follows. Notice that the W1/1–1 set corresponds to the PUC setting.

In the stochastic tiling algorithm, the index of a new tile to be placed is selected randomly with the uniform probability from an appropriate NW group compatible with the eastern code of the tile previously placed and the southern code of the tile above the one to be placed (edges α and δ in bold adjacent to shaded cell in Fig. 1(b)). Aperiodicity of the resulting tiling is guaranteed provided that the random generator never returns a periodic sequence of numbers and that each NW group contains at least two distinct tiles [5].

Analogously to the existing works on reconstruction and compression of random media, the tile morphologies are designed by an optimization procedure expressed in terms of suitable statistical descriptors. As our focus is to control long-range artifacts, we limit the exposition to the two-point probability function $S_2(\mathbf{x})$ [11]. For statistically uniform ergodic media, it provides the probability that two arbitrary points from $\mathcal{D}$, separated by $\mathbf{x}$, are simultaneously found in the particle phase. The function satisfies $S_2(\mathbf{0}) = \phi$, where ϕ is the volume fraction of particles, and $S_2(\mathbf{x}) \approx \phi^2$ for $\|\mathbf{x}\| > \lambda$ indicates the absence of long-range orders at the characteristic length λ, Fig. 2(b).

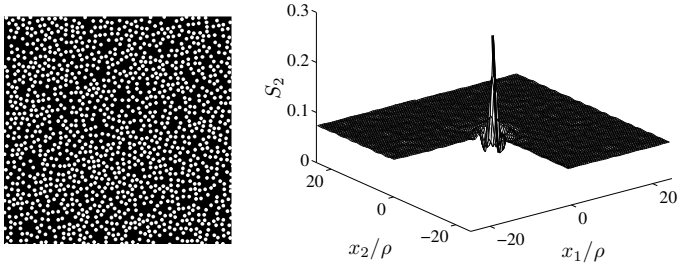

Figure 2: (a) Reference two-phase medium of size $174\rho \times 174\rho$ formed by equilibrium distribution of $1,300$ equi-sized disks of volume fraction 26.8% and (b) its two-point probability function S_2; ρ is the disk radius.

In the current setting, the Wang tiling compression consists of a set of n^{t} tiles of the edge length ℓ, in which we distribute n^{d} disks. The configuration of particles is determined by the parameter vector $[t_d, \xi_{1,d}, \xi_{2,d}]_{d=1}^{n^{\mathrm{d}}}$, where $t_d \in \{1, \ldots, n^{\mathrm{t}}\}$ specifies the parent tile index of the d-th disk and $\xi_{j,d} \in [0, \ell]$ the local position of the disk at j-th direction. To determine the two-point probability function $\widetilde{S}_2$ for a given configuration, we assemble a tiling that covers the domain of the same size as the representative sample $\mathcal{D}$, Fig. 2(a). Notice that such tiling corresponds to a realization of a statistically homogeneous material, since the tiles are selected from NW edge groups with the uniform probability. The proximity of the tile-based morphology to the original sample is quantified by an objective function

$$E = \frac{1}{|\mathcal{D}|} \int_{\mathcal{D}} \left(S_2(\mathbf{x}) - \widetilde{S}_2(\mathbf{x}) \right)^2 \mathrm{d}\mathbf{x} \tag{2}$$

which can be efficiently evaluated using the Fast Fourier Transform techniques, e.g. [11]. The minimization of (2) is carried out by the Simulated Re-Annealing method with computational cost similar to existing PUC design strategies [22]. The algorithm ensures that the tiles in the set satisfy the corner constraint [5], requiring that the tile corners are not occupied by a disk, and determines the number of disks n^{d} and the cell size ℓ such that the local

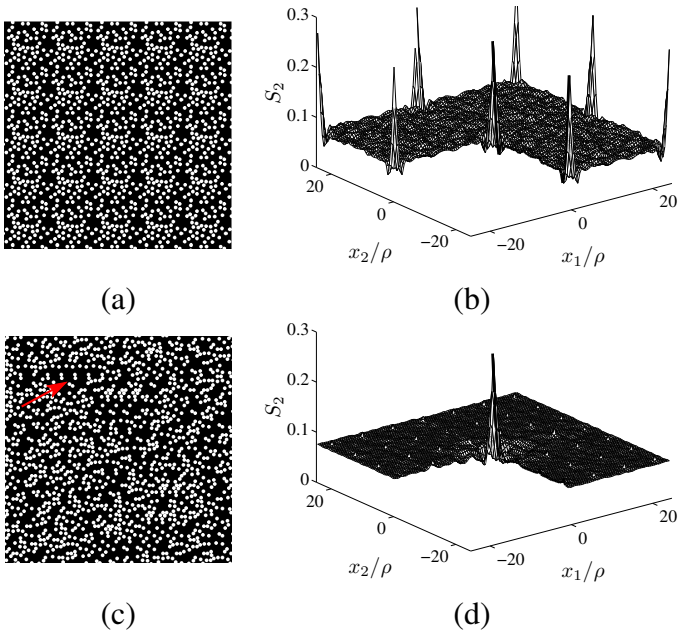

Figure 3: Optimized microstructures and two point probability functions $\widetilde{S}_2$ for PUC (a,b) and set W18/3–3 (c,d). Red arrow in (c) denotes periodic region due to local character of tile placement in CSHD tiling algorithm.

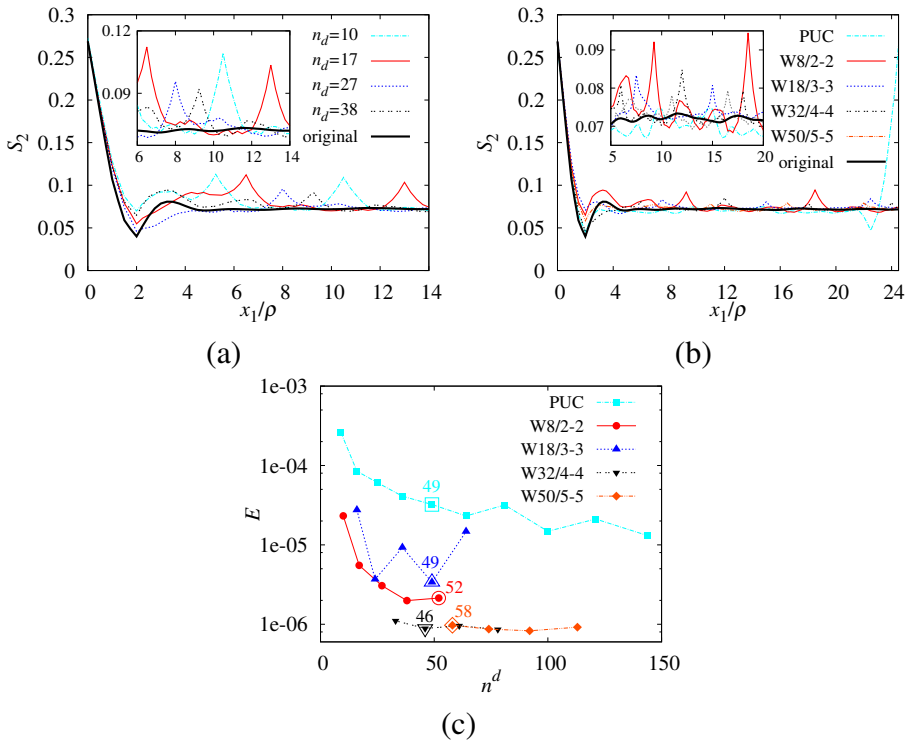

Figure 4: Comparison of $\widetilde{S}_2$ in x_1–S_2 plane for (a) tile set W8/2-2 with respect to number of disks n^{d} involved, (b) different sets. (c) Comparison of different sets in terms of objective function (2) and with respect to number of disks n^{d} involved. The curves in (b) are plotted for particular values of n^{d} highlighted in (c).

volume fractions associated with edges (red disks in Fig. 5) and tile interiors (white disks in Fig. 5) are as close to the target value ϕ as possible.

An example of optimal approximations of the target microstructure from Fig. 2 in terms

of a PUC and the Wang tile set W18/3–3 is shown in Fig. 3. The representations are based on $n^{\mathrm{d}} = 49$ particles and tile sizes $\ell = 24.5\rho$ and $\ell = 7.5\rho$, respectively. Evidently, both heterogeneity patterns carry long-range order effects with the period of ℓ, manifested as the local peaks

$$\widehat{S}_2 = \max_{\boldsymbol{k}\setminus\{\boldsymbol{0}\}} \widetilde{S}_2(\boldsymbol{k}\ell) \tag{3}$$

in the two-point probability functions, Fig. 3(b,d). Notice that $\widehat{S}_2$ is always equal to ϕ for the PUC approach, whereas the Wang tiles are capable of adjusting these artifacts by the proper morphology design. This is also reflected in visual regularity of the generated suspensions, compare Fig. 2(a) with Fig. 3(a,c). Also observe the locally periodic region in Fig. 3(c), arising from the local character of CSHD algorithm and from the lowest number of tiles in groups of admissible NW edge code combinations, $n^{\mathrm{NW}} = 2$. Such phenomenon is thus less likely when increasing parameter n^{NW}, however, at the expense of increasing set sizes, especially for higher edge code diversities, recall Eq. (1).

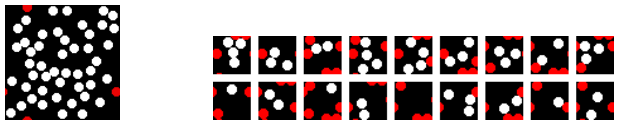

(a) (b)

Figure 5: Building blocks of microstructure compression based on (a) PUC and (b) tile set W18/3–3 with 49 disks assigned to tile edges (red) and interiors (white).

The principal features of Wang tile-based compressions are further illustrated in Fig. 5. Instead of relying on a single cell containing the complete morphological information, Fig. 5(a), the tiling-based approach utilizes substantially simpler building blocks, Fig. 5(b), assembled to comply with edge constraints (red disks in Fig. 5). This, however, restricts the space of admissible disk configurations in Wang tiles compared to the single PUC design.

Now, we are in the position to quantify to which extent is the quality of reconstructed suspensions determined by the tile set diversity and the morphology design itself. This aspect is examined first in Fig. 4 by means of sections of the two-point probabilities $S_2(x_1, 0)$ and the objective function E, revealing that two effects govern the amplitude and period of the local extremes $\widehat{S}_2$. First, for a fixed tile set, increasing the number of disks increases the tile edge dimension ℓ (and thus the period) and slightly decreases the amplitude, Fig. 4(a). On the other hand, increasing the number of tiles decreases the period as well as the magnitude of local extremes, Fig. 4(b). Also notice that the quality of the W18/3–3 set in terms of the objective function (2) is systematically inferior to W8/2–2, Fig. 4(c). This is caused by an inaccurate representation of disk volume fraction for the former set, which pollutes the shape of $\widehat{S}_2$ statistics, Fig. 4(b) [1]. It further follows from Fig. 4(c) that increasing the tile set diversity is much more efficient; for sets containing more than 32 tiles, the error is almost independent of the number of disks. This saturation value reflects the inaccurate representation of short-range values of S_2, caused by the particular form of the objective function (2). If needed, the local details can be incorporated in terms of higher-order statistics or specifically tailored descriptors [14, 15, 23, 24].

[1] The best resulting disk volume fraction for W18/3–3 and 24 disks was by 1.3% higher than the prescribed value. The remaining sets, however, never resulted in a worse scatter than 0.2%.

It is now clear that the local extremes can be attributed to a limited number of tiles used in a repetitive, although random fashion. Actually, two components repeat when tiling the plane: tile edges and interiors. To study the local artifacts analytically, we consider user defined sets with tiles selected so that their edges incorporate each code c_i at least once. Assuming that tiles and edges repeat independently, the local extremes can be estimated as

$$\widehat{S}_2^{\mathrm{p}} \approx \frac{\phi^{\mathrm{t}}}{n^{\mathrm{t}}}\left[\phi + (n^{\mathrm{t}}-1)\,\phi^2\right] + \frac{\phi^{\mathrm{e}}}{n_1^{\mathrm{c}} n_2^{\mathrm{c}}}\left[\phi + (n_1^{\mathrm{c}} n_2^{\mathrm{c}} - 1)\phi^2\right] \tag{4}$$

where $\phi^{\mathrm{t}} = (\ell - 4\rho)^2/\ell^2$ and $\phi^{\mathrm{e}} = 1 - \phi^{\mathrm{t}}$ denote the volume fractions of tile interiors (occupied by white disks in Fig. 5) and edges (occupied by red disks in Fig. 5), respectively [2].

In Fig. 6, we compare the actual values of $\widehat{S}_2$ with theoretical predictions (4) for several values of ϕ^{e}. Apart from the limit cases, $\phi^{\mathrm{e}} \in \{0, 1\}$, $\widehat{S}_2^{\mathrm{p}}$ was also explored for $\phi^{\mathrm{e}} = 0.2$ (average value from all considered tile sets). We observe that an almost exact match is obtained for the lower bound with $\phi^{\mathrm{e}} = 0$, red curve in Fig. 6(a), demonstrating that the long-range artifacts are carried mainly by the tile interiors. This is rather surprising, since all considered tile sets satisfy $n^{\mathrm{t}} \gg n_1^{\mathrm{c}} = n_2^{\mathrm{c}}$, so that edges repeat more often than the tile interiors. Moreover, the magnitude of spatial artifacts converges rapidly to the limit value ϕ^2. Altogether, this leads us to the conclusion that artifacts due to discrete nature of Wang tilings can be almost eliminated by a proper morphology optimization. Also note that the accuracy of the estimate (4) appears to be reasonable, both for the average value of $\phi^{\mathrm{e}} = 0.2$, blue curve in Fig. 6(a), as well as for values corresponding to individual tile sets, Fig. 6(b). It may thus serve as a basis for the a-priori selection of the tile set parameters n_i^{c} and n^{t}.

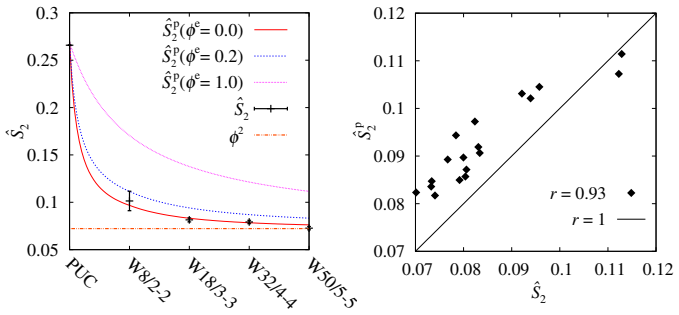

(a) (b)

Figure 6: (a) Dependence of local extremes $\widehat{S}_2$ on the particular tile set. (b) Correlation of local peaks obtained from two-point probabilities of optimized microstructures and their predictions given by Eq. (4); r in (b) denotes the Pearson correlation coefficient.

[2]Observe that the estimate (4) contains contributions from tile interiors and edges. In addition, the tile interior part arises from two complementary events. If the two adjacent tiles are identical, the probability of simultaneously locating two disks distant by ℓ amounts to $\phi^{\mathrm{t}}\phi/n^{\mathrm{t}}$. Otherwise, we consider the disks in both tiles as independent which gives rise to the term $\phi^{\mathrm{t}}(1 - 1/n^{\mathrm{t}})\phi^2$. The contribution of repeated tile edges is established analogously, by estimating the probability of simultaneously matching NW edge codes in the adjacent tiles as $1/n_1^{\mathrm{c}} \cdot 1/n_2^{\mathrm{c}}$.

Summary.

A new compression/reconstruction technique based on Wang tilings has been proposed and applied to two-dimensional microstructures of disordered particulate media. The technique is extensible to generic three-dimensional microstructures, adopting the frameworks of Wang cubes [25, 26] and image synthesis [5]; it substantially generalizes the periodic unit cell concept by making use of multiple tiles instead of a single cell, preserves long range spatial features, and is computationally efficient. A formula for estimates of long-range order spatial artifacts has also been proposed and verified for the studied material system.

Acknowledgement.

The authors acknowledge the Czech Science Foundation endowment under grants Nos. 105/12/0331 (JN) and 105/11/0411 (AK and JZ). The work by JZ was also partially supported by the European Regional Development Fund in the IT4Innovations Centre of Excellence project (CZ.1.05/1.1.00/02.0070). In addition, we would like to thank Jiří Šejnoha and Milan Jirásek of CTU in Prague and anonymous referees for helpful comments on the manuscript.

References

[1] H. Wang, Proving theorems by pattern recognition-II, Bell. Syst. Tech. J. 40 (1) (1961) 1–41.

[2] R. M. Robinson, Undecidability and nonperiodicity for tilings of the plane, Invent. Math. 12 (1971) 177–209.

[3] B. Grünbaum, G. Shephard, Tilings and patterns, WH Freeman & Co., 1986.

[4] K. Culik, An aperiodic set of 13 wang tiles, Discret. Math. 160 (1996) 245–251.

[5] M. Cohen, J. Shade, S. Hiller, O. Deussen, Wang tiles for image and texture generation, ACM Trans. Graph. 22 (3) (2003) 287–294.

[6] E. Demaine, M. Demaine, Jigsaw puzzles, edge matching, and polyomino packing: Connections and complexity, Graphs Comb. 23 (2007) 195–208.

[7] D. Aristoff, C. Radin, First order phase transition in a model of quasicrystals, J. Phys. A – Math. Theor. 44 (2011) 255001.

[8] E. Winfree, F. Liu, L. Wenzler, N. Seeman, Design and self-assembly of two-dimensional dna crystals, Nature 394 (6693) (1998) 539–544.

[9] A. Glassner, Andrew Glassner's notebook, IEEE Comput. Graph. Appl. 24 (1) (2004) 86–91.

[10] A. Lagae, P. Dutré, A comparison of methods for generating Poisson disk distributions, Comput. Graph. Forum 27 (1) (2008) 114–129.

[11] S. Torquato, Random heterogenous materials, Springer-Verag, New York, 2002.

[12] J. Chilés, P. Delfiner, Geostatistics, John Wiley & Sons, 1999.

[13] J. Serra, Image analysis and mathematical morphology, Academic Press, London, 1982.

[14] C. Yeong, S. Torquato, Reconstructing random media, Phys. Rev. E 57 (1) (1998) 495.

[15] P. Čapek, V. Hejtmánek, L. Brabec, A. Zikánová, M. Kočiřík, Stochastic reconstruction of particulate media using simulated annealing: Improving pore connectivity, Transp. Porous Media 76 (2009) 179–198.

[16] M. Davis, S. Walsh, M. Saar, Statistically reconstructing continuous isotropic and anisotropic two-phase media while preserving macroscopic material properties, Phys. Rev. E 83 (2) (2011) 026706.

[17] G. L. Povirk, Incorporation of microstructural information into models of two-phase materials, Acta Metall. Mater. 43 (8) (1995) 3199–3206.

[18] J. Zeman, M. Šejnoha, From random microstructures to representative volume elements, Model. Simul. Mater. Sci. Eng. 15 (2007) S325.

[19] H. Lee, M. Brandyberry, A. Tudor, K. Matouš, Three-dimensional reconstruction of statistically optimal unit cells of polydisperse particulate composites from microtomography, Phys. Rev. E 80 (6) (2009) 061301.

[20] D. T. Fullwood, S. R. Niezgoda, B. L. Adams, S. R. Kalidindi, Microstructure sensitive design for performance optimization, Prog. Mater. Sci. 55 (6) (2010) 477–562.

[21] M. D. Rintoul, S. Torquato, Reconstruction of the structure of dispersions, J. Colloid Interface Sci. 186 (2) (1997) 467–476.

[22] J. Novák, A. Kučerová, J. Zeman, Microstructural enrichment functions based on stochastic Wang tilings, available at `http://arxiv.org/abs/1110.4183` (2011).

[23] Y. Jiao, F. Stillinger, S. Torquato, A superior descriptor of random textures and its predictive capacity, Proc. Natl. Acad. Sci. U. S. A.

[24] R. Piasecki, A. Plastino, Entropic descriptor of a complex behaviour, Physica A 389 (3) (2010) 397–407.

[25] K. Culik, J. Kari, An aperiodic set of wang cubes, J. Univers. Comput. Sci. 1 (10) (1995) 675–686.

[26] A. Lu, D. S. Ebert, W. Qiao, M. Kraus, B. Mora, Volume illustration using wang cubes, ACM Trans. Graph. 26.

Chapter 5

SYNTHESIS OF MICROSTRUCTURE INFORMED ENRICHMENT FIELDS

In this chapter, the earlier promises in constructing realizations of statistically equivalent microstructural data is extended to constructing the sought microstructure-informed fluctuation fields, again encoded in Wang tiles by means of an optimization algorithm. Contrary to a single objective when reconstructing the geometrical data, the optimization's objective function for fluctuation fields combines compatibility requirements of encoded local fields and the geometry aperiodicity constraints at the same time. The microstructural enrichment functions are thus constructed from a small set of Wang tiles that are assembled by the same inexpensive skyline stochastic tiling algorithm as in the case of its purely geometry-driven counterpart. The local microstructural field patterns at the level of individual tile domains are defined to satisfy prescribed governing equations - selfequilibrated stress fluctuations in the case of this particular chapter. The microstructural compatibility is satisfied apriori as the geometry given by the binary images serves as spatial distribution of material coefficients for local stress field calculations.

List of selected journal papers and book chapters

Novák, J., Kučerová, A., and Zeman, J. (2013). Microstructural enrichment functions based on stochastic wang tilings. *Modelling and Simulation in Materials Science and Engineering*, 21(2):025014.

Microstructural enrichment functions based on stochastic Wang tilings

Jan Novák

Experimental Centre, Faculty of Civil Engineering, Czech Technical University in Prague, Czech Republic

Anna Kučerová

Department of Mechanics, Faculty of Civil Engineering, Czech Technical University in Prague, Czech Republic

Jan Zeman

Department of Mechanics, Faculty of Civil Engineering, Czech Technical University in Prague, Czech Republic

Abstract

This paper presents an approach to constructing microstructural enrichment functions to local fields in non-periodic heterogeneous materials with applications in Partition of Unity and Hybrid Finite Element schemes. It is based on a concept of aperiodic tilings by the Wang tiles, designed to produce microstructures morphologically similar to original media and enrichment functions that satisfy the underlying governing equations. An appealing feature of this approach is that the enrichment functions are defined only on a small set of square tiles and extended to larger domains by an inexpensive stochastic tiling algorithm in a non-periodic manner. Feasibility of the proposed methodology is demonstrated on constructions of stress enrichment functions for two-dimensional mono-disperse particulate media.

Keywords: Wang tiling, Microstructure optimisation, Enrichment functions, Partition of Unity, Trefftz method, FFT-based solver

1. Introduction

A detailed analysis of microstructured materials with the full resolution of heterogeneities by classical finite element methods has been found computationally prohibitive [34]. To overcome this, one option consists of modelling a coarse-scale problem with the help of homogenisation techniques based on effective material properties [10, 35, 15]. However, this may lead to a considerable loss of information on the fine scale behaviour, thereby resulting in an inaccurate assessment of microstructural effects on the global response and/or its evolution. An alternative, computationally appealing, strategy proceeds from generalised finite element formulations that enhance the approximation properties of standard finite element spaces by subscale-informed enrichment functions. Their design involves two related but

Email addresses: novakja@fsv.cvut.cz (Jan Novák), Anna.Kucerova@cvut.cz (Anna Kučerová), jan.zeman@cvut.cz (Jan Zeman)

contradictory aspects: (i) realistic representation of the underlying heterogeneity patterns and (ii) construction of complex enrichment functions in a computationally efficient manner. Here, we briefly review these issues for two finite element frameworks. The first one is based on the *partition of unity method*, introduced by Melenk and Babuška [26] and generalised in numerous aspects later on [2, 13]. The second one utilises the *hybrid Trefftz stress formulations* developed by Teixeira de Freitas [41], see also [17] for an overview. For simplicity, we restrict our attention to the small-strain linear elasticity in two dimensions. The following nomenclature is used in the sequel. Scalar quantities are denoted by plain letters, e.g. a or A, vectors and matrices are in bold as, e.g. $\boldsymbol{a}$ or $\boldsymbol{A}$. In addition, we adopt the Mandel vector-matrix representation of symmetric second- and fourth-order tensors, e.g. a_{ij} or A_{ijkl}, so that [28, Section 2.3]

$$\boldsymbol{a} = \begin{bmatrix} a_{11} \\ a_{22} \\ \sqrt{2}a_{12} \end{bmatrix}, \qquad \boldsymbol{A} = \begin{bmatrix} A_{1111} & A_{1122} & \sqrt{2}A_{1112} \\ A_{2211} & A_{2222} & \sqrt{2}A_{2212} \\ \sqrt{2}A_{1211} & \sqrt{2}A_{1222} & 2A_{1212} \end{bmatrix}.$$

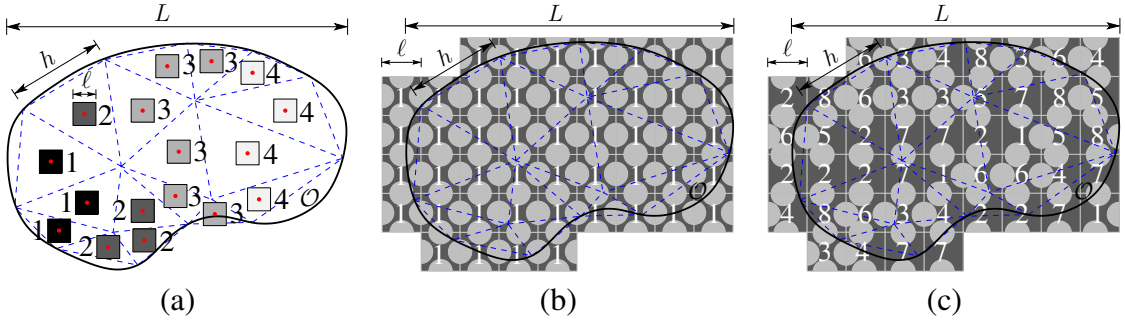

Figure 1: Examples of heterogeneity representations for a macroscopic body $\mathcal{O}$ and (a) separated scales ($\ell \ll h < L$): three unit cells associated with integration points (in red), (b) periodic geometry with non-separated scales ($\ell < h < L$): a single periodic unit cell, (c) aperiodic geometry with non-separated scales ($\ell < h < L$): eight distinct Wang tiles; ℓ, h, and L denote characteristic macroscopic, element (meso-scopic), and heterogeneity lengths, respectively.

1.1. Partition of unity methods

Consider a microstructured two-dimensional domain $\mathcal{O} \subset \mathbb{R}^2$ approximated by finite elements, cf. Fig. 1. The partition of unity methods build on the displacement field approximation in the form

$$\boldsymbol{u}(\boldsymbol{x}) \approx \sum_{n=1}^{n^{\mathrm{n}}} N_n(\boldsymbol{x}) \left[\boldsymbol{a}_n + \boldsymbol{\Psi}^*(\boldsymbol{x})\boldsymbol{b}_n\right] \text{ for } \boldsymbol{x} \in \mathcal{O}, \tag{1}$$

where n^{n} is the number of nodes in the finite element mesh, $N_n : \mathcal{O} \to \mathbb{R}$ denotes the standard finite element basis functions and $\boldsymbol{a}_n \in \mathbb{R}^2$ the regular degrees of freedom associated with the n-th node, whereas $\boldsymbol{\Psi}^*$ and $\boldsymbol{b}_n$ designate the strategy-specific matrices of enrichment functions and extended degrees of freedom, respectively. The ansatz (1) is then employed in the standard Galerkin procedure to arrive at a system of linear(ized) equations involving both regular and extended degrees of freedom. This approach was explored by Fish and

Yuan [11, 12], who derived the enrichment functions from solutions to a periodic unit cell problem, formulated for cells associated with integration points, see Fig. 1(a). In particular,

$$\boldsymbol{\Psi}^*(\boldsymbol{x}) = \begin{bmatrix} u_1^{*(1)} & u_1^{*(2)} & \frac{1}{\sqrt{2}}u_1^{*(3)} \\ u_2^{*(1)} & u_2^{*(2)} & \frac{1}{\sqrt{2}}u_2^{*(3)} \end{bmatrix}(\boldsymbol{x}), \tag{2}$$

where $u_i^{*(j)} : \mathcal{O} \to \mathbb{R}$ denotes the i-th component of the fluctuating displacement field, determined for a unit cell subject to the average strain with the j-th component set to one, while the remaining two vanish (see Appendix A for further details). Such form of enrichment functions is motivated by the displacement decomposition

$$\boldsymbol{u}(\boldsymbol{x}) = \boldsymbol{u}^0(\boldsymbol{x}) + \boldsymbol{u}^*(\boldsymbol{x}) \text{ for } \boldsymbol{x} \in \mathcal{O}, \tag{3}$$

with $\boldsymbol{u}^0 : \mathcal{O} \to \mathbb{R}^2$ and $\boldsymbol{u}^* : \mathcal{O} \to \mathbb{R}^2$ referring to global and fluctuating displacement fields; parameter $\boldsymbol{b}_n \in \mathbb{R}^3$ in Eq. (1) has thus the physical meaning of a generalised average strain known from classical homogenisation theories [15]. Since such fields are constructed under the assumption of separated lenghtscales, Fig. 1(a) with $\ell/L \to 0$, an attention is paid neither to the geometrical compatibility among neighbouring cells, nor to the compatibility of the corresponding enrichment fields. Consistent mathematical results for *periodic media* with a finite ratio ℓ/L, Fig. 1(b), were obtained by Matache et al. [25]. The enrichment functions are constructed on the basis of the spectral version of the unit cell problem [29] resolved by the p-version of the finite element method, see [1] for additional contributions to this field. The partition of unity methods have also been applied to simulations of material systems with *explicitly represented non-periodic* heterogeneities, such as thin fibres [37, 38]. Here, the enrichment function is chosen to be piecewise constant in fibre and matrix domains, and the extended degrees of freedom correspond to a relative slip at the fibre-matrix interface. Such simple format comes at the expense of the fact that two extra degrees of freedom are introduced per fibre, which renders realistic simulations costly.

1.2. Trefftz method

The hybrid Trettfz approach has recently been employed by Novák et al. [32] to simulate composites reinforced with non-periodic ellipsoidal heterogeneities with non-separated lengthscales. The method builds on the additive stress decomposition

$$\boldsymbol{\sigma}(\boldsymbol{x}) = \boldsymbol{\sigma}^0(\boldsymbol{x}) + \boldsymbol{\sigma}^*(\boldsymbol{x}) \text{ for } \boldsymbol{x} \in \mathcal{O}, \tag{4}$$

with $\boldsymbol{\sigma}^0 : \mathcal{O} \to \mathbb{R}^3$ corresponding to the macroscopic stress field and $\boldsymbol{\sigma}^* : \mathcal{O} \to \mathbb{R}^3$ being stress fluctuations, approximated at the level of an element Ω_e as

$$\boldsymbol{\sigma}(\boldsymbol{x}) \approx \boldsymbol{\Sigma}_e(\boldsymbol{x})\boldsymbol{a}_e + \boldsymbol{\Sigma}^*(\boldsymbol{x})\boldsymbol{b}_e \text{ for } \boldsymbol{x} \in \Omega_e. \tag{5}$$

Here, in analogy to Eq. (1), $\boldsymbol{\Sigma}_e : \Omega_e \to \mathbb{R}^{3\times m}$ stands for the standard basis functions of the Trefftz method associated with m regular degrees of freedom $\boldsymbol{a}_e \in R^m$ and $\boldsymbol{b}_e \in \mathbb{R}^3$ denotes the extended degrees of freedom with the physical meaning of average element strains. The

individual enrichment functions

$$\boldsymbol{\Sigma}^*(\boldsymbol{x}) = \begin{bmatrix} \sigma_{11}^{*(1)} & \sigma_{11}^{*(2)} & \sqrt{2}\sigma_{11}^{*(3)} \\ \sigma_{22}^{*(1)} & \sigma_{22}^{*(2)} & \sqrt{2}\sigma_{22}^{*(3)} \\ \sqrt{2}\sigma_{12}^{*(1)} & \sqrt{2}\sigma_{12}^{*(2)} & 2\sigma_{12}^{*(3)} \end{bmatrix} (\boldsymbol{x}) \text{ for } \boldsymbol{x} \in \mathcal{O}, \tag{6}$$

correspond to the fluctuating stress fields due to unitary strain impulses, see again Appendix A for further details. Note that the regular and enrichment basis functions need to be selected such that the stress remains self-equilibrated. The stress approximation is complemented with an independent approximation of displacements at the element boundary Γ_e [18]

$$\boldsymbol{u}(\boldsymbol{x}) \approx \boldsymbol{N}_e^{\Gamma}(\boldsymbol{x})\boldsymbol{a}_e^{\Gamma} \text{ for } \boldsymbol{x} \in \Gamma_e, \tag{7}$$

involving only regular edge shape functions $\boldsymbol{N}_e^{\Gamma}$ and regular boundary degrees of freedom $\boldsymbol{a}_e^{\Gamma}$. The remainder of the formulation follows from the weak form of the equilibrium and compatibility equations, which can be converted to the element boundaries by virtue of the divergence theorem, cf. [18, 41]. The appealing feature of the particular formulation [32] is that the size of the resulting system of equations is the same as for the homogeneous problem, due to the elimination of the extended degrees of freedom. This is achieved by a careful construction of the enrichment functions through Eshelby solutions for individual particles [8, 9], combined together to obtain compatible mechanical fields [32].

1.3. Tiling-based approach

This short overview illustrates the major difficulty in simulating non-periodic systems with realistic geometries, namely that simple enrichment functions lead to the loss of information and/or to a significant increase in the number of degrees of freedom, whereas manageable system sizes necessitate complex constructions of enrichment functions. The aim of this work is thus to develop an algorithm that allows for extending the local (possibly periodic) data from computationally tractable samples to entire macroscopic domains in a non-periodic way, Fig. 1(c). The algorithm keeps the synthesised enrichment functions, $\boldsymbol{\Psi}^*$ in Eq. (1) or $\boldsymbol{\Sigma}^*$ in Eq. (5), continuous across congruent boundaries and consistent in terms of statistical properties of original and reconstructed material morphologies. It is based on a small number of the so-called Wang tiles [44, 16, 4] and a stochastic tiling procedure introduced by Cohen et al. [3].

In 1961, Hao Wang introduced a tiling concept involving square tiles with different codes on their edges, referred to as Wang tiles [44]. The tiles are connected together so that the adjacent edges have the same code and permit a computationally efficient graphic reproduction of morphological patterns [3, 4, 6, 16]. Their desirable aesthetic properties are attributed to the aperiodicity of tilings, whereas the low computational effort results from the use of a small number of tiles to compress the entire morphological information [21].

Here, we exploit and extend these principles to provide a basis for an efficient generation of microstructure-based enrichment functions applicable in partition of unity or hybrid Trefftz finite element algorithms. In order to meet additional criteria arising from such constructions, the Simulated annealing-based optimisation [19, 43] is used to arrive at optimal tile sets. The performance of the method is illustrated on the construction of tile-based stress enrichment functions in a mono-disperse two-phase composite medium with linear elastic

phases. Although the proposed approach is illustrated solely in the two-dimensional setting, it is fully extensible to three dimensions by exploring the results available for the Wang cubes [5, 24]. We also note in passing that the techniques developed in this paper can be used equally well as microstructure reconstruction or generation algorithms, generalising the previous developments available e.g. in [36, 46, 20, 48, 22, 31, 40].

The paper structure is as follows. The concept of stochastic Wang tiling is described in Section 2. A discussion on the optimisation procedure based on prescribed statistical descriptors and compatibility of synthesised mechanical fields on contiguous tile edges is given in Section 3. Section 4 comprises numerical examples demonstrating the performance of the proposed approach. Final remarks on the current developments and future plans are assembled in Section 5. Finally, in Appendix A, we present a brief overview of the stress analysis algorithm utilised to determine the local stress fluctuations.

2. Aperiodic tilings by sets of Wang tiles

Consider again the domain $\mathcal{O}$ from Fig. 1(c) covered by a regular square grid. Each grid cell contains specific microstructural patterns that are compatible on contiguous boundaries. If there are no missing cells inside the synthesised domain, the discretization is called a valid *tiling*[1] and a single cell is referred to as the *Wang tile* [44], Fig. 2. The tiles have different codes on their edges, enumerated here by lowercase Greek letters, and are not allowed to rotate during the tiling procedure. The number of distinct tiles is fixed, though arranged in such a fashion that no sub-sequence of tiles periodically repeats. The set of all distinct tiles is referred to as the *tile set*, Fig. 2(a). Sets that enable uncountably many, always aperiodic, tilings are called *aperiodic* sets [4]. The assumption of strictly aperiodic sets can be relaxed, though still being capable to tile the plane aperiodically, e.g., when utilising the Cohen-Shade-Hiller-Deussen (CSHD) tiling algorithm [3] briefly introduced in the following section. Note that such tilings provide substantial generalisations to periodic paving algorithms, which use identical tiles–periodic unit cells, recall Fig. 1(b).

2.1. Tile set setup

Favourable properties of a tile set to control repetitive effects proceed from the tile and edge code diversity. The number of edge codes n_i^{c} in the i-th spatial direction of the Cartesian coordinates can be chosen arbitrarily, while the number of tiles n^{t} must satisfy

$$n^{\mathrm{t}} = n^{\mathrm{NW}}\sqrt{n^{\mathrm{cs}}}, \tag{8}$$

where $n^{\mathrm{cs}} = (n_1^{\mathrm{c}} n_2^{\mathrm{c}})^2$ is the number of tiles in the complete set and $n^{\mathrm{NW}} = 2, \ldots, \sqrt{n^{\mathrm{cs}}}$ stands for the number of tiles associated with each admissible pair of north-western (NW) edge codes, Fig. 2(a), see [33] for further details.

When designing a tile set, one chooses a particular number of edge codes n_1^{c} and n_2^{c}. The complete set of n^{cs} tiles is created by mutually permuting the codes. In order to tile the plane, the south-eastern edge codes must match those assigned to NW edges, Fig. 2(b). Thus, the created tiles are collected according to NW combinations. Finally, a desired number of tiles

[1] Henceforth, the term "tiling" stands for "valid tiling" exclusively, thereby excluding invalid tilings from the consideration.

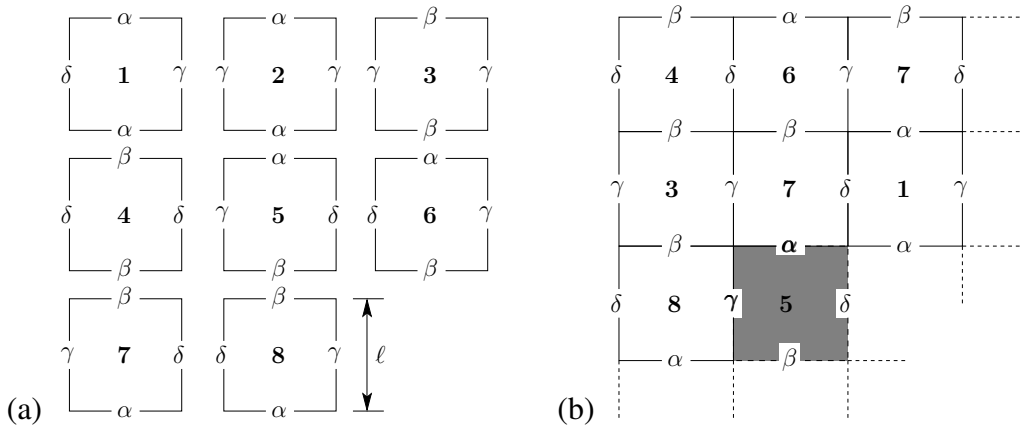

Figure 2: (a) Tile set W8/2-2 [3] consisting of 8 tiles with 2 vertical $\{\alpha, \gamma\}$ and 2 horizontal $\{\beta, \delta\}$ edge codes with equal frequencies of occurrence $q_\alpha = q_\beta = q_\gamma = q_\delta = \frac{1}{4}$, and $n^{\mathrm{NW}} = 2$, (b) an example of aperiodic valid tiling with highlighted connectivity across south-eastern and north-western edges.

is chosen using Eq. (8), in such a way that n^{NW} unique tiles is selected from each NW group. The emerging, user-defined, set of tiles is referred to as W$n^{\mathrm{t}}/n_1^{\mathrm{c}}$–$n_2^{\mathrm{c}}$. Moreover, we denote the relative frequency of occurrence of the c-th code in the tile set by q_c, see Fig. 2(a).

2.2. CSHD stochastic tiling algorithm

Since there are n^{NW} tiles associated to each NW group, index of the new tile to be placed is selected randomly from the set $\{1, \ldots, n^{\mathrm{NW}}\}$ with the uniform probability. Beforehand, one must select an appropriate NW group compatible with the eastern code of a previously placed tile and the southern code of the tile just above the one to be placed (edges α and γ of shaded areas in Fig. 2(b)). Aperiodicity of the resulting tiling is guaranteed by assuming that the random generator never returns a periodic sequence of numbers and that each NW group contains at least two distinct tiles [3].

3. Designing optimal tile set morphology

To simplify the exposition, we limit our attention to two-phase composite media formed by a matrix phase and equi-sized disks of radius ρ and a parametric microstructure representation built on the Wang tile set W8/2–2[2], introduced in Section 3.1. The location of the disks within the tiles has to be optimised to achieve (i) good approximation of the original microstructure in terms of a given morphological descriptor, Section 3.2, and (ii) microstructures that guarantee the compatibility of enrichment functions on contiguous tile edges, Section 3.3. Such criteria originate from different perspectives. The first goal aims at capturing the dominant spatial features of original media, while the latter criterion ensures that the tiling-generated fields comply with the governing differential equations. The details of the algorithm used to solve the resulting optimisation problem are provided in Section 3.4.

[2]The set W8/2–2 has been chosen since it is the simplest one that allows for aperiodic patterns in the stochastic sense [3]. Note that all the steps of the tile set design can be directly generalised to more complex tile sets, cf. [33].

3.1. Microstructure parametrisation

The adopted bitmap-based microstructure representation involves a Wang tile set consisting of n^{t} tiles of the edge length $\ell \in \mathbb{N}$ (in pixels), in which we distribute n^{d} disks of radius ρ. The d-th disk is represented by a triplet $\{t_d, x_{1,d}, x_{2,d}\}$, where $t_d \in \{1, \ldots, n^{\mathrm{t}}\}$ denotes the tile index and $x_{d,j} \in \{1, \ldots, \ell\}$ specifies the position of the d-th disk within the tile at the j-th direction. The associated parameter vector $\boldsymbol{p}$ is obtained as a collection of these data:

$$\boldsymbol{p} = [t_d, x_{1,d}, x_{2,d}]_{d=1}^{n^{\mathrm{d}}} . \tag{9}$$

Since the position of each disk is specified by three parameters, the parameter space $\mathbb{P}$ is $(3 \times n^{\mathrm{d}})$-dimensional, i.e. $\mathbb{P} \subset \mathbb{N}^{3 \times n^{\mathrm{d}}}$.

In an admissible configuration, the disks do not penetrate each other or overlap corners of tiles being associated with. The first constraint reflects the given feature of the original microstructure, Fig. 3(a), whereas the latter one arises as an artifact intrinsic to the edge-based tiling algorithm, e.g., [3]. In addition, to maintain the morphological compatibility, any disk intersecting the edge of a given code needs also be associated to tiles containing the same edge. To emphasise this, we encode a particular microstructural configuration as $n^{\mathrm{d}}\{n_c^{\mathrm{d}}\}_{c=1}^{n^{\mathrm{c}}}$, where n_c^{d} denotes the number of disks intersecting the edge of code c, see Fig. 6 on page 11.

3.2. Statistical properties of the microstructure

The most common class of statistical descriptors embodies a set of n-point probability functions, applicable to generic heterogeneous media [42]. In this paper, the focus is on the two-point probability function, which captures primary phenomena as the phase volume fraction, characteristic microstructural length(s), and long-range orientation orders, if any.

We now assume that the domain $\mathcal{O}$ is occupied by a two-phase heterogeneous material discretized by a regular lattice of $n_1^{\mathcal{O}} \times n_2^{\mathcal{O}}$ pixels, indexed by $\boldsymbol{k} \in \mathbb{K}^{\mathcal{O}}$ with

$$\mathbb{K}^{\mathcal{O}} = \left\{ \boldsymbol{m} \in \mathbb{Z}^2 : -\frac{n_i^{\mathcal{O}}}{2} < m_i \leq \frac{n_i^{\mathcal{O}}}{2}, i = 1, 2 \right\} . \tag{10}$$

The distribution of individual phases (disks and matrix) within $\mathcal{O}$ is quantified by the characteristic function $\chi(\boldsymbol{k})$, which equals 1 when $\boldsymbol{k}$ is occupied by the disk phase and 0 otherwise, cf. Fig. 3(a). Assuming a periodic[3] ergodic medium, the two-point probability function $S_2 : \mathbb{K}^{\mathcal{O}} \to [0, 1]$ is then defined as [42]

$$S_2(\boldsymbol{k}) = \frac{1}{n_1^{\mathcal{O}} n_2^{\mathcal{O}}} \sum_{\boldsymbol{m} \in \mathbb{K}^{\mathcal{O}}} \chi(\boldsymbol{m}) \chi\left(\lfloor \boldsymbol{k} + \boldsymbol{m} \rfloor_{\mathbb{K}^{\mathcal{O}}} \right) , \tag{11}$$

where $\lfloor \bullet \rfloor_{\mathbb{K}^{\mathcal{O}}}$ denotes the $\mathbb{K}^{\mathcal{O}}$-periodic extension. Noticing that (11) has the structure of circular correlation, the two-point probability function can be efficiently evaluated using Fast Fourier Transform techniques, see e.g. [14].

[3]Note that periodicity is considered here for the sake of computational efficiency. The tiling-generated data is always aperiodic.

According to its definition, $S_2(\boldsymbol{k})$ quantifies the probability that two arbitrary points separated by $\boldsymbol{k}$ will both be located at the disk phase when randomly selected from $\mathbb{K}^{\mathcal{O}}$. Denoting by ϕ the disk volume fraction, $0 \leq \phi \leq 1$, the two-point probability function satisfies $S_2(\mathbf{0}) = \phi$. Moreover, $S_2(\boldsymbol{k}) \simeq \phi^2$ for $\|\boldsymbol{k}\| \gg \rho$ indicates that the medium does not exhibit repeating long-range order orientation effects, cf. Fig. 3(b).

(a) 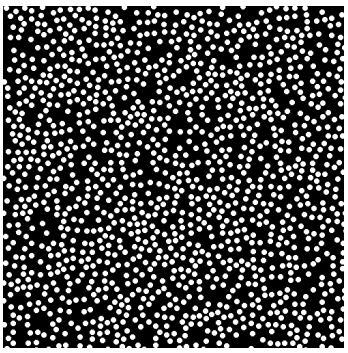 (b) 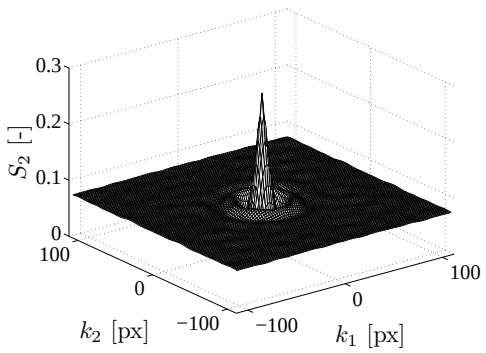

Figure 3: (a) An example of two-phase medium formed by equilibrium distribution of $1,300$ equi-sized disks of volume fraction 26.8% and (b) the two-point probability function S_2; the sample is discretized with $1,000 \times 1,000$ pixels and each disk has the radius of 8 pixels.

The following procedure is adopted to determine the two-point probability function for the tile-based microstructure. First, the set W8/2–2 is used to assemble a 4×4 tiling $\mathcal{O}_{\mathrm{S}} \subset \mathbb{R}^2$, periodic on external boundaries, in which each tile appears with the same frequency in order to suppress artificial fluctuations in volume fractions, Fig. 4(a). The domain $\mathcal{O}_{\mathrm{S}}$ is discretized by an $n_1^{\mathcal{O}_{\mathrm{S}}} \times n_2^{\mathcal{O}_{\mathrm{S}}}$ regular grid with the same pixel size as in the original microstructure, so that $n_i^{\mathcal{O}_{\mathrm{S}}} < n_i^{\mathcal{O}}$. Given a parameter vector $\boldsymbol{p}$ quantifying positions of individual disks, the tile-based morphology is quantified by the two-point probability function $\widetilde{S}_2 : \mathbb{P} \times \mathbb{K}^{\mathcal{O}_{\mathrm{S}}} \to [0,1]$, and its proximity to the target microstructure is evaluated as

$$f^{\mathrm{S}}(\boldsymbol{p}) = \frac{1}{n_1^{\mathcal{O}_{\mathrm{S}}} n_2^{\mathcal{O}_{\mathrm{S}}}} \sum_{\boldsymbol{k} \in \mathbb{K}^{\mathcal{O}_{\mathrm{S}}}} \Big(S_2(\boldsymbol{k}) - \widetilde{S}_2(\boldsymbol{p}, \boldsymbol{k}) \Big)^2 , \tag{12}$$

where $\mathbb{K}^{\mathcal{O}_{\mathrm{S}}}$ is defined analogously as for the target medium $\mathcal{O}$.

3	4	1	6
5	7	2	8
2	1	4	7
8	6	3	5

(a) Tiling $\mathcal{O}_{\mathrm{S}}$

2	**1**	**6**	**3**	**4**	**8**	3	6	4
2	8	6	3	3	**5**	**7**	8	5
6	5	2	7	7	2	1	5	8
2	2	2	7	1	6	6	4	7
4	8	6	3	4	2	2	7	1
3	3	4	7	7	2	8	5	8
1	5	7	1	3	4	1	6	5
8	6	5	8	5	1	4	8	4
1	4	2	7	2	2	7	1	5

(b) Tiling $\mathcal{O}_{\mathrm{T}}$

Figure 4: Valid tilings used in optimisation with respect to (a) two-point probability function and (b) stress field; highlighted vertical edges in (b) correspond to edge set Γ_δ containing 50 equivalent edges of code δ and length ℓ. Tiles denoted by bold numbers (first two rows) are used to generate aperiodic enrichment functions.

3.3. Stress-based enrichment fields and their compatibility

The additional, yet more complex, goal is to find the tile set morphology that ensures the admissibility of enrichment functions synthesised by the tiling algorithm. Analogously to the original Wang idea, this is achieved by requiring that edges of identical codes carry identical, this time non-scalar, information. In particular, motivated by encouraging results obtained recently in [32], we concentrate on the stress enrichment functions $\boldsymbol{\Sigma}^*$, recall Eq. (6). It is natural convert them to equivalent traction fluctuations, obtained as

$$\boldsymbol{T}^* = \boldsymbol{\nu}\boldsymbol{\Sigma}^*, \tag{13}$$

where $\boldsymbol{T}^*$ collects the components associated with individual load-cases and $\boldsymbol{\nu}$ stores the components of the normal vector:

$$\boldsymbol{T}^* = \begin{bmatrix} T_1^{*(1)} & T_1^{*(2)} & T_1^{*(3)} \\ T_2^{*(1)} & T_2^{*(2)} & T_2^{*(3)} \end{bmatrix}, \qquad \boldsymbol{\nu} = \begin{bmatrix} \nu_1 & 0 & \frac{1}{\sqrt{2}}\nu_2 \\ 0 & \nu_2 & \frac{1}{\sqrt{2}}\nu_1 \end{bmatrix}.$$

Analogously to the morphology design, the definition of the traction-based objective function is based on an auxiliary 9×9 tiling $\mathcal{O}_{\mathrm{T}}$, Fig. 4(b), discretized into $n_1^{\mathcal{O}_{\mathrm{T}}} \times n_2^{\mathcal{O}_{\mathrm{T}}}$ bitmap with pixels indexed by $\boldsymbol{k} \in \mathbb{K}^{\mathcal{O}_{\mathrm{T}}}$. The tiling is periodic at external boundaries, and contains all admissible combinations of tile pairs from the set W8/2–2 sharing all edge codes[4], since we assume that the edge traction values are dominated by the response of adjacent tiles. Hence, for each edge code $c \in \{1, 2, \ldots, n^{\mathrm{c}}\}$ with $n^{\mathrm{c}} = n_1^{\mathrm{c}} + n_2^{\mathrm{c}}$, we introduce a set Γ_c formed by n^{Γ_c} edges of identical code c and length ℓ with normal vector $\boldsymbol{\nu}^{\Gamma_c}$, Fig. 4(b)[5]. By $\boldsymbol{\Gamma}_{c,j} : \{1, \ldots, \ell\} \to \mathbb{K}^{\mathcal{O}_{\mathrm{T}}}$, $j \in \{1, 2, \ldots, n^{\Gamma_c}\}$, we denote a function providing coordinates of individual pixels at the j-th edge of code c.

Now we are in a position to quantify differences of tractions carried by an edge code c, due to differing neighbours, via an objective function f_c^{T}. For a given parameter vector $\boldsymbol{p} \in \mathbb{P}$ and material properties of individual phases, we calculate the stress enrichment function $\boldsymbol{\Sigma}^*(\boldsymbol{p}, \boldsymbol{k})$ by the algorithm outlined in Appendix A, and evaluate the objective function as

$$f_c^{\mathrm{T}}(\boldsymbol{p}) = \frac{1}{\ell}\sum_{s=1}^{\ell} \left\| \max\left\{\boldsymbol{T}^*(\boldsymbol{p}, \boldsymbol{\Gamma}_{c,j}(s))\right\}_{j=1}^{n^{\Gamma_c}} - \min\left\{\boldsymbol{T}^*(\boldsymbol{p}, \boldsymbol{\Gamma}_{c,j}(s))\right\}_{j=1}^{n^{\Gamma_c}} \right\|_1, \tag{14}$$

where the traction enrichments are determined from Eq. (13) with $\boldsymbol{\nu} = \boldsymbol{\nu}^{\Gamma_c}$, $\max$ and $\min$ operations are understood component-wise and $\|\boldsymbol{A}\|_1 = \sum_{i,j} |A_{ij}|$. Collecting the contributions from all codes, we obtain

$$f^{\mathrm{T}}(\boldsymbol{p}) = \sum_{c=1}^{n^{\mathrm{c}}} f_c^{\mathrm{T}}(\boldsymbol{p}). \tag{15}$$

Once the tile set is designed with respect to the objective function (15), the tiling-based

[4]There are 16 distinct pair combinations of basic tiles sharing the code δ : $\{2-1, 2-2, 2-7, 2-8, 4-1, 4-2, 4-7, 4-8, 5-1, 5-2, 5-7, 5-8, 7-1, 7-2, 7-7, 7-8\}$ see Fig. 2(a). All these combinations are present in the tiling $\mathcal{O}_{\mathrm{T}}$ in Fig. 4(b), each of them multiple times.

[5]For the particular tile set considered here, we set $\boldsymbol{\nu}^{\Gamma_\alpha} = \boldsymbol{\nu}^{\Gamma_\gamma} = [0, 1]$ and $\boldsymbol{\nu}^{\Gamma_\beta} = \boldsymbol{\nu}^{\Gamma_\delta} = [1, 0]$.

stress enrichment functions $\widetilde{\boldsymbol{\Sigma}}^* : \mathbb{K}^{\mathcal{O}_\mathrm{T}} \to \mathbb{R}^{3\times 3}$ can be assembled by the CSHD algorithm using the stress fluctuations $\boldsymbol{\Sigma}^*$ carried by an arbitrary selection of tiles 1–8 from the tiling $\mathcal{O}_\mathrm{T}$. In the numerical experiments reported in Section 4, we use the set of eight tiles from the top rows of $\mathcal{O}_\mathrm{T}$ highlighted by bold numbers in Fig. 4(b), but equivalent results were obtained for different selections. Due to this procedure, the reconstructed edge tractions corresponding to the synthesised enrichments $\widetilde{\boldsymbol{\Sigma}}^*$ may experience jumps at tile edges. For the j-th edge of the set Γ_c, these are defined as

$$[\widetilde{\boldsymbol{T}}^*_{c,j}](s) = \boldsymbol{\nu}^{\Gamma_c}\left(\widetilde{\boldsymbol{\Sigma}}^*_+(\boldsymbol{\Gamma}_{c,j}) - \widetilde{\boldsymbol{\Sigma}}^*_-(\boldsymbol{\Gamma}_{c,j})\right) \text{ for } s \in \{1,2,\ldots,\ell\}, \tag{16}$$

where $\widetilde{\boldsymbol{\Sigma}}^*_+$ and $\widetilde{\boldsymbol{\Sigma}}^*_-$ denote the values of the stress enrichment functions taken from the nearest edge neighbours from right and left, respectively, relative to the orientation of the edge set Γ_c by the normal vector $\boldsymbol{\nu}^{\Gamma_c}$.

3.4. Optimisation procedure

In fact, the goals represented by objective functions (12) and (15) are conflicting. Minimising only with respect to the two-point probability function results in traction enrichments discontinuous at internal edges, whereas the latter criterion drives the system to a periodic distribution of disks. To achieve a compromise solution, we introduce a composite objective function in the form

$$f(\boldsymbol{p}) = w f^\mathrm{S}(\boldsymbol{p}) + f^\mathrm{T}(\boldsymbol{p}), \tag{17}$$

where w denotes a weighting factor balancing geometrical features with mechanical compatibility. The minimisation of the objective function (17) is performed by the well-established Simulated Annealing method [19, 43], extended by a re-annealing phase to escape from local extremes, e.g. [23].

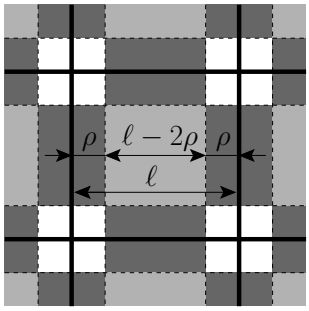

Figure 5: Tile decomposition into interiors, edges and corner regions.

Given the number of disks n^d and the target volume fraction ϕ, we initiate the algorithm by determining the number of edge disks n^d_c related to the c-th code and the tile edge length ℓ. Although this problem is difficult due to multiplicity of the edge-related disks, recall Fig. 6, we resolved it by a heuristic procedure outlined next. To this purpose, an arbitrary tile is decomposed into three regions assigned to interiors (light grey area in Fig. 5), edges (dark grey area in Fig. 5), and to corners (white area in Fig. 5 that cannot be occupied by disks due to the corner constraint). For a disk configuration $n^\mathrm{d}\{n^\mathrm{d}_c\}_{c=1}^{n^\mathrm{c}}$ related to a tile set Wn^t/n^c_1–n^c_2, there is $(n^\mathrm{d} - \sum_{c=1}^{n^\mathrm{c}} n^\mathrm{d}_c)$ interior disks and, due to the edge constraints, a single disk

associated with code c appears $2n^{\mathrm{t}}q_c$ times, cf. Fig. 6. Thus, the disk volume fraction in the tile set or in a tiling is given by

$$\widetilde{\phi} \approx \frac{A^{\mathrm{d}}}{n^{\mathrm{t}}\ell^2}\left(n^{\mathrm{d}} + \sum_{c=1}^{n^{\mathrm{c}}}\left(2n^{\mathrm{t}}q_c - 1\right)n_c^{\mathrm{d}}\right), \tag{18}$$

with A^{d} denoting the area of a single disk (in square pixels), and should be as close to the target value ϕ as possible. In addition, we impose the condition

$$\frac{n^{\mathrm{d}} - \sum_{c=1}^{n^{\mathrm{c}}} n_c^{\mathrm{d}}}{(\ell - 2\rho)^2} \approx \frac{n^{\mathrm{t}}\sum_{c=1}^{n^{\mathrm{c}}} q_c n_c^{\mathrm{d}}}{2\rho(\ell - \rho)}, \tag{19}$$

matching the local volume fractions of disks in interior and edge regions. Thus, given the numbers of disks attached to codes $\{n_c^{\mathrm{d}}\}_{c=1}^{n^{\mathrm{c}}}$, Eqs. (18) and (19) implicitly define tile edge lengths $\tilde{\ell}$ and $\hat{\ell}$, which should be equal to each other for the correct tile set setup. In our case, we sequentially check all values $\{n_c^{\mathrm{d}}\}_{c=1}^{n^{\mathrm{c}}}$ such that $n_c^{\mathrm{d}} \geq 0$, $\sum_{c=1}^{n^{\mathrm{c}}} n_c^{\mathrm{d}} \leq n^{\mathrm{d}}$ and select the configuration with the minimum difference $|\tilde{\ell} - \hat{\ell}|$.[6]

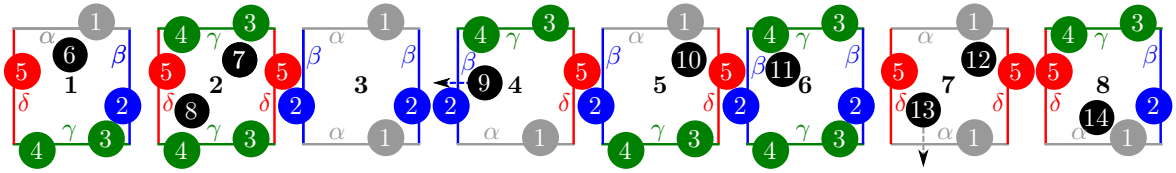

Figure 6: An example of an admissible 14{1-1-2-1} configuration (with $n_\alpha^{\mathrm{d}} = n_\gamma^{\mathrm{d}} = n_\delta^{\mathrm{d}} = 1$ and $n_\beta^{\mathrm{d}} = 2$ code-related disks) and its modification by disk displacements; disk 9 leaves its parent tile 4 and randomly enters tiles 1, 3, 6 or 8; disk 13 leaves its parent tile 7 and randomly enters tiles 1, 3, 5 or 7.

On the basis of these data, we randomly generate positions of individual disks and assign them to randomly selected tile interiors and edges, until an admissible configuration $\boldsymbol{p}$ is obtained. A single loop of the optimisation algorithm involves a sequential selection of a disk $d \in \{1, \ldots, n^{\mathrm{d}}\}$, and its movement given by

$$\widehat{x}_{j,d} = x_{j,d} + \ell\left(U - \tfrac{1}{2}\right), \qquad j = 1, 2, \tag{20}$$

repeated until a new admissible configuration $\widehat{\boldsymbol{p}}$ is encountered. The symbol U denotes a random variable with a uniform distribution in the interval $[0, 1]$. If a disk, during its displacement, leaves its parent tile by crossing the edge of code c, it is randomly assigned to a tile sharing the same code, Fig. 6.

The acceptance of the new solution $\widehat{\boldsymbol{p}}$ is driven by the Metropolis criterion [19]

$$\exp\left(\frac{f(\boldsymbol{p}) - f(\widehat{\boldsymbol{p}})}{\theta}\right) \geq U, \tag{21}$$

where θ denotes the algorithmic temperature, initially set to $\theta^{\max}$ and gradually reduced by

[6]Note that the values of ℓ and n^{d} are kept constant during the optimisation process, whereas the values of n_c^{d} are allowed to change, since disks can move freely between tile interiors and edges.

a constant multiplicator $\theta^{\mathrm{mlt}} < 1$ once the loop over all n^{d} disks is completed. The entire algorithm terminates after $n^{\max}$ objective function evaluations. Moreover, we keep it restarting when the current temperature θ is less than the threshold value $\theta^{\min}$. Such a re-annealing step was found beneficial, as the resulting problem is multi-modal and discontinuous due to the presence of edge-constrained disks.

4. Results

The potential of the tile-based representation is demonstrated for the two-phase composite medium appearing in Fig. 3, with default parameters shown in Tab. 1. Distinct sets W8/2–2, differing in (i) the tile edge length ℓ, (ii) the number of total and edge disks $n^{\mathrm{d}}\{n_c^{\mathrm{d}}\}_{c=1}^{n^{\mathrm{c}}}$, (iii) the weighting factor w, and in (iv) phase properties contrast $E^{\mathrm{d}}/E^{\mathrm{m}}$ have been examined. In particular, our aim is to demonstrate that the proposed tile morphology design procedure works well and that the tile sets based on the specific tilings $\mathcal{O}_{\mathrm{S}}$ and $\mathcal{O}_{\mathrm{T}}$ can be used to represent generic particulate media.

Table 1: Default setting of parameters.

Microstructure	
Volume fraction, ϕ	26.8%
Disk radius, ρ	8 pixels
Young modulus of disk[a], E^{d}	10
Young modulus of matrix[a], E^{m}	1
Poisson ratio of matrix and disks, $\nu^{\mathrm{m}} = \nu^{\mathrm{d}}$	0.125
Optimisation algorithm	
Weighting factor[b], w	10^5
Maximum temperature, $\theta^{\max}$	10^{-3}
Minimum temperature, $\theta^{\min}$	10^{-6}
Multiplicative factor, θ^{mlt}	$(\theta^{\max}/\theta^{\min})^{1/200}$
Number of function evaluations, $n^{\max}$	$10^4 n^{\mathrm{d}}$

[a] In what follows, all stress-related values are expressed in consistent units.

[b] Determined as $w \approx \langle f^{\mathrm{T}}\rangle/\langle f^{\mathrm{S}}\rangle$, with e.g. $\langle f^{\mathrm{S}}\rangle$ denoting the average value of f^{S} determined for 20 randomly generated disk configurations.

In Fig. 8, we present the disk configurations and two-point probability functions $\widetilde{S}_2$ obtained for the domain $\mathcal{O}$ being tiled by optimised tile sets. We observe that all reconstructed functions $\widetilde{S}_2$ exhibit local peaks exceeding the value of ϕ^2, which reveals the presence of characteristic length scales of order ℓ in the synthesised medium. For the default value of the weighting factor $w = 10^5$, Figs. 8(a,b), the local extremes are notably smaller than the value of ϕ corresponding to a periodic construction, e.g. [48]. In addition, their number and magnitude can be substantially reduced by increasing the edge length ℓ, Fig. 8(b), and practically eliminated when using more general tile sets [33]. For lower values of w, the disk distribution becomes more regular, Fig. 8(c), and the resulting representation is visually indistinguishable from the periodic setting, cf. [33].

Such conclusions are further supported by Fig. 9 showing cross-sections of the two-point probability functions in the k_1 direction for two different values of the weighting factor

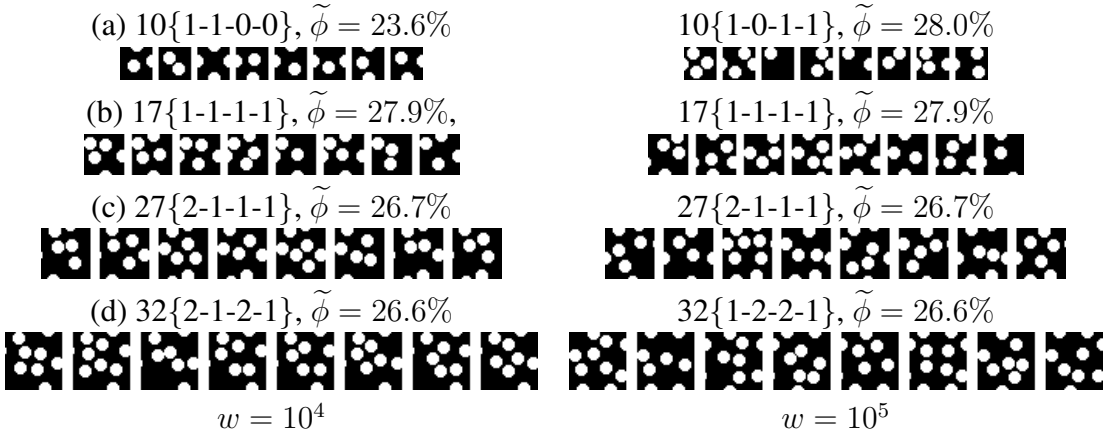

Figure 7: Optimised sets W8/2–2 obtained for weighting factors w equal to 10^4 and 10^5 and for configurations with (a) $n^{\mathrm{d}} = 10$, $\ell = 42$ px, (b) $n^{\mathrm{d}} = 17$, $\ell = 52$ px, (c) $n^{\mathrm{d}} = 27$, $\ell = 64$ px and (d) $n^{\mathrm{d}} = 38$, $\ell = 74$ px; $n^{\mathrm{d}}\{n_c^{\mathrm{d}}\}_{c=1}^{n^{\mathrm{c}}}$ refers to configuration of n^{d} disks in total with n_c^{d} disks intersecting edge c, ℓ is the tile edge length and $\widetilde{\phi}$ is the reconstructed volume fraction.

w. The results demonstrate that for higher values of w, the short-range phenomena are captured to a high accuracy and the magnitude of local extremes are consistently reduced with the increasing number of disks, albeit at a small rate. By decreasing the emphasis on S_2 objective, Fig. 9(b), the discrepancy between the original and reconstructed medium substantially increases at short distances, leading even to an inconsistent value of the volume fraction for 10 disks. The local peaks also become more pronounced as the stress-based criterion drives the system towards periodic configurations.

Fig. 10(a) illustrates the ability of the optimisation algorithm to achieve self-equlibrated stress enrichment functions by comparing the distribution of tractions $T_1^{*(3)}$ obtained for an initial and the optimised configuration of disks. Clearly, traction enrichments at contiguous edges differ significantly in the initial configuration, and are reduced to almost identical values by the proposed procedure. This also automatically keeps the edge jumps in reconstructed traction enrichments $[\widetilde{T}_1^{*(3)}]$ under control, Fig. 10(b), since their magnitude corresponds to the scatter found for representative eight tiles from $\mathcal{O}_{\mathrm{T}}$ utilised in the reconstruction, recall Fig. 4(b).

To what extent influences such choice of representative tiles the synthesised enrichment functions? To address this question, we consider a particular reconstruction of stress enrichments functions $\widetilde{\boldsymbol{\Sigma}}^* : \mathcal{O}_{\mathrm{T}} \to \mathbb{R}^{3\times 3}$, assembled according to the the sequence of tiles found in the tiling $\mathcal{O}_{\mathrm{T}}$. It is useful for the visualisation purposes to introduce a local error measure

$$f_{ij}^{\Sigma}(\boldsymbol{k}) = \frac{\left|\Sigma_{ij}^*(\boldsymbol{k}) - \widetilde{\Sigma}_{ij}^*(\boldsymbol{k})\right|}{\max\limits_{\boldsymbol{m}\in\mathbb{K}^{\mathcal{O}_{\mathrm{T}}}} \Sigma_{ij}^*(\boldsymbol{m}) - \min\limits_{\boldsymbol{m}\in\mathbb{K}^{\mathcal{O}_{\mathrm{T}}}} \Sigma_{ij}^*(\boldsymbol{m})}, \qquad \boldsymbol{k} \in \mathbb{K}^{\mathcal{O}_{\mathrm{T}}}; i,j \in \{1,2,3\}, \tag{22}$$

quantifying a difference between the components of the stress enrichment functions $\boldsymbol{\Sigma}^*$ determined directly for the tiling $\mathcal{O}_{\mathrm{T}}$ by the algorithm described in Appendix A, and their reconstruction $\widetilde{\boldsymbol{\Sigma}}^*$.

Outcomes of this comparison are shown in Fig. 11 in the form of (a) tiling-based microstructures, (b) distribution of the corresponding enrichment functions Σ_{13}^*, (c) their recon-

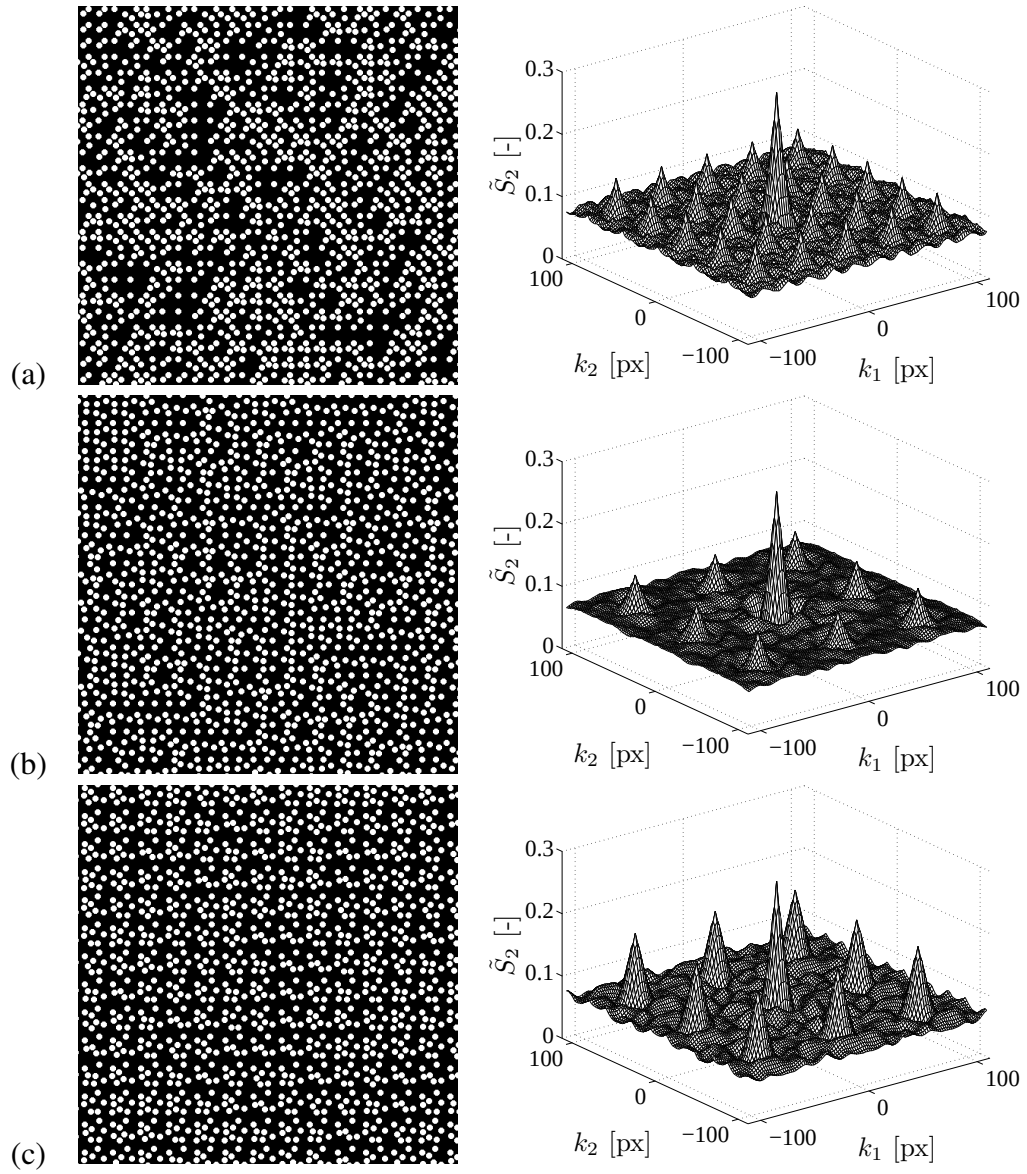

Figure 8: Reconstructed microstructures and two point probability functions $\widetilde{S}_2$ for tile sets with (a) $w = 10^5, n^{\mathrm{d}} = 10$ disks and $\ell = 42$ px, (b) $w = 10^5, n^{\mathrm{d}} = 38$ disks and $\ell = 74$ px, and (c) $w = 10^4, n^{\mathrm{d}} = 38$ disks and $\ell = 74$ px.

structed counterparts and (d) spatial distribution of the relative error. For the microstructure generated from tiles with $n^{\mathrm{d}} = 10$ disks, we observe that the reconstructed field displays distributed errors in tile interiors. Similarly to S_2 criterion, these deviations are significantly reduced and become highly localised when increasing the number of disks and the size of tiles. This claim is further supported by Fig. 12, plotting the evolution of the global error

$$f^{\Sigma} = \frac{1}{\mathcal{O}_{\mathrm{T}}} \sum_{i,j=1}^{3} \sum_{\boldsymbol{k} \in \mathbb{K}^{\mathcal{O}_{\mathrm{T}}}} |f_{ij}^{\Sigma}(\boldsymbol{k})| \tag{23}$$

as a function of the number of disks. For both values of w, we observe approximately linear convergence with increasing n^{d}. In addition, the error decreases for larger phase contrasts

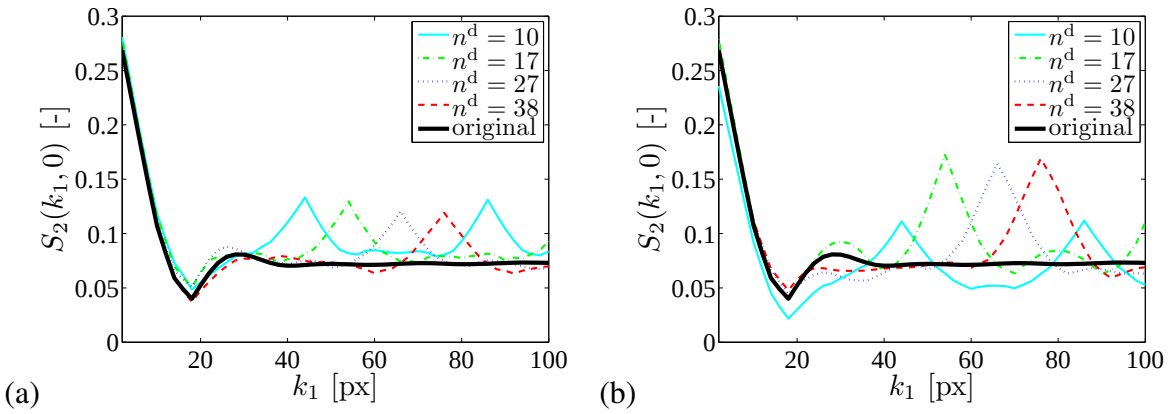

Figure 9: Comparison of two-point probability functions $S_2(k_1, 0)$ for the weighting factors (a) $w = 10^5$ and (b) $w = 10^4$.

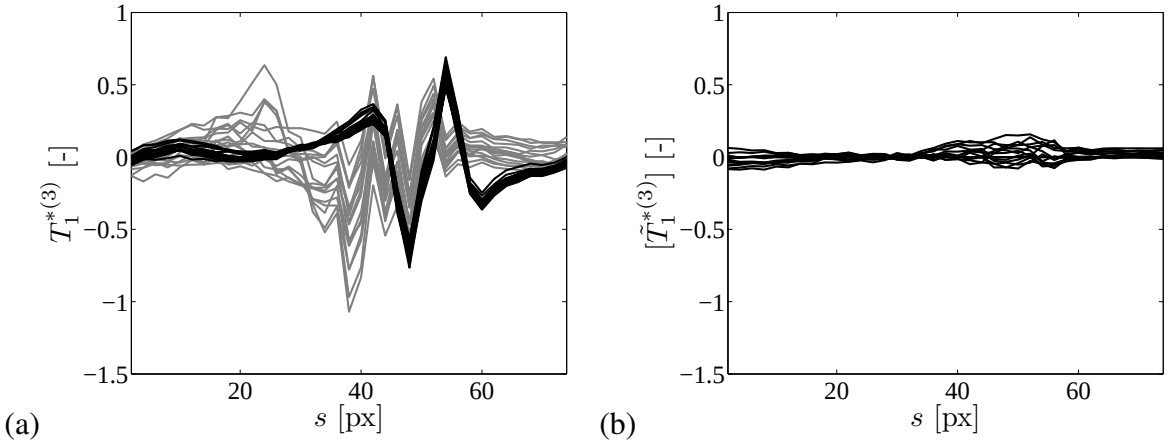

Figure 10: Distribution of (a) traction enrichments $T_1^{*(3)}$ and (b) reconstructed traction enrichment jumps $[\widetilde{T}_1^{*(3)}]$ at edges Γ_δ of the tiling $\mathcal{O}_{\mathrm{T}}$, obtained for $n^{\mathrm{d}} = 38$ disks and $\ell = 74$ px. The grey/black patterns in (a) correspond to initial and optimised and enrichment functions, respectively.

$E^{\mathrm{d}}/E^{\mathrm{m}}$. This is caused by the fact that stresses tend to concentrate more at stiffer disks, therefore reducing variations of tractions at tile edges, see also [32] for a similar discussion.

Altogether, this indicates that the tile set was designed correctly, since the optimisation was executed for independent objective functions, recall Eq. (17). Finally we stress that the significant compression has been achieved by the tiling-based representation: the original microstructure contains $\approx 1,300$ disks, whereas the most detailed tile-based representation builds on 38 disks only and is capable of producing much larger microstructures at a negligible computational cost.

5. Conclusions

In this work, we have proposed an approach to the construction of aperiodic local fields in heterogeneous media with potential applications in hybrid or generalised FE environments. The method is based on the Wang tiling concept that allows us to represent complex patterns using a limited set of representative tiles, complemented by the Simulated Annealing-based algorithm to arrive at optimal tile set morphologies. On the basis of the results obtained from analyses of the medium under consideration we conjecture that:

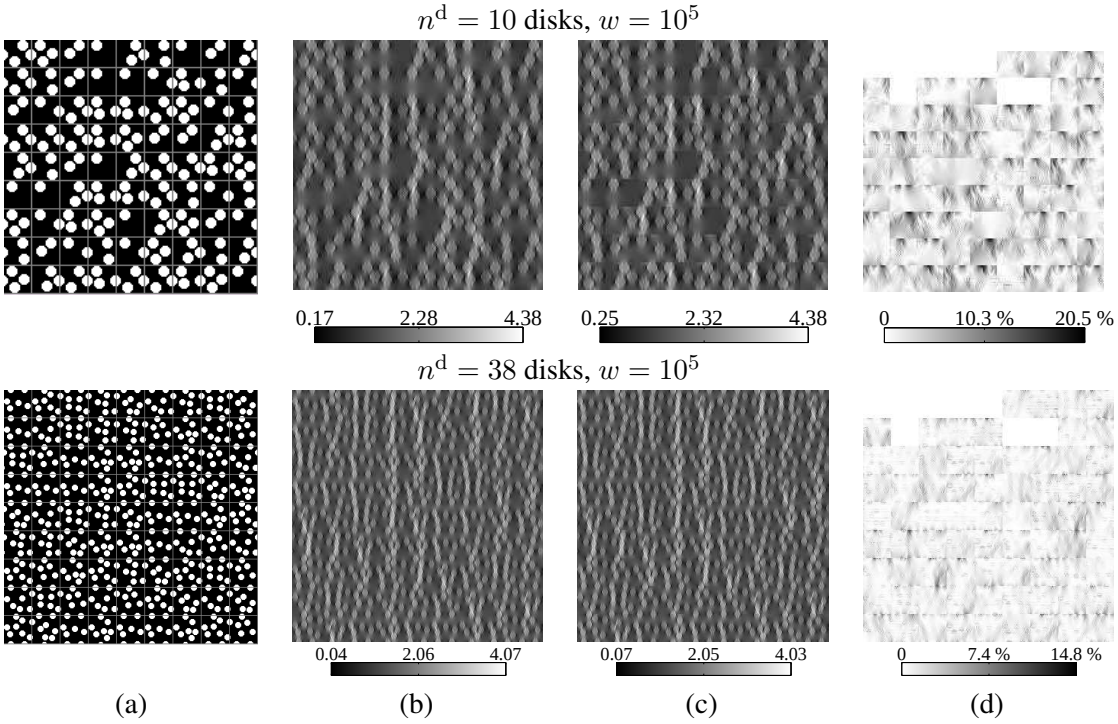

Figure 11: Assessment of tiling-based enrichment functions, (a) microstructures obtained by tilings $\mathcal{O}_{\mathrm{T}}$, distribution of (b) true stress enrichment functions $\Sigma^*_{13} \equiv \sigma^{*(3)}_{11}$, (c) reconstructed stress enrichment functions $\widetilde{\Sigma}^*_{13} \equiv \widetilde{\sigma}^{*(3)}_{11}$ and of (d) the local reconstruction-based error f^{Σ}_{13}.

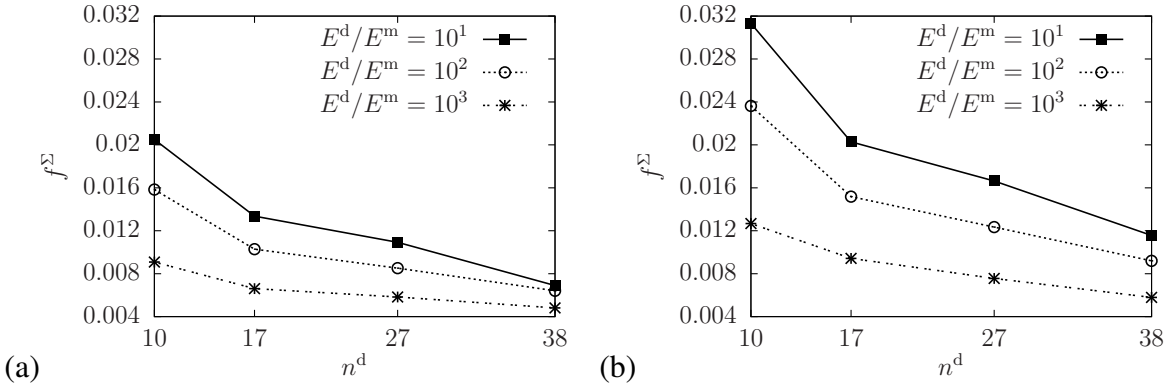

Figure 12: The global reconstruction error f^{Σ} as a function of the number of disks n^{d} for different phase contrasts $E^{\mathrm{d}}/E^{\mathrm{m}}$ and weighting factors (a) $w = 10^5$ and (b) $w = 10^4$.

- the proposed method provides a robust tool for compression of disordered microstructures and can serve as an efficient microstructure generation algorithm,
- it allows for aperiodic extensions of local, possibly periodic, fields to substantially larger domains while maintaining their compatibility,
- the tiling-based fields can be utilised as microstructure-based enrichment functions for generalised Partition of Unity methods or hybrid finite element schemes.

We are fully aware that our conclusions are somewhat provisional, in the sense that these are based on a single set of tiles and the specific class of microstructures. Partial extension to

general setting is available in [33, 7] and remains in the focus of our current work.

Acknowledgements

The authors thank Jaroslav Vondřejc (CTU in Prague) for providing us with a MATLAB source code of FFT-based homogenisation algorithm and Adrian Russell (University of New South Wales), Michal Šejnoha and Milan Jirásek (CTU in Prague) and anonymous referees for their criticism and helpful comments on earlier versions of the manuscript. We also gratefully acknowledge financial support by the Czech Science Foundation through grants No. P105/12/0331 (JN), P105/11/P370 (AK), and P105/11/0411 (JZ). Our work was partially supported by the European Social Fund, grant No. CZ.1.07/2.3.00/30.0005 of Brno University of Technology (Support for the creation of excellent interdisciplinary research teams at Brno University of Technology, JN), by the Ministry of Education, Youth and Sports of the Czech Republic through project MSM 6840770003 (AK), and by the European Regional Development Fund under the IT4Innovations Centre of Excellence, project No. CZ.1.05/1.1.00/02.0070 (JZ).

Appendix A. Computation of mechanical fields

As explained earlier in Section 1, our objective is to determine local fields within a given domain $\mathcal{Y} \subset \mathbb{R}^2$ subjected to a given overall strain field

$$\boldsymbol{E} = \begin{bmatrix} E_{11} & E_{22} & \sqrt{2}E_{12} \end{bmatrix}^{\mathsf{T}}, \tag{A.1}$$

under the periodic boundary conditions. These follow from the solution of the elastic unit cell problem [28, 27]

$$\boldsymbol{\varepsilon}(\boldsymbol{x}) = \boldsymbol{\partial}\boldsymbol{u}(\boldsymbol{x}), \quad \boldsymbol{\partial}^{\mathsf{T}}\boldsymbol{\sigma}(\boldsymbol{x}) = \boldsymbol{0}, \quad \boldsymbol{\sigma}(\boldsymbol{x}) = \boldsymbol{L}(\boldsymbol{x})\boldsymbol{\varepsilon}(\boldsymbol{x}) \text{ for } \boldsymbol{x} \in \mathcal{Y}, \tag{A.2}$$

in which $\boldsymbol{u} : \mathcal{Y} \to \mathbb{R}^2$ designates the displacement field, $\boldsymbol{\varepsilon} : \mathcal{Y} \to \mathbb{R}^3$ and $\boldsymbol{\sigma} : \mathcal{Y} \to \mathbb{R}^3$ denote the $\mathcal{Y}$-periodic strain and stress fields, $\boldsymbol{L} : \mathcal{Y} \to \mathbb{R}^{3\times 3}$ stands for the symmetric positive-definite material stiffness matrix, and the operator matrix is defined as

$$\boldsymbol{\partial} = \begin{bmatrix} \frac{\partial}{\partial x_1} & 0 & \frac{1}{\sqrt{2}}\frac{\partial}{\partial x_2} \\ 0 & \frac{\partial}{\partial x_2} & \frac{1}{\sqrt{2}}\frac{\partial}{\partial x_1} \end{bmatrix}^{\mathsf{T}}. \tag{A.3}$$

In addition, the strain field is subject to a mean value-type constraint

$$\frac{1}{|\mathcal{Y}|}\int_{\mathcal{Y}} \boldsymbol{\varepsilon}(\boldsymbol{x})\,\mathrm{d}\boldsymbol{x} = \boldsymbol{E}. \tag{A.4}$$

It is well-known [27, 28] that the solution to the unit cell is characterised by the Lippmann-Schwinger equation

$$\boldsymbol{\varepsilon}(\boldsymbol{x}) + \int_{\mathcal{Y}} \boldsymbol{\Gamma}^0(\boldsymbol{x}-\boldsymbol{y})\delta\boldsymbol{L}(\boldsymbol{y})\boldsymbol{\varepsilon}(\boldsymbol{y})\,\mathrm{d}\boldsymbol{y} = \boldsymbol{E} \text{ for } \boldsymbol{x} \in \mathcal{Y}, \tag{A.5}$$

where $\delta\boldsymbol{L} = \boldsymbol{L} - \boldsymbol{L}^0$, $\boldsymbol{L}^0 \in \mathbb{R}^{3\times 3}$ is the stiffness matrix of an auxiliary reference medium

and the operator $\boldsymbol{\Gamma}^0 : \mathcal{Y} \to \mathbb{R}^{3\times3}$ is related to the Green function of the problem (A.2) with $\boldsymbol{L}(\boldsymbol{x}) = \boldsymbol{L}^0$. It admits a compact closed-form expression in the Fourier space, e.g. [27, Section 5.3], and its action can be efficiently evaluated by the FFT algorithm. This observation is at the heart of an iterative scheme due to Moulinec and Suquet [30], which can be applied to arbitrary digitised media. In our case, we adopt an accelerated version of the original algorithm based on observations due to Zeman *et al.* [47]. Since the sample is discretized by a regular $n_1^{\mathcal{Y}} \times n_2^{\mathcal{Y}}$ bitmap, it is convenient to project the integral equation onto the space of trigonometric polynomials, e.g. [39]. This yields the linear system in the form

$$(\boldsymbol{I} + \boldsymbol{B})\boldsymbol{e} = \boldsymbol{b}, \tag{A.6}$$

where $\boldsymbol{e} \in \mathbb{R}^{3\times n_1^{\mathcal{Y}}\times n_2^{\mathcal{Y}}}$ stores the unknown strain values at individual pixels, $\boldsymbol{b} \in \mathbb{R}^{3\times n_1^{\mathcal{Y}}\times n_2^{\mathcal{Y}}}$ is the corresponding matrix of overall strains and matrix $\boldsymbol{B}$ is expressed as a product of several matrices

$$\begin{aligned}\boldsymbol{B} = &\begin{pmatrix} \boldsymbol{F}^{-1} & \boldsymbol{0} & \boldsymbol{0} \\ \boldsymbol{0} & \boldsymbol{F}^{-1} & \boldsymbol{0} \\ \boldsymbol{0} & \boldsymbol{0} & \boldsymbol{F}^{-1} \end{pmatrix} \begin{pmatrix} \boldsymbol{\Gamma}_{1111} & \boldsymbol{\Gamma}_{1122} & \sqrt{2}\boldsymbol{\Gamma}_{1112} \\ \boldsymbol{\Gamma}_{2211} & \boldsymbol{\Gamma}_{2222} & \sqrt{2}\boldsymbol{\Gamma}_{1112} \\ \sqrt{2}\boldsymbol{\Gamma}_{2212} & \sqrt{2}\boldsymbol{\Gamma}_{1212} & 2\boldsymbol{\Gamma}_{2212} \end{pmatrix} \begin{pmatrix} \boldsymbol{F} & \boldsymbol{0} & \boldsymbol{0} \\ \boldsymbol{0} & \boldsymbol{F} & \boldsymbol{0} \\ \boldsymbol{0} & \boldsymbol{0} & \boldsymbol{F} \end{pmatrix} \\ &\times \begin{pmatrix} \delta\boldsymbol{L}_{1111} & \delta\boldsymbol{L}_{1122} & \sqrt{2}\delta\boldsymbol{L}_{1112} \\ \delta\boldsymbol{L}_{2211} & \delta\boldsymbol{L}_{2222} & \sqrt{2}\delta\boldsymbol{L}_{1112} \\ \sqrt{2}\delta\boldsymbol{L}_{2212} & \sqrt{2}\delta\boldsymbol{L}_{1222} & 2\delta\boldsymbol{L}_{2212} \end{pmatrix}.\end{aligned} \tag{A.7}$$

Here, $\boldsymbol{F} \in \mathbb{C}^{n_1^{\mathcal{Y}}\times n_2^{\mathcal{Y}}}$ and $\boldsymbol{F}^{-1}$ implement the forward and the inverse Fourier transform and, e.g., $\delta\boldsymbol{L}_{1122} \in \mathbb{R}^{n_1^{\mathcal{Y}}\times n_2^{\mathcal{Y}}}$ stores the corresponding component of the stiffness tensor at individual pixels, see [47] for more details. The system (A.6) is solved using standard conjugate gradient algorithm. Upon convergence, the distribution of the local stress field $\boldsymbol{\sigma}$ is determined from the solution $\boldsymbol{e}$ by Eq. $(A.2)_3$. The local displacement fields $\boldsymbol{u}$ follow from an inexpensive analysis in the Fourier space, e.g. [45].

Note that the construction of the enrichment functions is based on the perturbation fields of displacements and stresses

$$\boldsymbol{u}^*(\boldsymbol{x}) = \boldsymbol{u}(\boldsymbol{x}) - \tfrac{1}{|\mathcal{Y}|}\textstyle\int_{\mathcal{Y}} \boldsymbol{u}(\boldsymbol{y})\,\mathrm{d}\boldsymbol{y}, \tag{A.8}$$

$$\boldsymbol{\sigma}^*(\boldsymbol{x}) = \boldsymbol{\sigma}(\boldsymbol{x}) - \tfrac{1}{|\mathcal{Y}|}\textstyle\int_{\mathcal{Y}} \boldsymbol{\sigma}(\boldsymbol{y})\,\mathrm{d}\boldsymbol{y}, \tag{A.9}$$

instead of the total values. The enrichment functions for displacements, $\boldsymbol{\Psi}^*$ in Eq. (2), and stresses, $\boldsymbol{\Sigma}^*$ in Eq. (6), can now be constructed from the solutions to three load-cases, obtained by successively setting each component of E_{ij} in (A.1) to 1, while the ones become 0.

[1] I. Babuška and R. Lipton. Optimal local approximation spaces for generalized finite element methods with application to multiscale problems. *Multiscale Modeling and Simulation*, 9(1):373–406, 2011.

[2] T. Belytschko, R. Gracie, and G. Ventura. A review of extended/generalized finite element methods for material modeling. *Modelling and Simulation in Materials Science and Engineering*, 17(4):043001, 2009.

[3] M.F. Cohen, J. Shade, S. Hiller, and O. Deussen. Wang tiles for image and texture generation. *ACM Transactions on Graphics*, 22(3):287–294, 2003.

[4] K. Culik. An aperiodic set of 13 Wang tiles. *Discrete Mathematics*, 160:245–251, 1996.

[5] K. Culik and J. Kari. An aperiodic set of Wang cubes. *Journal of Universal Computer Science*, 1(10):675–686, 1995.

[6] E.D. Demaine and M.L. Demaine. Jigsaw puzzles, edge matching, and polyomino packing: Connections and complexity. *Graphs and Combinatorics*, 23:195–208, 2007.

[7] M. Doškář. Geometrical modelling of heterogenous materials based on Wang tilings. Bachelor thesis, Czech Technical University in Prague, 2012. Available at `http://mech.fsv.cvut.cz/wiki/index.php/File:BP-2012-Doskar.pdf` (in Czech).

[8] J.D. Eshelby. The determination of the elastic field of an ellipsoidal inclusion, and related problems. *Proceedings of the Royal Society of London. Series A, Mathematical and Physical Sciences*, 241(1226):376–396, 1957.

[9] J.D. Eshelby. The elastic field outside an ellipsoidal inclusion. *Proceedings of the Royal Society of London. Series A. Mathematical and Physical Sciences*, 252(1271):561–569, 1959.

[10] F. Feyel and J.-L. Chaboche. FE^2 multiscale approach for modelling the elastovisco-plastic behaviour of long fibre SiC/Ti composite materials. *Computer Methods in Applied Mechanics and Engineering*, 183(3-4):309–330, 2000.

[11] J. Fish and Z. Yuan. Multiscale enrichment based on partition of unity. *International Journal for Numerical Methods in Engineering*, 62(10):1341–1359, 2005.

[12] J. Fish and Z. Yuan. Multiscale enrichment based on partition of unity for nonperiodic fields and nonlinear problems. *Computational Mechanics*, 40:249–259, 2007.

[13] T.-P. Fries and T. Belytschko. The extended/generalized finite element method: An overview of the method and its applications. *International Journal for Numerical Methods in Engineering*, 84(3):253–304, 2010.

[14] J. Gajdošík, J. Zeman, and M. Šejnoha. Qualitative analysis of fiber composite microstructure: Influence of boundary conditions. *Probabilistic Engineering Mechanics*, 21(4):317–329, 2006.

[15] M.G.D. Geers, V.G. Kouznetsova, and W.A.M. Brekelmans. Multi-scale computational homogenization: Trends and challenges. *Journal of Computational and Applied Mathematics*, 234:2175–2182, 2010.

[16] A. Glassner. Andrew Glassner's notebook. *Computer Graphics and Applications, IEEE*, 24(1):86–91, 2004.

[17] I. Herrera. Trefftz method: a general theory. *Numerical Methods for Partial Differential Equations*, 16(6):561–580, 2000.

[18] Ł. Kaczmarczyk and C.J. Pearce. A corotational hybrid-Trefftz stress formulation for modelling cohesive cracks. *Computer Methods in Applied Mechanics and Engineering*, 198(15–16):1298–1310, 2009.

[19] S. Kirkpatrick, C. Jr. Gelatt, and M. P. Vecchi. Optimization by simulated annealing. *Science*, 220:671–680, 1983.

[20] H. Kumar, C.L. Briant, and W.A. Curtin. Using microstructure reconstruction to model mechanical behavior in complex microstructures. *Mechanics of Materials*, 38(8–10):818–832, 2006.

[21] A. Lagae and P. Dutré. A comparison of methods for generating Poisson disk distributions. *Computer Graphics Forum*, 27(1):114–129, 2008.

[22] H. Lee, M. Brandyberry, A. Tudor, and K. Matouš. Three-dimensional reconstruction of statistically optimal unit cells of polydisperse particulate composites from microtomography. *Physical Review E*, 80:061301, 2009.

[23] M. Lepš. *Single and Multi-Objective Optimization in Civil Engineering with Applications*. PhD thesis, CTU in Prague, 2005. Available at `http://klobouk.fsv.cvut.cz/~leps/publications/pdf/thesis.pdf`.

[24] A. Lu, D.S. Ebert, W. Qiao, M. Kraus, and B. Mora. Volume illustration using Wang cubes. *ACM Transactions on Graphics*, 26, 2007.

[25] A.M. Matache, I. Babuška, and C. Schwab. Generalized p-FEM in homogenization. *Numerische Mathematik*, 86:319–375, 2000.

[26] J.M. Melenk and I. Babuška. The partition of unity finite element method: Basic theory and applications. *Computer Methods in Applied Mechanics and Engineering*, 139(1–4):289–314, 1996.

[27] J.C. Michel, H. Moulinec, and P. Suquet. Effective properties of composite materials with periodic microstructure: a computational approach. *Computer Methods in Applied Mechanics and Engineering*, 172(1-4):109 – 143, 1999.

[28] G. W. Milton. *The Theory of Composites*, volume 6 of *Cambridge Monographs on Applied and Computational Mathematics*. Cambridge University Press, 2002.

[29] R. Morgan and I. Babuška. An approach for constructing families of homogenized equations for periodic media. I: An integral representation and its consequences. *SIAM Journal on Mathematical Analysis*, 22(1):1–15, 1991.

[30] H. Moulinec and P. Suquet. A fast numerical method for computing the linear and nonlinear mechanical properties of composites. *Comptes rendus de l'Académie des sciences. Série II, Mécanique, physique, chimie, astronomie*, 318(11):1417–1423, 1994.

[31] S.R. Niezgoda, D.M. Turner, D.T. Fullwood, and S.R. Kalidindi. Optimized structure based representative volume element sets reflecting the ensemble-averaged 2-point statistics. *Acta Materialia*, 58(13):4432–4445, 2010.

[32] J. Novák, Ł. Kaczmarczyk, P. Grassl, J. Zeman, and C. Pearce. A micromechanics-enhanced finite element formulation for modelling heterogeneous materials. *Computer Methods in Applied Mechanics and Engineering*, 201–204:53–64, 2012.

[33] J. Novák, A. Kučerová, and J. Zeman. Compressing random microstructures via stochastic Wang tilings. *Physical Review E*, 86:040104, 2012.

[34] J.T. Oden, T. Belytschko, J. Fish, T.J.R. Hughes, C. Johnson, D. Keyes, A. Laub, L. Petzold, D. Srolovitz, and S. Yip. Simulation-based engineering science: Revolutionizing engineering science through simulation. Report of the National Science Foundation blue ribbon panel on simulation-based engineering science, National Science Foundation, Arlington, VA, 2006. Available at `http://www.nsf.gov/pubs/reports/sbes_final_report.pdf`.

[35] B. Pichler, S. Scheiner, and C. Hellmich. From micron-sized needle-shaped hydrates to meter-sized shotcrete tunnel shells: Micromechanical upscaling of stiffness and strength of hydrating shotcrete. *Acta Geotechnica*, 3(4):273–294, 2008.

[36] G.L. Povirk. Incorporation of microstructural information into models of two-phase materials. *Acta Metallurgica et Materialia*, 43(8):3199–3206, 1995.

[37] F.K.F. Radtke, A. Simone, and L.J. Sluys. A partition of unity finite element method for obtaining elastic properties of continua with embedded thin fibres. *International Journal for Numerical Methods in Engineering*, 84(6):708–732, 2010.

[38] F.K.F. Radtke, A. Simone, and L.J. Sluys. A partition of unity finite element method for simulating non-linear debonding and matrix failure in thin fibre composites. *International Journal for Numerical Methods in Engineering*, 86(4–5):453–476, 2011.

[39] J. Saranen and G. Vainikko. *Periodic Integral and Pseudodifferential Equations with Numerical Approximation*. Springer Monographs in Mathematics. Springer-Verlag, Berlin, Heidelberg, 2002.

[40] J. Schröder, D. Balzani, and D. Brands. Approximation of random microstructures by periodic statistically similar representative volume elements based on lineal-path functions. *Archive of Applied Mechanics*, 81:975–997, 2011.

[41] J.A. Teixeira de Freitas. Formulation of elastostatic hybrid-Trefftz stress elements. *Computer Methods in Applied Mechanics and Engineering*, 153:127–151, 1998.

[42] S. Torquato. *Random heterogenous materials*. Springer-Verlag, New York, 2002.

[43] J. Černý. Thermodynamical approach to the traveling salesman problem: An efficient simulation algorithm. *Journal of Optimization Theory and Applications*, 45:41–51, 1985.

[44] H. Wang. Proving theorems by pattern recognition–II. *Bell Systems Technical Journal*, 40(2):1–41, 1961.

[45] F. Willot, Y.-P. Pellegrini, M.I. Idiart, and P.P. Castañeda. Effective-medium theory for infinite-contrast two-dimensionally periodic linear composites with strongly anisotropic matrix behavior: Dilute limit and crossover behavior. *Physical Review B*, 78:104111, 2008.

[46] C.L.Y. Yeong and S. Torquato. Reconstructing random media. *Physical Review E*, 57(1):495–506, 1998.

[47] J. Zeman, J. Vondřejc, J. Novák, and I. Marek. Accelerating a FFT-based solver for numerical homogenization of periodic media by conjugate gradients. *Journal of Computational Physics*, 229(21):8065–8071, 2010.

[48] J. Zeman and M. Šejnoha. From random microstructures to representative volume elements. *Modelling and Simulation in Materials Science and Engineering*, 15(4):S325–S335, 2007. 2007 Higlight paper.

Chapter 6

FOLLOW-UP DEVELOPMENTS

In the following chapter, the impact of Author's work in the scientific community is highlighted in terms of a brief overview on follow-up works motivated by the results presented in **Chapters 2–5**.

Follow-up Developments

Jan Novák

Experimental Centre, Faculty of Civil Engineering, Czech Technical University in Prague, Czech Republic

The presented work yielded in a new research agenda, namely on Wang tiling presented in **Chapter 4** and **Chapter 5**, that has been justified by a number of follow-up works from the field of Simulation science and, for the time being, one publication from a popular subject on additive manufacturing [1]. The obvious, but uneasy, extension of the compression of random mono-dispersion [2] to complex "real world" material systems was presented by Doškář [3] as early after its introduction to Materials Engineering community as in 2013. A deeper extension of Doškář's developments, involving also the use of Wang tiles in numerical homogenization was published later in [4]. The scientifically most tangible findings elaborated in the two theses were consequently summarized and discussed in [5]. The homogenization strategies supported by Wang tiles were also successfully applied to the analysis of macroscopic properties of high porosity materials, metallic foams in particular, that are often cumbersome to be analyzed by majority of conventional homogenization strategies. These particular results are covered in detail in [6]. As the formalism of Wang tiles is, by definition, well-suited for generating microstructure realizations additively growing in size, they naturally found use in statistical determination of Representative Volume Element dimensions in conjunction with bounds to apparent properties of certain synthetic as well as natural composites [7]. As the principle of generalized periodicity is encoded in Wang tiles, further works mirroring the developments originally made for the Periodic Unit Cell paradigm have been mirrored also into Wang tiles, see e.g. [8]. As mentioned in **Chapter 1**, the very recent Computational Mechanics oriented outcome provoked by the findings explored in **Chapter 2** and **Chapter 5** of this collection, such that it targets the propagation of microstructure-induced information into the coarse scale solutions by means of Reduced Order Modeling method was studied and presented by Doškář et al. [9].

Further promising results were brought by Tyburec et al. [10]. Here the Wang tiling stays behind the "modularity engine" of the topology optimization procedure for truss structures that commenced during Tyburec's Ph.D. work published in [11]. The extension of modular optimization principles to compliant structures and mechanisms has been also recently accepted for publication [12]. Tyburec's, rather theoretical works have been preceded also by a decent application of Wang tiles in fabrication of modular 3D printed functional reinforcement of wound composite hollow beams designed with semidefinite programming [13].

Last but not least, Author's findings presented in **Chapter 2** and **Chapter 3** has been further elaborated in terms of establishing direct solution to the algebraic system arising from the proposed, originally iterative, self-compatibility technique to incorporate inclusion interactions in non-dilute media, see Meng [14], Meng et al. [15, 16].

Email address: novakja@fsv.cvut.cz (Jan Novák)

References

[1] V. Nežerka, M. Somr, T. Janda, J. Vorel, M. Doškář, J. Antoš, J. Zeman, J. Novák, A jigsaw puzzle metamaterial concept, Composite Structures 202 (2018) 1275–1279, ISSN 02638223, doi:10.1016/j.compstruct.2018.06.015.

[2] J. Novák, A. Kučerová, J. Zeman, Compressing random microstructures via stochastic Wang tilings, Physical Review E 86 (4) (2012) 040104(R), ISSN 1539-3755, 1550-2376, doi:10.1103/PhysRevE.86.040104.

[3] M. Doškář, Wang tilings for real world material systems, Master's thesis, Czech Technical University in Prague, Prague, 2013.

[4] M. Doškář, Wang tiling for modelling of heterogeneous materials, Ph.D., Czech Technical University in Prague, doi:10.14311/dis.fsv.2019.001, 2019.

[5] M. Doškář, J. Novák, J. Zeman, Aperiodic compression and reconstruction of real-world material systems based on Wang tiles, Physical Review E 90 (6) (2014) 062118, ISSN 1539-3755, 1550-2376, doi:10.1103/PhysRevE.90.062118.

[6] M. Doškář, J. Novák, A jigsaw puzzle framework for homogenization of high porosity foams, Computers & Structures 166 (2016) 33–41, ISSN 00457949, doi:10.1016/j.compstruc.2016.01.003.

[7] M. Doškář, J. Zeman, D. Jarušková, J. Novák, Wang tiling aided statistical determination of the Representative Volume Element size of random heterogeneous materials, European Journal of Mechanics - A/Solids 70 (2018) 280–295, ISSN 09977538, doi:10.1016/j.euromechsol.2017.12.002.

[8] M. Doškář, J. Zeman, D. Rypl, J. Novák, Level-set Based Design of Wang Tiles for Modelling Complex Microstructures, Computer-Aided Design 123 (2020) 102827, ISSN 00104485, doi:10.1016/j.cad.2020.102827.

[9] M. Doškář, J. Zeman, P. Krysl, J. Novák, Microstructure-informed reduced modes synthesized with Wang tiles and the Generalized Finite Element Method, Computational Mechanics 68 (2) (2021) 233–253, ISSN 0178-7675, 1432-0924, doi:10.1007/s00466-021-02028-y.

[10] M. Tyburec, J. Zeman, M. Doškář, M. Kruk, M. Lepš, Modular-topology optimization with Wang tilings: an application to truss structures, Structural and Multidisciplinary Optimization 63 (3) (2021) 1099–1117, ISSN 1615-147X, 1615-1488, doi:10.1007/s00158-020-02744-8.

[11] M. Tyburec, Modular-Topology Optimization of Structures and Mechanisms, Ph.D., Czech Technical University in Prague, doi:http://hdl.handle.net/10467/98774, 2021.

[12] M. Tyburec, M. Doškář, J. Zeman, M. Kružík, Modular-topology optimization of structures and mechanisms with free material design and clustering, Computer Methods in Applied Mechanics and Engineering (In print).

[13] M. Tyburec, J. Zeman, J. Novák, M. Lepš, T. Plachý, R. Poul, Designing modular 3D printed reinforcement of wound composite hollow beams with semidefinite programming, Materials & Design 183 (2019) 108131, doi:10.1016/j.matdes.2019.108131.

[14] C. Meng, Extending Esh3D Code to Solve Interacting Eshelby's Inhomogeneity Problems, Earth and Space Science 6 (8) (2019) 1569–1577, ISSN 2333-5084, doi: 10.1029/2019EA000594.

[15] C. Meng, C. Gu, B. Hager, An Eshelby solution-based finite-element approach to heterogeneous fault-zone modeling, Seismological Research Letters 91 (1) (2020) 465–474, doi:10.1785/0220190083.

[16] C. Meng, M. Fehler, B. Hager, Elastic medium containing interacting fluid inclusions, Composite Structures 256 (2021) 113018, doi:10.1016/j.compstruct.2020.113018.

LIST OF AUTHOR'S PUBLICATIONS

WOS journal papers

Doškář, Martin and Zeman, Jan and Krysl, Petr and Novák, Jan (2021). Microstructure-informed reduced modes synthesized with Wang tiles and the Generalized Finite Element Method. *Computational Mechanics*, 68(2):233–253.

Doškář, Martin and Zeman, Jan and Rypl, Daniel and Novák, Jan (2020). Level-set based design of Wang tiles for modelling complex microstructures. *Computer-Aided Design*, 123:102827.

Tyburec, Marek and Zeman, Jan and Novák, Jan and Lepš, Matěj and Plachỳ, Tomáš and Poul, Robin (2019). Designing modular 3D printed reinforcement of wound composite hollow beams with semidefinite programming. *Materials & Design*, 183:108131.

Nežerka, V and Somr, M and Janda, T and Vorel, J and Doškář, M and Antoš, J and Zeman, J and Novák, J (2018). A jigsaw puzzle metamaterial concept. *Composite Structures*, 202:1275–1279.

Doškář, Martin and Zeman, Jan and Jarušková, Daniela and Novák, Jan (2018). Wang tiling aided statistical determination of the Representative Volume Element size of random heterogeneous materials. *European Journal of Mechanics-A/Solids*, 70:280–295.

Horák, Martin and Patzák, Bořek and Novák, Jan (2018). An isogeometric extension of Trefftz method for elastostatics in two dimensions. *International Journal for Numerical Methods in Engineering*, 114(11):1213–1227.

Svoboda, Ladislav and Šulc, Stanislav and Janda, Tomáš and Vorel, Jan and Novák, Jan (2016). μMech micromechanics library. *Advances in Engineering Software*, 100:148–160.

Doškář, Martin and Novák, Jan (2016). A jigsaw puzzle framework for homogenization of high porosity foams. *Computers & Structures*, 166:33–41.

Doškář, Martin and Novák, Jan and Zeman, Jan (2014). Aperiodic compression and reconstruction of real-world material systems based on Wang tiles. *Physical Review E*, 90(6):062118.

Svoboda, Ladislav and Novák, Jan and Kurilla, Lukáš and Zeman, Jan (2014). A framework for integrated design of algorithmic architectural forms. *Advances in Engineering Software*, 72:109–118.

Oberrecht, SP and Novák, J and Krysl, P (2014). B-bar FEMs for anisotropic elasticity. *International Journal for Numerical Methods in Engineering*, 98(2):92–104.

Novák, Jan and Kučerová, Anna and Zeman, Jan (2013). Microstructural enrichment functions based on stochastic Wang tilings. *Modelling and Simulation in Materials Science and Engineering*, 21(2):025014.

Novák, Jan and Kučerová, Anna and Zeman, Jan (2012). Compressing random microstructures via stochastic Wang tilings. *Physical Review E*, 86(4):040104.

Novák, Jan and Kaczmarczyk, Łukasz and Grassl, Peter and Zeman, Jan and Pearce, Chris J (2012). A micromechanics-enhanced finite element formulation for modelling heterogeneous materials. *Computer Methods in Applied Mechanics and Engineering*, 201:53–64.

Zeman, Jan and Vondřejc, Jaroslav and Novák, Jan and Marek, Ivo (2010). Accelerating a FFT-based solver for numerical homogenization of periodic media by conjugate gradients. *Journal of Computational Physics*, 229(21):8065–8071.

Zeman, Jan and Novák, Jan and Šejnoha, Michal and Šejnoha, Jiří (2008). Pragmatic multiscale and multi-physics analysis of Charles Bridge in Prague. *Engineering Structures*, 30(11):3365–3376.

Tomková, Blanka and Sejnoha, Michal and Novák, Jan and Zeman, Jan (2008). Evaluation of effective thermal conductivities of porous textile composites. *International Journal for Multiscale Computational Engineering*, 6(2):–.

Book chapters

Pearce, C. J. and Kaczmarczyk, L. and Novák, J. (2010). Multiscale modelling strategies for heterogeneous materials. In *Comuputational Technology Reviews*, pages 23–49. Saxe-Coburg Publications.

Novák, J. and Zeman, J. and Šejnoha, M. and Šejnoha, J. (2008). Multi-Scale and Multi-Physics Study of Charles Bridge in Prague as a Basis for Rehabilitation. In *Contributions to numerical and experimental investigation of building materials and structures*, pages 83–88. Czech Technical University in Prague.